UNIVERSITY OF SOUTHAMPTON

FACULTY OF ENGINEERING, SCIENCES AND MATHEMATICS

School of Engineering Sciences

Hollow Cathode Life Time Modelling

by

Michele Coletti, BSc, MSc

Thesis for the degree of Doctor of Philosophy

November 2008

ABSTRACT

Hollow Cathodes (HCs) are of primary importance in the field of electric space propulsion, being used as electron sources in ion and Hall-effect thrusters. Hence, their lifetime is a key factor in all these applications.

HCs have demonstrated the capability of providing up to 30,000 hours of operation, whereas no direct experimental data exist above this limit.

The importance of HC lifetime is a growing issue for deep space missions using propulsive systems based on ion or Hall-effect thrusters that may require longer lifetimes than those demonstrated up to now. To address these concerns about HCs and to prove the suitability of an ion thrusters based solar electric propulsion subsystem for future high-impulse missions (such as Bepi Colombo), a model able to predict the HC lifetime is needed.

The model that has been developed in this thesis consists of three parts: a barium oxide depletion model, a low work function surface coverage model and a plasma update procedure to calculate the effects that a change in the insert surface work function will produce on the cathode plasma.

The barium-oxide depletion model has been validated by comparing its results with experimental measurements performed at QinetiQ and NASA, showing a good quantitative agreement.

The low-work function surface coverage model is the first of its kind to include the effect of ion bombardment. The plasma update procedure, even if semi-empirical, is able to produce results that are in good agreement with the measurements.

Using these three models the lifetime of the NSTAR hollow cathode has been simulated, yielding predictions that are in good agreement with the theoretical expectations.

Ai miei nonni

Acknowledgments

First of all I would like to thank everybody that helped and supported me during these two years and a half in particular my family and my friends.
I would also like to thank everybody I met in this period in Southampton and around the world, I mean every single person that made me laugh, cry, scream or anything else cause thanks to them I manage to feel home even in a place with no season, no food (apart for the ones foreigners coming from the Mediterrean cook), no sun, no colours and a lot of useless rain (...well they call it England).
After all these people I want to thank the three professors that missed me at the PhD admission exams in the University of Rome in October 2005, even if you did it only for miserable political reason you made me a great favour without wanting it.
Last but not least I would like to thank Prof. Stephen Gabriel that more than a supervisor has been a friend during this period I spent in Southampton.
Thanks to all of you...I don’t put names only because you are too many and I will definitely forget somebody.

Table of Contents

List of Tables

List of Figures

1 Introduction

1.1 Aim of this thesis

Hollow cathodes are key devices in the field of electric space propulsion, being used as electron sources and neutralizers inside gridded ion thrusters(GIE) and Hall effect thrusters, as plasma contactors onboard of the International Space Station and in the future probably as standalone thrusters [1].

With the increase in the duration and complexity of space missions the lifetime of the electric propulsion subsystem is becoming a growing issue.

Since both GIEs and Hall Effect thrusters make use of hollow cathodes their lifetime can be a key factor in all these application. Hollow cathodes have demonstrated the ability of providing up to 30,000 hours of functioning whereas no experimental data exists above this limit [2].

The 30,000 hours lifetime has been demonstrated with a single long duration test performed on a single cathode (NASA NSTAR cathode from the Deep Space 1 spare ion engine); hence if a mission requires a lifetime longer than 30,000 hours or demands operational parameters that are different from those used during this test the use of a hollow cathode-based electric propulsion subsystem might pose risks unless a way of assessing the cathode lifetime is found.

The use of testing every time the lifetime of a cathode must be known is unfeasible considering the extremely long timescale of the tests (30,000 hours correspond to three and a half years) and the consequential enormous cost associated with such long tests; it must also be noted how accelerated life tests are not a reliable option since the way lifetime scales with the characteristic functioning parameters of an hollow cathode is still not well known.

Given the aforementioned the need for a model capable of predicting the lifetime of a cathode is clear.

The aim of this thesis is then the development of the first hollow cathode lifetime model able to predict the lifetime of a cathode starting from its operational parameters like discharge current and insert temperature distribution.

1.2 Hollow cathode description

A modern hollow cathode (HC) for space propulsion application consists mainly of a cylindrical tube (made of tantalum or tungsten) through which gaseous propellant is passed. At the downstream end of the tube a plate with a small orifice is present to impede gas exit hence to increase the internal pressure.

To improve HC performance allowing them to work in steady state at lower power levels a low work function insert is added inside the HC cavity, and heater element is placed on the outer surface of the tube positioned on the region of the dispenser while downstream of the tube, just after the orifice plate, an external anode electrode (referred to as the keeper) is present.

This insert commonly consists of a porous matrix of tungsten welded on the downstream end of the inner surface of the tube butted up against the inner part of the orifice plate. This matrix is impregnated with a mixture of low work function compounds. In hollow cathodes for space application the most commonly used impregnant is a mixture of barium oxide, calcium oxide and alumina in the proportion 4 BaO – 1 CaO – 1Al_2O_3 .

Outside the cathode tube a “keeper electrode” is present. This electrode is used during the cathode start up where a potential is applied to it to initiate the discharge. The discharge is then transferred from the keeper to the main anode that can consist in a real electrode (when the HC is used inside ion or Hall Effect thrusters) or in a positive ion beam (when the cathode is used as a neutralizer).

From this point on is not necessary to continue drawing current from the keeper; even so, this is commonly done in ion thrusters to ensure that the cathode will continue running even in case the main anode current or the ion beam are interrupted.

A sketch of a common hollow cathode configuration is in Figure 1

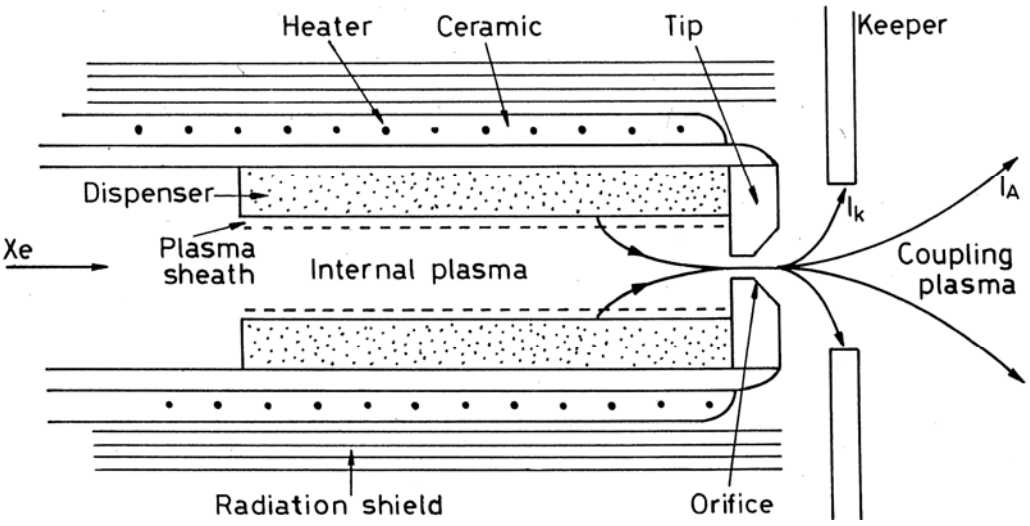

Figure 1 – Hollow cathode configuration (image courtesy of QinetiQ)

The heater is used only during the start-up phase of the hollow cathode to heat up the insert. Once the insert has reached a temperature around 1100 °C barium oxide evaporation from the impregnant contained in the pores starts. These barium vapours will deposit on the surface of the insert, on the internal surface of the orifice plate and in the orifice lowering the average work function of these surfaces from the value of bare tungsten (4.5 eV) down to a value of about 2-2.5 eV.

Due to this barium layer and to the relatively high temperature, thermionic emission will occur. The emitted electrons will lower the inter electrode resistance reducing the breakdown voltage to help the initiation of the discharge.

With the establishment of the discharge between the cathode body and the keeper/anode, a plasma is created inside the hollow cathode cavity.

The presence of the plasma inside the hollow cathode cavity and of thermionic emitted electrons at the cathode/insert surface will lead to the creation of a sheath region between the plasma and the cathode/insert surface.

Using density and temperature measurements present in the literature [3]-[6],[26] the sheath thickness (that is of the order of some Debye lengths) can be estimated in about 10^{-5} m, whereas the voltage drop occurring across it is about 5-15 Volt; this provides an electric field at the surface of the insert of about 10^6 V/m.

Because of their random thermal motion some ions and electrons present in the plasma column may move towards the sheath region. Every ion, once it has reached the sheath region, will be accelerated by the voltage drop towards the cathode surface; on the contrary the electrons will be repelled by the sheath voltage being able to reach the

cathode surface only if their energy is higher than the sheath potential. From now one we will refer to this flux of electrons to the HC surface as “back-streaming electrons”.
Hence the presence of the sheath will limit electron back-streaming to the surface that would produce a reduction in the net emitted current and, accelerating ions toward the HC surface, will provide an ion current that will contribute to the net current produced by the cathode and .
These ions, being accelerated through the sheath to electron volt level energies, colliding with the insert surface will provide enough heating to maintain the insert temperature sufficiently high (around 1100 °C) to produce the required thermionic emission hence allowing the heater to be switched off.
This high electric field at the insert surface enhances thermionic emission while the voltage drop accelerates the electrons towards the plasma column with energies of the order of the sheath voltage drop (5~15 eV). These electrons will collide with neutral propellant gas atoms (commonly Xenon) causing ionization and thus the production of other free electrons. The electrons are then accelerated by the main axial electric field toward the orifice, where the sudden area reduction increases the pressure increasing the collisions between electrons and neutrals enhancing the ionization process; the electron so generated, “pushed” by the high pressure in the orifice and accelerated by the electric field will then be “emitted” through the orifice into the volume outside the cathode.
Now that the functioning of a hollow cathode has been qualitatively described the main processing taking place will be discussed in more detail.

1.3 Thermionic emission

Thermionic emission is the process first measured by Richardson in 1901, where the electrons of a metal are able to escape its surface thanks to their vibration energy. This will happen only if an electron has energy higher than the electrostatic force restraining it on the surface. The minimum amount of energy that an electron must possess to overcome this restraining force is called “work function” and is of the order of some eV. Since the work function is much higher than the metal temperature (the work function is of the order of some eV whereas the metal temperature is certainly much lower since 1 eV corresponds to 11,600 °K and any metal would melt at this temperature), the ratio of electrons escaping the surface is going to be proportional to the exponential of the ratio

between the energy needed to leave the surface and the thermal energy possessed by the electrons.

This has been mathematically demonstrated by Dushman in 1923 with the formulation of the so called Richardson-Dushman law where the current density emitted thermionically is related to the surface temperature and work function

$$J_{th} = A_{th} T^2 e^{\frac{-q\phi}{k_b T}} \tag{1}$$

where A_{th} is the thermionic emission constant and has a value of $1.26 \cdot 10^6$ A m^{-2} K^{-2}.

The escape of electrons from the metal surface is also influenced by the presence of an electric field perpendicular to the surface. The effect of this field can usually be modelled with a simple modification of the Richardson-Dushman equation; in particular the value of the work function is lowered by the presence of the electric field perpendicular to the surface and pointing towards it (hence tending to extract electrons). If the electric field strength is lower than about 10^8 V m^{-1}, the field enhancement is known as the Schottky effect [8]. In this case an "effective" value of the work function relative to the metal work function and to the electric field can be introduced, its value is

$$\phi_{eff} = \phi - \sqrt{\frac{qE}{4\pi\epsilon_0}} \tag{2}$$

If the electric field is above 10^8 V m^{-1} quantum effects become important [8] and the relations in Eq. (1) and (2) are no longer valid. In this case the emission process in no longer called "thermionic emission" but takes the name of "field emission". Since in HC operations the electric field is normally below the threshold value of 10^8 V m^{-1}, field emission will not be investigated further. As said before the electric field can be estimated to be of the order of 10^6 V m^{-1} hence from Eq. (2) the magnitude of the work function reduction due to the Schottky effect is about 0.03 eV. In the densest region of the plasma the Debye length can be smaller than the average one cited before (10^{-5} m) hence increasing the value of the electric field at the insert surface consequently increasing the Schottky correction up to a value of the order of 0.1 eV.

1.4 Current and power balances

To better understand the functioning of the cathode we will now describe qualitatively the current and power balances existing in the cathode.

We can distinguish two main power balances: one on the insert surface and another one inside the plasma column.

On the insert surface the main fluxes are ion and electron flux from the plasma column, electron flux from the cathode surface toward the plasma and evaporated barium oxide leaving the insert.

The ion and electron fluxes from the plasma are the main source of heating for the insert. In fact the ions, being accelerated through the sheath voltage drop, deposit on the surface an energy of the order of some eV and, recombining with the electrons present on the surface, release an energy equal to their ionization energy (for Xenon 12 eV) under the form of heat whereas the electrons that, coming from the plasma column, are able to reach the HC surface deposit their thermal energy (of the order of 1 eV) and assuming that they get absorbed by the surface they also release an energy equal to the work function of the surface (in the form of heat).

The thermionic emission from the surface is the main source of cooling for the insert. In fact every emitted electron "removes" from the insert an energy equal to its thermal energy (of the order of 1400 °K ~ 0.12 eV) plus the energy needed for its emission (work function).

The flux of evaporated barium oxide leaving the insert provides a cooling effect since they remove from the surface and energy equal to their thermal energy (~ 0.12 eV) plus the energy needed for their evaporation (some eV).

We must also take into account the power irradiated from the plasma to the surface and from the surface back to the plasma. The power irradiated from the plasma to the surface is quite small if compared to the fluxes reported above because of the relatively low temperature for the plasma (~1 eV). The net power irradiated from the surface to the plasma is also small because the plasma inside the cavity has been found to be transparent [9] and because of the HC geometry. In fact the HC tube almost completely enclose the plasma (except the apertures present at the orifice and upstream the tube) hence the power irradiated from a part of the HC surface (for example the upper part in Figure 1), not being absorbed by the plasma (since it is transparent), will reach the opposite part of the cathode tube (lower part in Figure 1) and there will be absorbed hence minimizing the net radiated power.

Regarding the power balance in the plasma we have that the main heating process is thermionic emitted electron flux accelerated through the sheath and ohmic heating

whereas the main cooling processes are ion and electron fluxes from the plasma to the surface.

Regarding the cathode current balance the total current flowing in the cathode is fixed by the power supply. This current is equal to the sum of the thermionic emitted current plus the current relative to the ion flux from the plasma to the surface minus the one relative to the electron back-streaming flux.

Considering what has been said above we can see how a hollow cathode tends to auto-regulate. Let's for example assume that starting from a stable functioning condition of the cathode the thermionic emission is decreased due to a work function increase caused by a change in the insert surface. In this case the cathode, to maintain its current requirement, will try to increase the temperature of the insert to increase the thermionic emission. To do so the power deposited by the ion flux must be increased, this will be achieved increasing the sheath voltage drop. This will consequently decrease the electron back-flow to the surface reducing the back-streaming current. Another effect of the sheath voltage drop increase is the reduction of the work function thanks to the Schottky effect and the consequent increase of the thermionic emission. The increase in the thermionic current and in the voltage drop will tend to cool the insert balancing the heating effect due to the ion flux hence bringing the insert to a new stable condition with a higher insert temperature.

1.5 Hollow cathode lifetime

In the past the hollow cathode lifetime has been the object of several studies [10]-[16]. Although a great deal of effort has been spent in these studies, a model able to predict the cathode lifetime has still not been developed.

The end of life of a cathode is normally identified with the impossibility of starting the cathode within the capabilities of the power supply i.e. the breakdown voltage needed to initiate the discharge goes beyond the maximum voltage of the power supply.

The discharge voltage needed to initiate the discharge is somehow related to the work function of the surface hence to the amount of barium that evaporates during the start-up phase and to the amount of low work function compounds that are already present on the surface.

During the normal functioning of the cathode barium oxide evaporates from the impregnant present inside the insert pores and subsequently deposits on the surface lowering the surface work function.

Due to this evaporation the BaO content inside the insert pores will slowly decrease. In particular the barium oxide content will be lower closer to the surface where evaporation takes place than in the insert core; this will give raise to a diffusion motion of BaO from the insert core to the surface.

The combined effects of barium oxide evaporation from the pores and BaO diffusion inside the insert constitute the barium oxide depletion process that will determine the exact distribution of BaO inside the insert.

The evaporation rate of barium oxide from the insert will decrease during lifetime reducing the deposition rate of low work function compounds.

Experimental investigations of the activated insert surface have shown how over the tungsten matrix there is first a strongly bonded oxygen layer and then, on top of this, a barium layer that lowers the work function down to about 2 eV [17].

The barium and oxygen atoms constituting these two layers are reported to be chemisorpted [17] meaning that some kind of chemical bond exists between them and with the tungsten surface.

These adsorbed atoms are then desorpted by thermal evaporation and by ion bombardment and replaced by deposition of new barium and barium oxide coming from the insert. The relative magnitude of these processes will determine the increase or the decrease of the low work function surface coverage and the consequent evolution of the insert work function and of the thermionic emission.

When the surface coverage drops below a value such that the evaporation of BaO from the insert pores during the start up phase of the cathode is not high enough to produce a full low work function coverage of the insert surface, the thermionic emission will start to decrease with a consequent increase of the breakdown voltage. This process will then go on up to the point where the required voltage will be above the maximum one that can be supplied by the power supply resulting in the end of the cathode's operational life.

Hence it is clear that to derive the trend of the breakdown voltage, a model to predict the evaporation of barium oxide from the insert pore and its subsequent depletion and a model to predict the formation and desorption of low work function compounds, are needed.

The models presented in the literature commonly calculate barium oxide depletion assuming that BaO production is the effect of only one chemical reaction and/or calculating the barium oxide depletion using the scaling law experimentally demonstrated by Roquais [10] according to which the depletion depth (commonly intended as the distance from the insert surface towards the insert core where all the barium oxide has evaporated) is proportional to the square root of time.

In the model that will be presented in this thesis the barium oxide evaporation will be calculated taking into account the full chemistry of the impregnant including all the compounds formed by BaO together with CaO and Al_2O_3 whereas the barium oxide depletion process will be modelled simulating the insert with a three dimensional code taking into account both the barium oxide evaporation and the diffusion motion of barium oxide inside the insert.

It will be shown how the reduction of the insert chemistry to a single reaction produces results that overestimate the barium oxide mass flow rate by several orders of magnitude.

The barium oxide depletion model is then validated by comparing the numerical data with the experimental ones measured at QinetiQ and at the NASA Jet Propulsion Laboratory.

The model shows good qualitative and quantitative agreement and is the first model able to simulate a 3D insert taking into account the complex impregnant chemistry and the processes involving barium oxide diffusion being capable of producing results that are in quantitative agreement with the measurements.

Regarding the deposition and desorption of low work function compounds some models already exist in the literature [12]-[14], [16], [18]. All these models are derived from or consist in modifications of the model firstly proposed by Longo in Ref [13].

In the model in Ref [13] the evolution of the surface coverage is related to the balance between the desorption of barium atoms from the emitter surface due to thermal desorption and their replenishment through Knudsen flow from inside the pores. The characteristic energies relative to these two processes are derived tuning the model to data from travelling wave tubes.

In the model in Ref [13] and in the others in [12], [14], [16], [18] the desorption term includes only thermal desorption of the low work function compounds neglecting ion sputtering.

In addition, in these models the energy required for the desorption of one adsorbed barium atom varies from author to author from a value of 2 eV [11] up to 6 eV [17] showing how the chemistry of the insert surface is still not well understood [17].

The model presented in this thesis is not derived from the one proposed in Ref. [13].

In this model, using some data found in the Russian literature [19], the main low work function compound will be identified as Ba_3WO_6.

The process relative to the formation and destruction of Ba_3WO_6 is reported in several papers (for example [19]-[21]). In all these papers it is shown how the formation and destruction of Ba_3WO_6 involve a BaO molecule and not a Ba atom and the energy needed to activate such process is about 7 eV.

Starting from the identification of the low work function compound a deposition and desorption model will be derived and coupled with the barium oxide depletion model.

The deposition and desorption model will also be coupled with a semi-empirical procedure to update the plasma parameters to include the effects that a modification in the surface coverage will produce on the hollow cathode plasma.

Using the deposition/desorption model and the procedure to update the plasma parameters the evolution of the surface coverage and of the insert work function with time can be calculated.

Comparing the data obtained simulating the cathode in Ref [22] with the experimental results an end of life criterion will be derived according to which the end of life of a cathode is reached when during the start-up phase the insert is not able to produce enough BaO to reach a full surface coverage of low work function compounds. The desorption/deposition model, the plasma update procedure and the end of life criterion will be subsequently applied to the NSTAR cathode finding life time prediction that are in agreements with the expectations (since no data regarding the end of life of the NSTAR exist).

The whole modelling process is reported in the diagram below

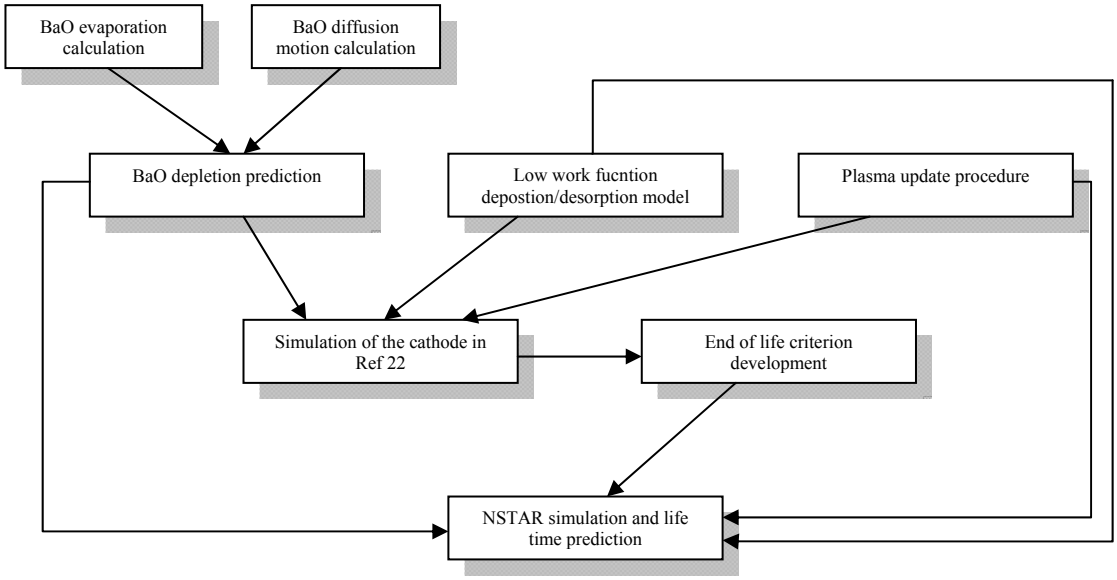

Figure 2 – Modelling flowchart

The barium oxide depletion model together with the deposition/desorption model, with the procedure to update the plasma parameter and with the end of life criterion will constitute the most advanced and complete model for the prediction of hollow cathode lifetime.

2 Literature review

In this chapter the most important papers regarding hollow cathode lifetime measurements and modelling will be reviewed and commented on. The papers will be divided into experimental and theoretical papers whereas a different section will be dedicated to the papers dealing with plasma models.
At the end of the review a conclusion section will be present where gaps present in the literature will be pointed out and the path that this thesis must follow will be defined indicating also the most important paper that will be used in the thesis development.

2.1 Experimental papers

T. R. Sarver-Verhey [22], [23] presents a comprehensive analysis of the end-of-life scenario of a hollow cathode (similar to the one sketched in Figure 1) operated for 28,000 hours. In his analysis W and BaO deposition on the insert surface has been found respectively at the downstream and upstream end of the insert.
Tungsten deposition is believed to result from the condensation of free metallic tungsten that will occur only after the lowering work function capability of that area of the insert has been degraded due to the insert chemistry evolution. The level of degradation needed to start the process of condensation of free metallic tungsten is not discussed in this paper.
This tungsten deposition covers the previous formed layer of low work function compounds and, at the same time, occludes the insert pores preventing BaO production hence stopping the thermionic emission at the downstream end of the cathode and forcing the "discharge zone" to move upstream.
The deposition of barium oxide compounds is observed at the upstream end of the cathode; according to the author these compounds can stop the thermionic emission from the insert accelerating the formation of "poisonous compounds" that block the work function lowering process of the insert and stopping the barium oxide migration from the inner part of the insert to the surface.

At the end-of-life 70% of the surface is covered by these compounds as shown in Figure 3.

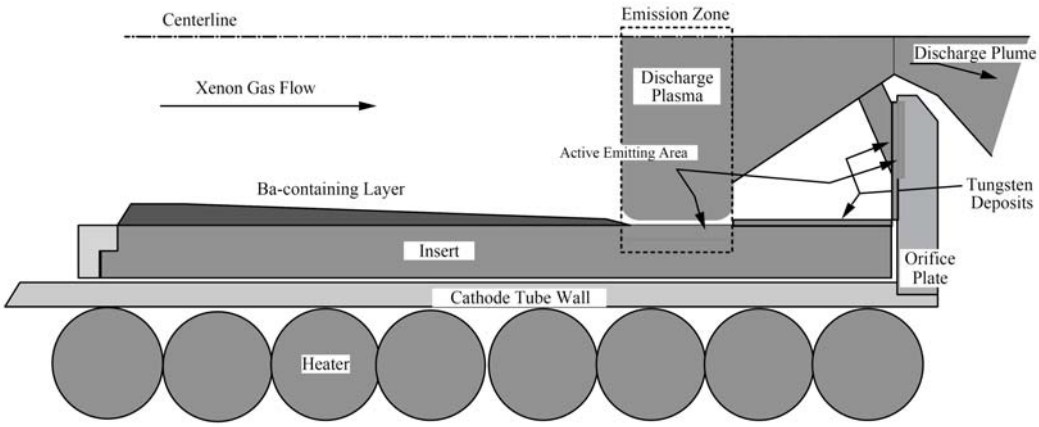

Figure 3 - End of life scenario showing Ba compounds and tungsten deposition [22]

The composition of the surface has been investigated by means of Scanning Electron Microscope (SEM) and X-Ray Diffraction (XRD) analysis, the results are reported in Figure 4. The main compounds found upstream are $BaWO_4$ and Ba_2CaWO_6

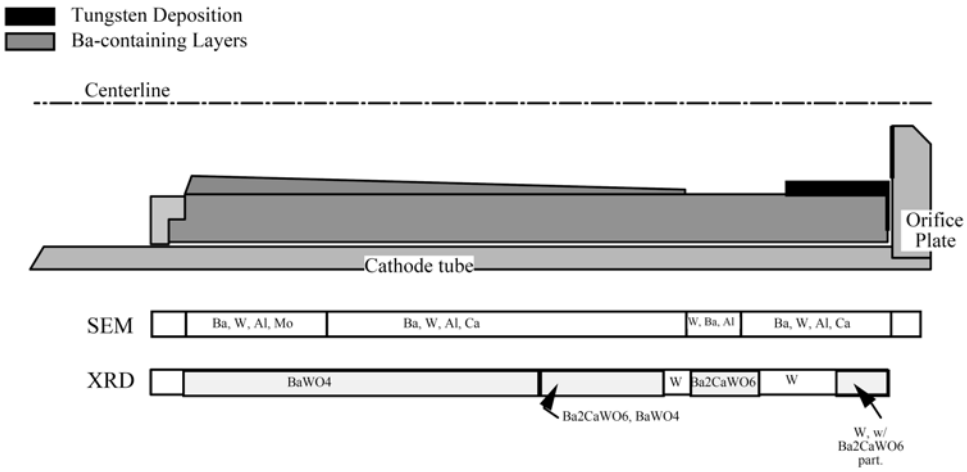

Figure 4 - SEM and XRD analysis showing the composition Ba and tungsten deposition [22]

Another important result of this analysis is that after 28,000 hours a large amount of barium is still present inside the insert. Sarver-Verhey explain this noting that the tungsten and barium compounds deposition on the surface may occlude the pores preventing barium evaporation and hence depletion.

The cathode tested in this paper has been defined “dead” after 28,000 hours. This end-of-life criterion is based on the impossibility of igniting the cathode within the power supply capabilities. During the ignition process utilized in this work the cathode is heated to a fixed temperature for a fixed period of time after which an increasing

voltage is applied until the discharge initiates. After 28,000 hours the value of this voltage went beyond the capability of the ignition power supply resulting in an ignition failure and so sentencing the "death" of the cathode (this does not necessarily mean that if the power supply was able to provide higher voltages the cathode would not have started). The ignition voltage trend with operational time is reported below.

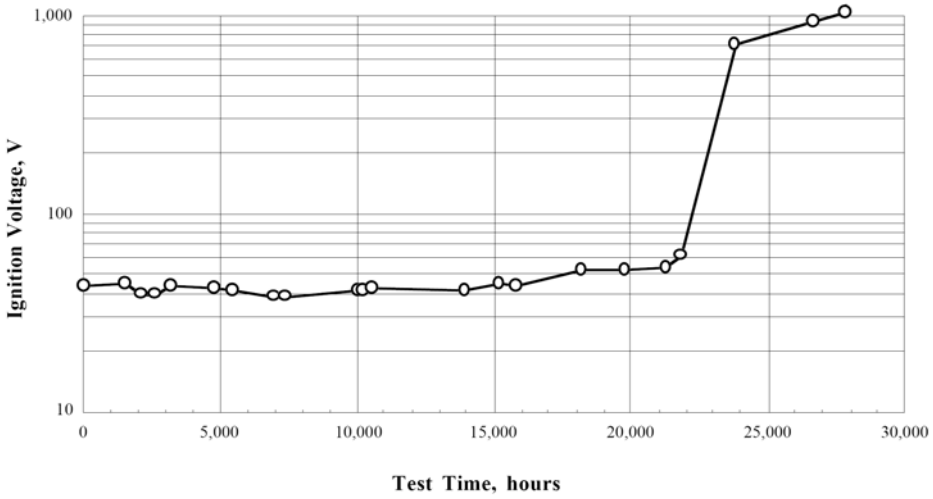

Figure 5 – Ignition voltage as a function of test time [23]

It can be noted how the end-of-life of the cathode occurs suddenly with the ignition voltage increasing from 60 to 1000 V in less than 5000 hours of operation. The author imputes this to a change in the emission characteristics of the insert. It must be also noted how the rapid increase in the ignition voltage presents two different slopes: a much steeper one at the beginning and a less steep one afterwards. This has not been commented by the author.

Kovalesky in Ref [24] presents a comprehensive review of all the testing performed on hollow cathodes at Nasa Glenn Research Center in support of the International Space Station plasma contactors up to October 2001. In this paper the results already reported by Sarver-Verhey in [22], [23] are presented. Together with this, the data relative to several other cathodes are presented.

The cathodes have been tested in different conditions to simulate all the possible operating conditions onboard of the ISS. They were tested at variable current demands and at constant high current; ignition testing has also been performed.

Four of the cathodes have accumulated more the 12,000 hours of functioning respectively HCA.003 has accumulated 12,415 hours, HCA.013 18,823 hours, HCA.010 15,876 hours and the cathode from [22] has accumulated 28,000 hours. Only

two of these cathodes failed to ignite, HCA.003 after 12,415 hours and the one reported in Ref [22] after 28,000 hours while all the other tests were stopped intentionally.

The failure of the HCA.003 cathode was imputed to an insert failure that is supposed to be caused by the cracking of the insert after vibration testing prior to the operational testing whereas the cathode tested by Sarver-Verhey has been already discussed above.

In all the tests reported in this paper the ignition of the cathode has been done by heating the cathode with a fixed heater power and applying a constant voltage until the discharge does not initiate. The time needed to ignite the cathode has been recorded and used as an end of life criteria.

The ignition time of the HCA.003 is reported below

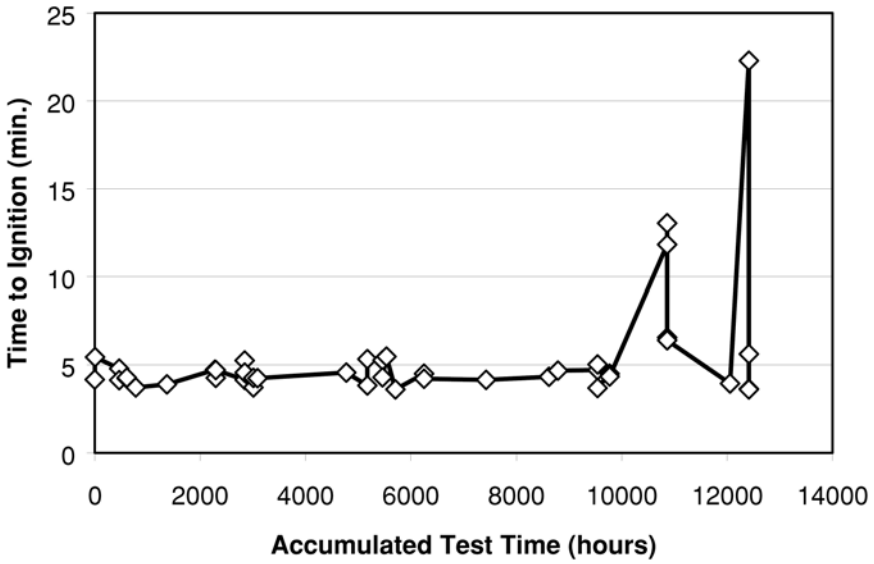

Figure 6 – Ignition time for the HCA.003 cathode [23]

As in Figure 5 a sudden increase of voltage occurs at the end of life here a sudden increase of the ignition time is present. In this case this sudden increase has been considered as an end-of-life criteria and the HCA.003 has been considered dead. To investigate the causes of the cathode death its insert has been then removed and mounted in a new cathode. This cathode failed to ignite too, demonstrating that the insert is to be considered the cause of the failure.

Sengupta's paper [2] presents a lot of data regarding barium content inside the insert of the ELT discharge cathode from the Deep Space One flight spare ion engine after the 30,000 hours life test.

After 30,372 hours the cathode test has been voluntary interrupted and the cathode insert has been sectioned and analyzed.

Using EDX the author has measured Ba/W ratio in various points, as reported in Figure 7, showing how after 30,372 hours of operation at least 30% of the initial barium content is still present confirming what already noticed by Sarver-Verhey in [22], [23].

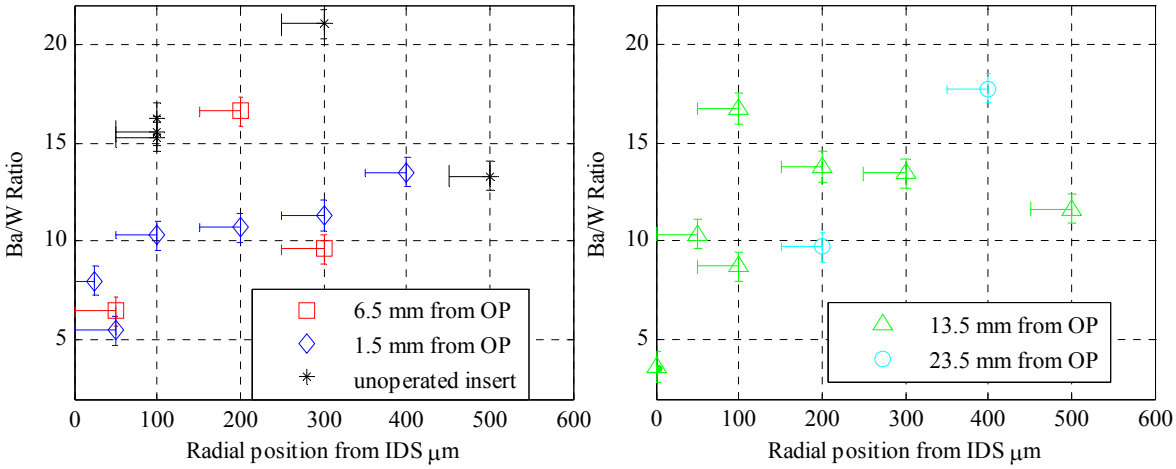

(a) (b)

Figure 7 – Ba/W ratio value for different radial and axial position [2]

From this data she has also extrapolated the depletion depth that is found to vary between 400 μm at the downstream end to 100 μm at the upstream one although how this has been defined is not clear from the paper. The depletion depth trend is reported below

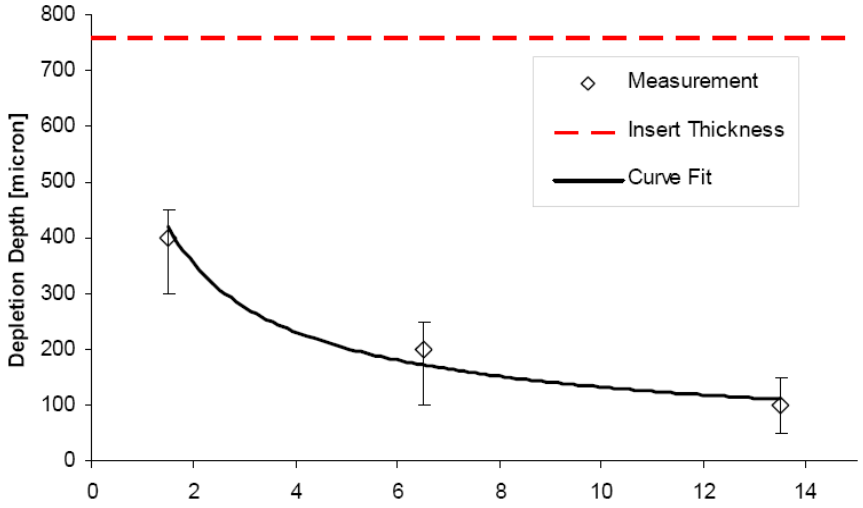

Figure 8 - Depletion depth along the insert length [2]

Another important result presented in this paper is the presence of W and BaO deposition on the surface of the tantalum tube that encloses the insert. This is evidence of how barium oxide evaporation and escape from the insert does not occur only from the inner and upstream surface (that are obviously "free" not being enclosed or covered

by anything) but also from the outer one that at a first glance seems to be "closed" since it is enclosed by the cathode tube.

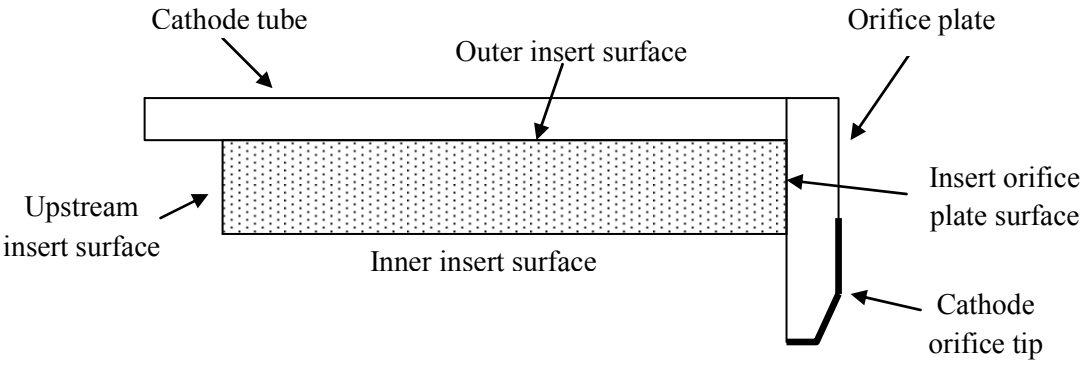

Figure 9 – HC insert surface definition

Roquais [10] focussed on barium depletion depth measurements using different insert porosities and temperatures. To measure depletion depth he used a porous disk of tungsten impregnated with a 4:1:1 BaO-CaO-Al_2O_3 compositions welded in a "cup" so that barium oxide can evaporate only from one surface; in this way he was able to obtain depletion profiles that are almost perfectly one dimensional. Also in this paper barium depletion from an enclosed surface is observed. Roquais experimental apparatus and depletion data are shown in Figure 10-Figure 12.

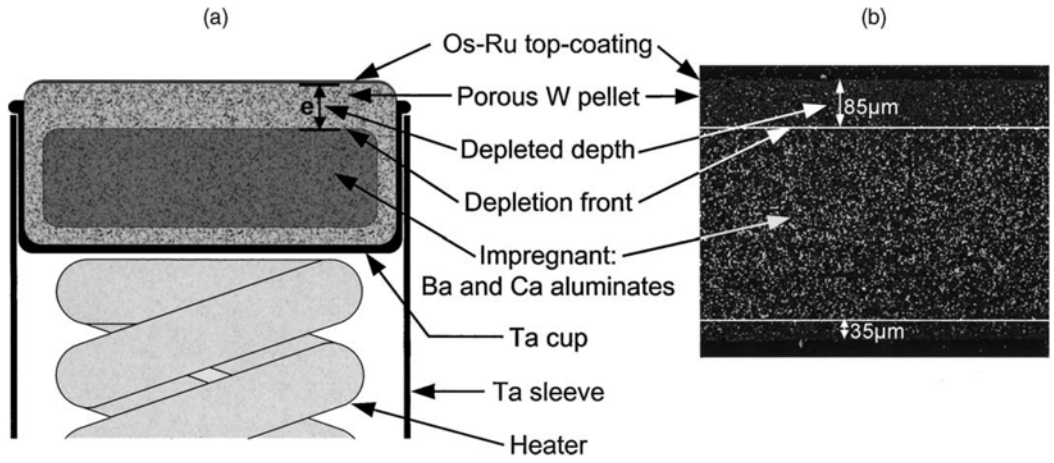

Figure 10 - Experimental apparatus (a) and EDX image of the emitter (b) showing a 2-side depletion [10]

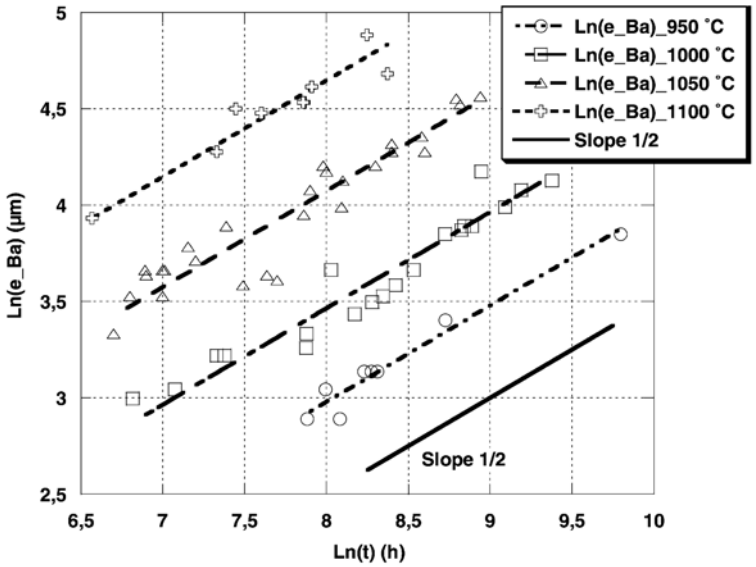

Figure 11 - Measure depletion depth versus time at different temperatures [10]

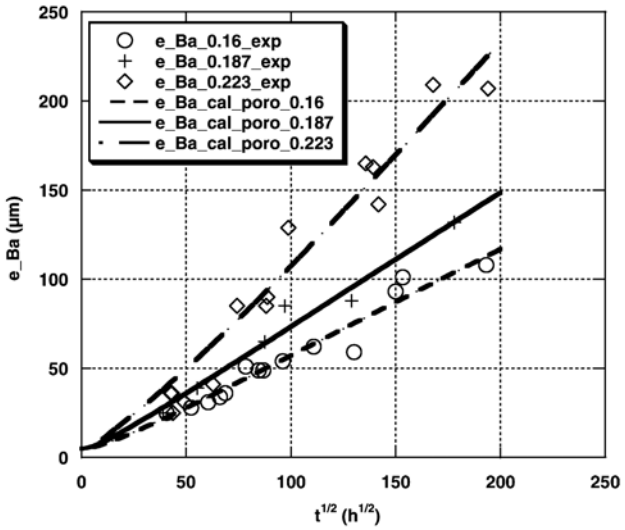

Figure 12 - Ba depletion as a function of the square root of time for three different porosities of tungsten pellet at a cathode operating temperature of 1000 °C [10]

Polk et al. [25] have measured the temperature profile along the insert on the NSTAR cathode for all the different throttle levels used by NASA (Figure 13). They have also shown how the orifice size influences the temperature profile: the bigger is the orifice the higher is the insert temperature (Figure 14).

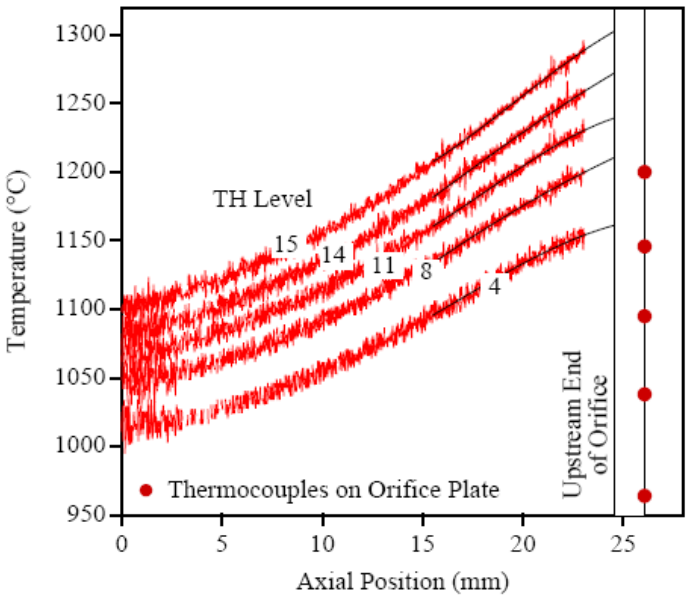

Figure 13 – Nstar insert Temperature profile at different throttle levels [25]

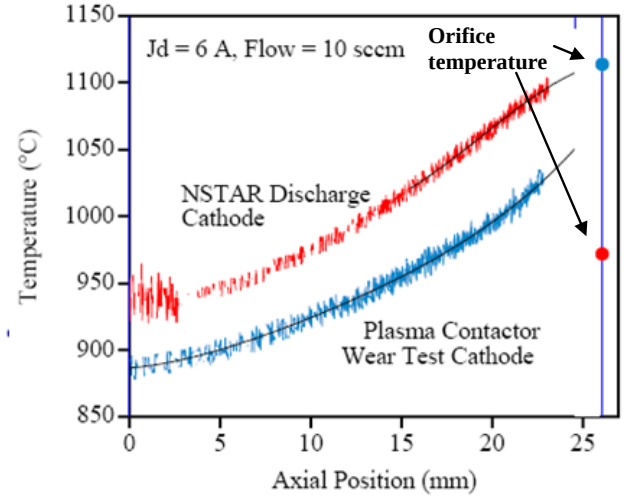

Figure 14 – Different insert temperature profile for different orifice sizes (bigger for the NSTAR, smaller for the Plasma Contractor Wear Test Cathode) [25]

This has been explained noting that a bigger orifice produces a smaller pressure increase inside the cathode cavity close to the orifice plate. A lower pressure means a lower local density hence a lower ionization rate; this implies a lower electron production from the ionization processes and so requires higher insert temperatures to produce the missing electrons by thermionic emission

Other useful data regarding the NSTAR cathode have been published by Goebel et al in , [4], [26] where the electron density, cathode voltage drop and electron temperature for different throttle levels have been measured.

The papers by Appendino [20], Wolten [27] and Resulhina [21] mainly present data related to the insert chemistry.

In Ref [21] there is a comprehensive list of the reactions that can produce Ba and BaO and of the reactions that form the low work function compound.
Appendino [20] and Wolten [27] focused their attention on the behaviour of the BaO-CaO-Al_2O_3 ternary system drawing the complete system diagram at 1250 °C and indicating all the possible compounds that can be found in it.
All the data contained in these papers has been collected and summarized by Lipeles and Kahn [28].
The papers by L. Chang [29], B. Phillips [30], and E. Kreidler [31] present data regarding phase relations in the systems W – O, BaO – WO_3 , CaO – WO_3 and of the ternary system BaO – CaO – WO_3 .
In Ref [19] a comprehensive study of the thermionic properties of the alkali tungstates is presented including the work functions values of most of the barium-tungsten compounds and their trends with temperature.

2.2 Theoretical papers

2.2.1 Lifetime and barium depletion modelling papers

In Ref [28] a model that deals with the BaO-CaO-Al_2O_3 system behaviour is derived. In this model the strongly non linear behaviour of the insert chemistry is shown (i.e. how evaporation rate depends on local barium oxide concentration) but this model does not include the diffusion process that supplies barium oxide to the surface. No comparison with experimental data is presented.
In the paper by Jensen [11] , the barium diffusion process is modelled in detail but the complex chemistry of the BaO-CaO-Al_2O_3 system is neglected assuming that the only reaction that produces gaseous barium oxide is solid barium oxide evaporation.
The author of this paper also calculated the barium diffusion coefficient defining it as the product of the probability that a barium atom has enough energy to "jump" out of its location inside the crystalline structure (characterized by E_m) times the probability that the target jump site is vacant (characterized by E_f) multiplied by the vibration frequency and by the jump separation squared (where the jump separation is the distance between the location where the atom is and the target jump site).

$$D_a = \frac{1}{6}\nu\,(2R_{Ba})^2\, e^{-\frac{E_m+E_f}{k_b T}} \tag{3}$$

where ν is the frequency of vibrations calculated from the minimum of the Lennard-Jones potential, R_{Ba} is the atomic radius of barium, E_m the energy of vaporization of barium (assumed to be 1.45 eV) and E_f the energy relative to the jump of a barium atom from one vacancy to another (0.8 eV).

Roquais [10] in his paper shows how the depletion depth is related to the square root of the time (Figure 11 and Eq. (4) where δ is the depletion depth and a an experimental constant)

$$\delta = a\, t^{1/2} \tag{4}$$

and develops a model that includes the diffusion process and how the diffusion coefficient is related to the insert porosity, analytically deriving a linear relation between the two. Again the model neglects the BaO-CaO-Al_2O_3 chemistry.

Kovalesky [12] develops a model of the insert taking into account the BaO-CaO-Al_2O_3 chemistry but without taking into account the BaO diffusion inside the insert (all the barium oxide is always available at the surface for evaporation).

In this paper a model to treat Ba and BaO diffusion inside the hollow cathode cavity is also presented but it does not include the possibility of BaO dissociation into atomic barium and oxygen and the possibility that these atomic species can be ionized.

Longo in Ref. [13] and [14] presents a model for the lifetime of dispenser thermionic cathode.

In this model the evolution of the surface coverage is related to the balance between the desorption of barium atoms from the emitter surface due to evaporation and their replenishment through free molecular flow from inside the pores where barium is generated.

This process can be described by Eq. (5) where the first term represents the supply of barium from the insert core through free molecular flow whereas the second one represents the desorption of barium from the surface as the ratio between the surface coverage and a characteristic desorption time (that will be derived by comparison with experimental results).

$$\frac{d\theta}{dt} = \frac{E_0\, e^{\frac{-q\epsilon}{k_b T}}}{\sqrt{1+\gamma t}}(1-\theta) - \frac{\theta}{\tau} \tag{5}$$

where ϵ is the energy involved with the evaporation of barium inside the insert and the consequent free molecular flow, γ is a coefficient that takes into account the time scale of this flow, τ is the characteristic desorption time, θ is the surface coverage defined as the ratio between the part of the surface covered with low work function material over the total insert surface, and where the term $1-\theta$ has been introduced to limit the surface coverage to one.

In fact if $\theta \rightarrow 1$ the first term in the right hand side of Eq. (5) tends to zero and hence the desorption rate becomes the only term in the equation avoiding the construction of multiple layers of barium.

The value of γ has firstly assumed to be constant in [13] whereas in [14] it has been assumed to be proportional to the barium vapour pressure through a constant κ

$$\gamma = \kappa \frac{p(T)}{\sqrt{T}} \tag{6}$$

This model has then been tuned to lifetime data relative to travelling wave tubes (TWT) determining the values of γ, ϵ, τ and κ and showing a very good agreement with the experimental data.

A TWT is an electronic device used to amplify radio frequency signal to high power. It consists mainly of an elongated vacuum tube with an electron gun at one end. The role of the electron gun is to produce electrons that are then accelerated through the vacuum tube. To produce electrons the electron gun makes use of a thermionic dispenser (that, except for the geometry, is equal to a hollow cathode insert).

Even if also in TWT tubes a thermionic dispenser (insert) is present the environment in which this will operate is different from the one present in a hollow cathode. In fact inside TWT there is no plasma but only electrons that are accelerated away from the dispenser. This means that the insert surface chemistry is not influenced by ion and electron bombardment and that the total current is provided only by the thermionic emission whereas in hollow cathodes the ion and electron fluxes to the surface are important in the total current calculation and the ions flowing back to the cathode surface, being accelerated to electron volt level energies by the sheath voltage drop, will produce a certain sputtering rate of the low work function material hence influencing the evolution of the surface coverage.

From this we can infer that this model being validated with TWT data is not directly applicable to hollow cathodes.

In addition to this in this model the chemistry of the BaO-CaO-Al_2O_3 system has not been taken into account.

In Ref [13] and [14] the relation between the low work function material surface coverage and the surface work function has been derived as

$$\phi(\theta) = \phi_m \left(\frac{\Gamma\phi_m}{\phi_{Ba}}\right)^{\frac{\Gamma\theta}{1-\Gamma}} + \phi_{Ba}\left[1 - \left(\frac{\Gamma\phi_m}{\phi_{Ba}}\right)^{\frac{\theta}{1-\Gamma}}\right] \tag{7}$$

Where ϕ_m is the bare metal work function that is a function of time and of the surface concentration of the matrix metal and ϕ_{Ba} is the barium work function (2.5 eV) and is a constant. The parameter Γ determines the values of coverage corresponding to the minimum of the work function and can be determined finding the zero of the first derivative of Eq. (7) at any time given the minimum value of the work function. The minimum value of the work function is commonly determined from experimental measurement.

In Ref. [15] Tighe presents a model for hollow cathode ignition. In this model the barium vapour pressure p_0 has been assumed to be relative to only one reaction (solid barium oxide evaporation) and to be constant with time.

The barium oxide pressure at the surface has then been assumed to decay in time with $t^{1/2}$ according to the results obtained by Roquais [10]. The BaO pressure trend has been assumed to take the form

$$p = p_0\left(1 - \sqrt{\frac{t}{\Omega(t)}}\right) \tag{8}$$

Where $\Omega(t)$ is an empirically determined function of the form

$$\Omega(t) = C_1\, e^{\frac{C_2}{T}} \tag{9}$$

The low work function surface coverage is then determined using an equation similar to Eq. (5).

The ignition of the cathode is assumed to be characterized by electron emission from the cathode orifice tip (Figure 9). From the knowledge of the surface coverage and of the barium oxide vapour pressure evolution with time the coverage obtained at the end of the start up time is calculated. From this value of the coverage the work function of the cathode tip and the thermionic emitted current are calculated. It is not clear how the ignition voltage is derived from these parameters.

The constants C_2 in Eq. (9) have been obtained from comparison with TWT tubes data whereas the value of C_1 has been obtained matching the calculated values of the ignition voltage to the ones reported in [23] and in Figure 5.
No other comparison with experimental data is reported so the goodness of the model cannot be judged.

2.2.2 Plasma modelling papers

In the literature there are many models for the plasma inside the hollow cathode.
The most relevant models have been developed by Siegfried and Wilbur [32] , Salhi and Turchi [7], Katz et al [33], Rossetti et al. [34] and by Mikellides et al [5], [6], [35], [36].
The model by Siegfried and Wilbur was developed after a series of experiments on hollow cathodes operating on mercury. This model relies on empirically derived relationships and on the specification of a fixed value of the electron temperature T_e derived from the related experiments. For these reason its applicability to Xenon hollow cathodes over a wide range of operating parameters is considered problematic hence it will not be discussed further.
The model in Ref [7] by Salhi and Turchi is derived from first principles.
The model is two dimensional in the plasma potential whereas densities, temperatures, and hence the pressures, are assumed to be constant inside the cathode. In this model the neutral gas temperature is assumed to be equal to the wall temperature and the ion particle density is assumed to be equal to the electron particle density (quasineutrality) reducing the unknowns to 7 scalar unknowns (the values of n, n_n, T_e, T_i, T_w, p and of the emission length L defined as the length of that part of the cathode surface that emits thermionically) plus the plasma potential V that is function of both the radius and axial distance.
In this model the ion and electron fluxes to the cathode surface are calculated as

$$J_i = qn\left(\frac{k_b T_i}{2\pi m_i}\right)^{\frac{1}{2}} \qquad J_e = qn\left(\frac{k_b T_e}{2\pi m_e}\right)^{\frac{1}{2}} e^{-\frac{q\Delta V}{k_b T_e}} \tag{10}$$

And the thermionic emitted current is calculated including the field enhancement effect.
Where the surface field is calculated through the relation derived by Prewett and Allen [37]

$$E = \frac{k_b T e}{q\lambda_D}\sqrt{4\nu_i\eta_0[(1+\eta_c/\eta_0)^{1/2}-1] - 2J_b(2\eta_c)^2 + 2e^{-\eta_c} - 2} \tag{11}$$

where ν_i, η_0, η_c, J_b are non dimensional parameters relative to the electron temperature, thermionic emission and cathode voltage fall.

This relation has been approximated by Siegfried and Wilbur for conditions in a hollow cathode

$$E = \sqrt{\left(\frac{nk_bT_e}{\epsilon_0}\right)\left[2\left(1+2\frac{q\Delta V}{k_bT_e}\right)^{1/2}-4\right]} \tag{12}$$

To derive the densities and the temperatures the set of algebraic equation reported below have been solved

$$\begin{aligned}\int J_{th}\left(\phi_{eff}+\frac{5kT_e}{2q}\right)dA = \int J_e\left(\phi_{eff}+\frac{5kT_w}{2q}\right)dA + \\ + \int J_i\left(E_{ion}+\Delta V-\phi_{eff}\right)dA + fq_r\end{aligned} \tag{13}$$

$$n\left(\frac{n}{n_0}\right)^{\frac{T_i}{T_e}} = \frac{2Z_i}{Z_0}\left(\frac{2\pi m_e k_b T_e}{h^2}\right)^{3/2} e^{\frac{-E_{ion}}{k_bT_e}} \tag{14}$$

$$\begin{aligned}\int J_{th}\left(\Delta V+\frac{5kT_w}{2q}\right)dA + \int \eta J^2 dV = \int J_e\left(\frac{5kT_e}{2q}\right)dA + \\ + \int J_i\left(E_{ion}+\frac{5kT_i}{2q}\right)dA + (I_D+I_{eq})\left(\frac{5kT_e}{2q}\right) + I_{eq}\left(\frac{5kT_e}{2q}\right) + q_r\end{aligned} \tag{15}$$

$$p = (n+n_0)k_bT_i\left(1+\alpha\frac{T_e}{T_i}\right) \tag{16}$$

$$\dot{m} = \frac{p}{4\sqrt{\frac{k_bT_i}{m_i\left(1+\alpha\frac{T_e}{T_i}\right)}}} \tag{17}$$

$$\int \left(J_{th}+J_i-J_e\right)dA = I_D \tag{18}$$

Eq. (13) represents the power balance at the cathode surface. The LHS represents the thermionic cooling power including both the energy spent for the "evaporation" of an electron and the fraction of thermal energy leaving with the "evaporated" electron.

The first term of the RHS represents the electron heating effect assuming that every electron arriving at the cathode surface is reabsorbed.

The second term of the RHS represents the ion bombardment heating. This is calculated assuming that the energy gained by the ion in the sheath is much higher than its temperature and that every ion impacting on the surface recombines with one of the cathode electrons hence subtracting from the surface an energy equal to ϕ_{eff} and transferring to the surface the energy liberated during the recombination (E_{ion}). The last term represents the radiative heat exchange between the plasma and the cathode surface.

Eq (14) is a two temperature Saha equation used to derive the particle densities from the ionic and electronic temperatures.

Eq (15) represents the power balance inside the plasma column. The terms of the LHS indicated respectively the power input due to the thermionic emitted electron entering the plasma column and the power generated by ohmic heating.

In the RHS the power losses due to ion and electron fluxes to the cathode surfaces and to particles flowing out of the cathode and the radiative heat exchanged with the cathode surface are represented.

Eq. (16) and (17) are respectively the ideal gas law written for the plasma inside the cathode and the calculation of the mass flow rate assuming that the orifice size is much smaller than the cathode cavity so that the flow is sonic in the orifice.

Eq (18) is the current balance on the cathode surface where I_D is the total discharge current.

The plasma potential inside the plasma is then calculated solving the Laplace equation for a neutral plasma

$$\nabla^2 V = 0 \tag{19}$$

Eq. (19), being derived assuming quasineutrality, is not suitable to describe the sheath regions. The effect of the sheath is implicitly included in the Eq. (19) through the boundary conditions.

$$\begin{aligned} \frac{\partial V}{\partial x} &= \begin{cases} \eta J_{or} & at \quad 0 \le r \le R_{or} \quad and \quad x = L_c \\ 0 & at \quad R_{or} \le r \le R_c \quad and \quad x = L_c \\ 0 & at \quad 0 \le r \le R_c \quad and \quad x = 0 \end{cases} \\ \frac{\partial V}{\partial r} &= \begin{cases} \eta(J_{th} + J_i + J_e) & at \quad 0 \le L \le L_c \quad and \quad r = r_c \\ 0 & at \quad 0 \le L \le L_c \quad and \quad r = 0 \end{cases} \end{aligned} \tag{20}$$

The presence of the sheath region is implicitly included through the presence of the thermionic current (J_{th}) and of the electron back-streaming (J_e) current. In fact the thermionic emitted current depends on the sheath voltage drop through the presence the Schottky effect correction for the effective work function as in Eq (2) and (12) whereas the back-streaming electron current depends on the sheath voltage drop since only the electrons that possess an energy higher than the sheath potential can reach the cathode surface (Eq. (10)).

The results obtained with this model have been compared with the experimental measurements reported in another paper by the same authors [38].

Comparison between the computed and measured trends of the cathode wall temperature, cathode pressure, electron temperature, plasma density and plasma voltage with the cathode current shows a very good agreement with a maximum discrepancy of 30% in the electron temperature and plasma number density trends.

The model developed by Katz et al [33] deals with the plasma inside the cathode orifice. The model is mainly one-dimensional with the exception of the particle density whose radial profile is derived once the axial profile is known.

The main assumptions are quasi-neutrality, the use of Poiseuille flow for the neutrals and that the ion flow is diffusion limited because of the very short mean free path for resonant CEX collisions.

The main equations used in this model are:

- the three mass conservation equations for neutrals, ions and electrons,

$$\begin{aligned} \nabla \cdot v_0 n_0 &= -\dot{n} \\ \nabla \cdot v_i n &= \dot{n} \\ \nabla \cdot v_e n &= \dot{n} \end{aligned} \tag{21}$$

where $\dot{n}$ is the ion generation rate

$$\dot{n} = 4\sigma(T_e) n\, n_0 \sqrt{\frac{qT_e}{2\pi m_e}} \tag{22}$$

- the Poiseuille flow relation for neutral velocities where ζ is the Xenon viscosity and R the cathode radius

$$v_0 = -\frac{R^2}{8\zeta}\frac{dp}{dx} \tag{23}$$

- the combination of the momentum equation for ions and electrons

$$n(v_i - v_0) = -\left(D_i + \frac{\mu_i}{\mu_e} D_e\right)\frac{\partial n}{\partial z} - \frac{\mu_i}{\mu_e} n\, v_e \tag{24}$$

where D_e, D_i and D_a indicate the electron, ion and ambipolar diffusion coefficients defined as

$$\begin{aligned} D_e &= \tau_e \frac{qT_e}{m_e} \\ D_i &= \tau_i \frac{qT_i}{m_i} \\ D_e &= \tau_i \frac{q}{M}\frac{T_e + T_i}{v_{scat}} \end{aligned} \tag{25}$$

where v_{scat} is the ion scattering speed.

- The steady state electron energy equation

$$\nabla \cdot \left(\frac{5}{2} + \kappa \nabla T_e \right) + \eta J_e^2 = \dot{n} q E_{ion} \tag{26}$$

Once the axial profiles of all the variables are know the radial profile of the particle density has been calculated solving the ambipolar diffusion equation

$$-\nabla \cdot (D_a \nabla n) = \dot{n} \tag{27}$$

The model has been also applied to the insert region to calculate the plasma number density inside the cathode cavity. This has been done solving the ambipolar diffusion equation but is not clear if in this calculation any modification has been done to Eq. (27) to take into account the electron input from thermionic emission from the cathode surface or not.

The model by Rossetti et al [34] is still a one-dimensional model. In it quasi-neautrality is assumed, the neutral flow is described through a Poiseuille flow relation and the ions and neutrals temperatures are assumed to be equal to the wall temperature.

The main equations in this model are the energy balance in the plasma and in the cathode body, the Poiseuille flow relation for the neutrals, the current balance in the plasma column and on the cathode body and Ohm's law. All these equations have been written in their differential form constituting a differential equation system of five first-order and one second order equation. This system has been solved numerically with a shooting technique.

In this paper the cathode temperature calculated with the model has been compared to the measured profiles showing a good agreement. No other comparison with experimental values is present in this paper.

The last model that we will review is the one developed at JPL by Mikellides, Polk, Katz and Goebel [5], [6], [35], [36].

This model has undergone several improvements and refinements and in its final version is a full 2D-axisymmetric time dependent model of the hollow cathode including both the cathode cavity and the plume region.

The only input required by this model is the shape of the cathode temperature profile that the model will automatically shift up or down to meet the thermionic emission requirements at the insert surface.

In this model the only assumptions made are $n_i = n_e$ (quasi-neutrality), that neutrals and ions have the same temperature, and that the gas pressure is equal to a given value p_g (how the value of p_g is obtained is not specified in the paper but we could suppose that it is obtained from measurements).

The model consists in the solution of a system of seven differential equations obtained from the combination of mass conservation, momentum and energy equations for ions, electron and neutrals plus two algebraic equations for the pressure calculation and the total current balance.

$$
\begin{aligned}
\mathbf{j_i} &= \frac{m_e}{m_i}\frac{\nu_{en}}{\nu_{in}+\nu_{iz}}\mathbf{j_e} - \frac{q\nabla(nk_bT_i + nk_bT_e)}{m_i(\nu_{in}+\nu_{iz})} \\
\nabla \cdot v_i n &= \dot{n} \\
-\nabla\cdot\left(\frac{5}{2}T_e\mathbf{j_e} + \kappa_e\nabla T_e\right) &= \mathbf{E}\cdot\mathbf{j_e} - 3nk_b(T_e-T_i)\frac{m_e}{m_i}(\nu_{ei}+\nu_{en}) - qE_{ion}\dot{n} \\
\nabla\cdot\left(\frac{5}{2}T_i\mathbf{j_i} - \kappa_N\nabla T_i\right) &= \mathbf{v_i}\cdot\nabla(nqT_i) + 3nk_b(T_e-T_i)\frac{m_e}{m_i}(\nu_{ei}+\nu_{en}) + nm_i\nu_{in}v_i^2 \\
\nabla\cdot\left(\frac{\nabla V}{\eta}\right) &= \nabla\cdot\left[\frac{\nabla(nT_e)}{\eta n} + \left(1-\frac{\nu_{ei}}{\nu_{ei}+\nu_{en}}\right)\mathbf{j_i}\right] \\
\mathbf{j_e} &= \frac{\nabla(nT_e)}{\eta n} + \frac{\mathbf{E}}{\eta} - \left(1-\frac{\nu_{ei}}{\nu_{ei}+\nu_{en}}\right)\mathbf{j_i} \\
\mathbf{E} &= -\nabla V \\
p_g &= k_bT\left[n_n + n\left(1+\frac{T_e}{T_i}\right)\right] \\
I_D &= I_{th} - I_e + I_i
\end{aligned}
\tag{28}
$$

In Eq. (28) the quantities in bold are vectors, ν are the collision frequencies, ν_{iz} the ionization collision frequency, κ is the thermal conductivity of the plasma and η the plasma resistivity. The system is solved numerically discretizing the solution domain in finite volumes where all the vectors are defined on the cell edges and all the scalars in the cell centers.

The outputs of this model have been tested with a number of experimental values showing an extremely good agreement with measured particle densities, electron temperature and plasma voltages.

2.3 Literature review conclusions

In this chapter the most relevant papers regarding HC lifetime modelling and measurements have been presented.

As already said in the introduction three are the main aspect that a model must be able to catch to predict the hollow cathode lifetime:

1) barium oxide depletion from the HC insert
2) the evolution of the low work function surface coverage on the insert

3) the effects that a change in the surface coverage will produce on the hollow cathode plasma

As it could be seen from the literature review reported above at present a model that include all these three aspects does not exist, to be more precise the first two aspects (BaO depletion and surface coverage evolution) are still not well understood and modelled.

In fact regarding BaO depletion all the models present in the literature either neglect the complex chemistry of the $BaO\text{-}CaO\text{-}Al_2O_3$ system or, when this is taken into account, they neglect the barium oxide diffusion motion inside the insert.

Regarding low work function surface coverage evolution we must note how the models currently available [12], [14], [16], [18] are all based on the semi-empirical approach used by Longo in [13]. Moreover the data used to tune the model reported in [13] are relative to TWT devices and not to hollow cathodes hence this model is, in principle, not directly applicable to hollow cathodes.

Talking about point 3 we must note how, to be able to capture the effect that a change in the surface coverage will produce on the plasma, we need a model that at least provides us with the plasma parameter trend along the cathode axis (a full 3D cylindrical simulation would be ideal).

In the literature many models regarding the plasma inside an HC exists [5]-[7], [32]-[36]. In particular the most accurate and comprehensive is the one developed at JPL [5], [6], [35], [36].

The problem regarding this model is the impossibility of obtaining access to it (due to ITAR regulations) and its level of complexity that makes almost impossible to replicate it starting from what is published in the literature.

The model developed by Rossetti et al. [34] is also quite complicated and, in addition to this, there are no sufficient evidences in the literature of its accuracy (the only comparison found in the literature is between computed and experimental data is relative to the wall temperature [34]) to justify the effort needed to replicate it.

The model by Turchi and Salhi [7] is easy and quick to implement but unfortunately does not provides the trends of all the plasma parameter inside the cathode since all the parameters, except the plasma potential, are assumed to be constant inside the cathode.

From what is said above the path that this thesis must follow appears clear: first a model able to predict BaO depletion from the HC insert will be developed taking into account both the $BaO\text{-}CaO\text{-}Al_2O_3$ system chemistry (using the data in [20], [21], [27], [28]) and

the diffusion motion of BaO inside the insert (using the data reported by Roquais [10] and theory presented in [11] relatively to the diffusion coefficient); second a surface coverage evolution model will be developed including both thermal desorption of the low work function compound (evaporation) and ion sputtering (using the data in [19], [29]-[31]), third a way to derive the effect that a change in the surface coverage have on the plasma parameter will be developed starting from the experimental measurements reported in [3], [4], [25], [26] and the model developed by Salhi and Turchi [7].

3 Barium depletion modelling [39] [40]

As already pointed out in the literature review, at present no barium oxide depletion model that takes into account both the dependency of barium oxide evaporation rate on the local BaO concentration and the BaO diffusion motion through the pores has been published.

In this chapter the model developed to predict BaO depletion from hollow cathode insert will be presented.

This model is the first that takes into account both the BaO diffusion motion and the relation between BaO evaporation rate and local BaO content.

The model will be firstly formulated in a mono-dimensional case and will be then generalized to the case of 3-D cylindrical geometry.

The model will consist of two parts: one that will evaluate barium oxide evaporation rate from the surfaces taking as an input the local concentration and another one that will calculate how BaO migrates from the inner part of the insert to the surfaces.

For both of these parts of the model the temperature of the insert will be taken as an input together with the initial distribution of BaO inside the tungsten matrix.

3.1 $BaO\text{-}CaO\text{-}Al_2O_3$ ternary system diagram

Barium oxide depletion from the insert is the result of the complex chemistry of the $BaO\text{-}CaO\text{-}Al_2O_3$ ternary system so its knowledge and understanding is the basis for the development of a depletion model. The ternary diagram of the $BaO\text{-}CaO\text{-}Al_2O_3$ system at 1250 °C is shown in Figure 15, Figure 16.

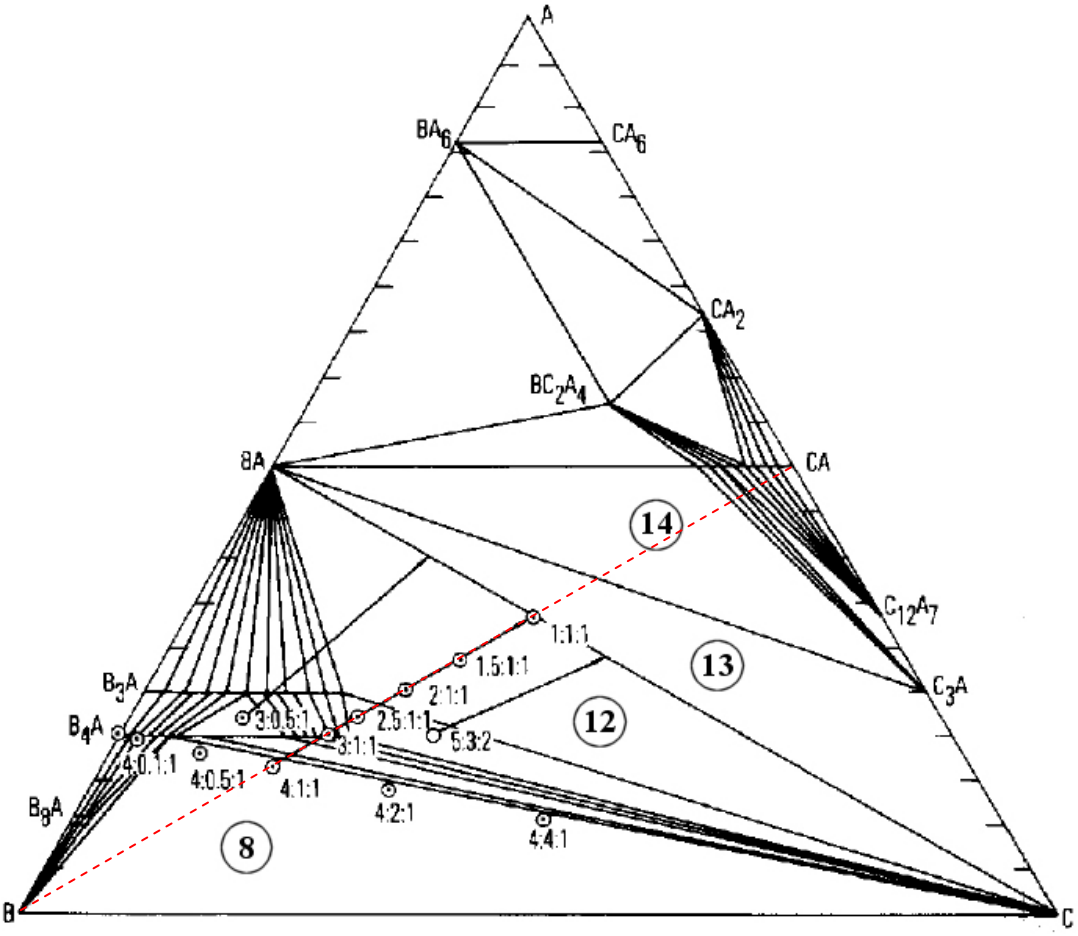

Figure 15 - BaO-CaO-Al2O3 phase diagram at 1250 °C[28]

In this diagram the letters A, B and C stand for Al_2O_3, BaO and CaO respectively. Each of the three corners represents a molar concentration of 100% of one of these three fundamental compounds (the one displayed near the corner).

Each point of the diagram represents a particular composition where the concentration of A, B and C are inversely proportional to the distance of the point from each corner.

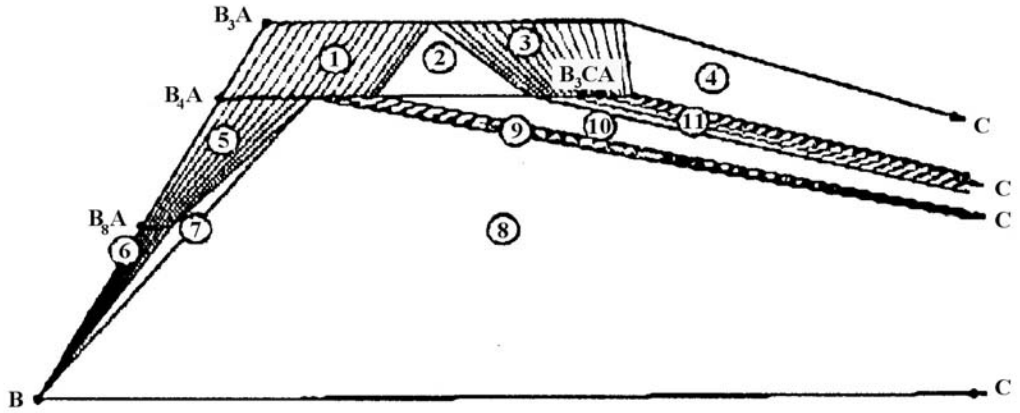

Figure 16 - Particular of the BaO-CaO-Al_2O_3 phase diagram [20]

Each of the areas in which the diagram is divided represents a particular state of the system i.e. which compounds are present.

The empty areas stand for states in which the compounds stoichiometric coefficients are fixed and do not vary with the composition while the filled ones stand for states in which the stoichiometric coefficients of the compounds change with the composition.

In most of the BaO-CaO-Al_2O_3 compounds barium oxide can be partially substituted by calcium oxide because of their similar atomic configuration, when this happens we will refer to these compounds as solid solution (s.s.).

For example the expression $B_{4-x}C_xA$ means that in the B_4A compound x molecules of barium oxide have been substituted by calcium oxide and will be indicated as "B_4A s.s".

Below there is a list of all the compounds present in the most important areas of the diagram

Table 1 - Compounds present in each area of the ternary diagram [20], [27].

Area N°	Compounds	Area N°	Compounds
1	B_3A s.s. and B_4A s.s.	8	B, C and $\overline{B_4A}$ s.
2	$\overline{B_3A}$ s.s., $\overline{B_4A}$ s.s. and $\overline{B_3CA}$	9	C and $\overline{B_4A}$ s.s.
3	B_3A s.s. and B_3CA s.s.	10	C, $\overline{B_4A}$ s.s. and $\overline{B_3CA}$ s.s.
4	C, $\overline{B_3A}$ s.s. and B_3CA s.s.	11	C and $\overline{B_3CA}$ s.s
5	B_4A s.s. and B_8A s.s.	12	C, B_3A and BA
6	B and B_8A s.s.	13	C, BA and C_3A
7	B, $\overline{B_4A}$ s.s. and $\overline{B_8A}$ s.s.	14	AB, C_3A and CA

The barred formulae refer to a well-defined composition of the corresponding solid solution

Once we know which compounds are present and which are their stoichiometric coefficients, using the conservation of atomic species we can calculate the final composition.

Given an area of the diagram where all the compounds have a fixed composition (empty area) the state of the system can be represented as

$$Y_1 \cdot B_{S_{11}} C_{S_{21}} A_{S_{31}} + Y_2 \cdot B_{S_{12}} C_{S_{22}} A_{S_{32}} + Y_3 \cdot B_{S_{13}} C_{S_{23}} A_{S_{33}} \tag{29}$$

The conservation of mass implies that

$$\begin{bmatrix} S_{11} & S_{12} & S_{13} \\ S_{21} & S_{22} & S_{23} \\ S_{31} & S_{32} & S_{33} \end{bmatrix} \begin{Bmatrix} Y_1 \\ Y_2 \\ Y_3 \end{Bmatrix} = \begin{Bmatrix} f_1 \\ f_2 \\ f_3 \end{Bmatrix} \tag{30}$$

where f_1, f_2, f_3 are the absolute concentration of BaO, CaO and Al_2O_3.

From Eq. (30) we can calculate the stoichiometric coefficients of the compounds as

$$Y = S^{-1} f \tag{31}$$

For example a 2:1:1 composition corresponds to area number 12 of the diagram so the compounds present are C, B_3A and BA. The concentrations are $f_{BaO} = 2$, $f_{CaO} = 1$, $f_{Al_2O_3} = 1$ hence Eq. (30) becomes

$$\begin{bmatrix} 0 & 3 & 1 \\ 1 & 0 & 0 \\ 0 & 1 & 1 \end{bmatrix} \begin{Bmatrix} Y_1 \\ Y_2 \\ Y_3 \end{Bmatrix} = \begin{Bmatrix} 2 \\ 1 \\ 1 \end{Bmatrix} \tag{32}$$

Whose solution is

$$\begin{Bmatrix} Y_1 \\ Y_2 \\ Y_3 \end{Bmatrix} = \begin{Bmatrix} 1 \\ 1/2 \\ 1/2 \end{Bmatrix} \tag{33}$$

Hence the final composition is found to be $C + \frac{1}{2}B_3A + \frac{1}{2}BA$ or the equivalent $CaO + \frac{1}{2}Ba_3Al_2O_6 + \frac{1}{2}BaAl_2O_4$.

If we are in one of the filled areas and the state of the system can be represented as

$$Y_1 \cdot B_{S_{11}} C_{S_{21}} A_{S_{31}} + Y_2 \cdot B_{S_{12}-x} C_{S_{22}+x} A_{S_{32}} \tag{34}$$

From the conservation of mass we have

$$\begin{cases} Y_1 S_{11} + Y_2 (S_{12} - x) = f_1 \\ Y_1 S_{21} + Y_2 (S_{22} + x) = f_2 \\ Y_1 S_{31} + Y_2 S_{32} = f_3 \end{cases} \tag{35}$$

Adding these three equations we can obtain all the unknowns

$$\begin{Bmatrix} Y_1 \\ Y_2 \end{Bmatrix} = \begin{bmatrix} S_{11} + S_{21} + S_{31} & S_{12} + S_{22} + S_{32} \\ S_{31} & S_{32} \end{bmatrix}^{-1} \begin{Bmatrix} f_1 + f_2 + f_3 \\ f_3 \end{Bmatrix} \tag{36}$$

$$x = \frac{Y_1 S_{11} + Y_2 S_{12} - f_1}{Y_2} \tag{37}$$

3.2 Barium oxide evaporation rate calculation

As can be easily inferred barium oxide evaporation is strongly dependent on which compounds are present on the surface and so on the local composition.

Below there is a list of the most important reactions that lead to barium oxide evaporation

Table 2 - Most important reactions in barium oxide evaporation [20], [21], [26]

Reactions	ΔH [eV]	ΔS [J/mol]
$BaO(s) \rightarrow BaO(g)$	4.3224	137.85
$1/5\ Ba_8Al_2O_{11}(s) \rightarrow s)\ Ba) + 1/4\ Ba_4Al_2O_7(s)$	4.4267	130.72
$Ba_4Al_2O_7(s) \rightarrow s)\ 72) + Ba_3Al_2O_6(s)$	4.5789	122.76
$1/2\ Ba_3Al_2O_6(s) \rightarrow s)\ Ba) + 1/2BaAl_2O_4(s)$	4.6615	125.28
$6/5\ BaAl_2O_4(s) \rightarrow s)\ BaAlaO(g)Al_{12}O_{19}(s)$	5.6095	124.86
Decomposition of solid solution	ΔH [eV]	ΔS [J/mol]
$Ba_{8-0.2}Ca_{0.2}Al_2O_{11}$	4.4267	130.47
$Ba_{4-1.1}Ca_{1.1}Al_2O_7$	4.5789	122.05
$Ba_{3-0.75}Ca_{0.75}Al_2O_6$	4.6615	122.93

Where ΔH and ΔS represent the enthalpy and entropy of the reactions.

To calculate the barium oxide evaporation rate some hypotheses have been formulated:

- since the ternary diagram is known only at 1250 °C we will assume that it will not change appreciably in the range 900 – 1300 °C so that its application is possible to the study of hollow cathodes inserts.
- since no data regarding the kinetic of the chemistry of the ternary system has been found we will assume to be always in local thermodynamic equilibrium. This hypothesis can be justified noting that the scale of the problem we are dealing with is of the order of tens of thousands of hours hence the effects of non-equilibrium chemistry should be quite small.
- since BaO tends to evaporate much more easily than CaO and Al_2O_3 we will neglect the evaporation rates of calcium oxide and alumina hence assuming to move along the dashed red line in Figure 15 as BaO evaporates. This can be justified noting that BaO is the most abundant compound in the impregnant and the easiest compound to vaporize and that in the literature only reaction involving evaporations of barium oxide from compounds containing BaO, CaO and Al_2O_3 have been found whereas evaporation of CaO and Al_2O_3 from such compounds has never been taken into account [28].

The calculation of barium oxide evaporation consists of four steps:

1) Given the concentration of BaO, CaO and Al_2O_3, referring to the diagram in Figure 15, Figure 16 and to Table 1, the compounds present can be determined and their concentration can be obtained.
2) Using the data in Table 2 the barium oxide pressure (in atmospheres) generated by each compound can be calculated as

$$p_{BaO_i} = e^{-q\frac{\Delta H_i}{kT}+\frac{\Delta S_i}{R}} \tag{38}$$

where the index *i* is used to label the pressure relative to the *i-th* compound.

3) The final barium oxide pressure can be calculated as

$$p_{BaO_{tot}} = \sum_{i=1}^{N} p_{BaO_i} X_i \tag{39}$$

Where X_i indicates the molar fraction of the *i-th* compound calculated as

$$X_i = \frac{Y_i}{\sum Y_i} \tag{40}$$

4) The barium oxide mass flow rate per unit area can be obtained using the Knudsen-Hertz-Langmuir formula

$$\dot{m}_{BaO} = \frac{p_{BaO_{tot}}}{\sqrt{\frac{2\pi RT}{M_{BaO}}}} 10^5 \tag{41}$$

This formula was derived by Langmuir by application of the principle of detailed balancing. This principle states that at equilibrium, the rates of all forward and reverse processes must be equal.

Thus, the rate of evaporation of a solid or liquid in contact with its equilibrium vapour is equal to the rate of impingement of molecules from the gas on the surface, which is calculable from gas kinetic theory, Langmuir then assumed that the vaporization rate remains unchanged when the equilibrium vapour is replaced by a vacuum.

Performing the four steps reported above it is possible to calculate how the barium oxide pressure and the mass flow rate for unit area behave with barium oxide content.

These values are plotted in Figure 17 starting from a 4:1:1 composition (i.e. mass fraction: 66.6% BaO, 16.6% CaO, 16.6% Al_2O_3) down to a 1:1:1 composition (i.e. mass fraction: 33% BaO, 33% CaO, 33% Al_2O_3).

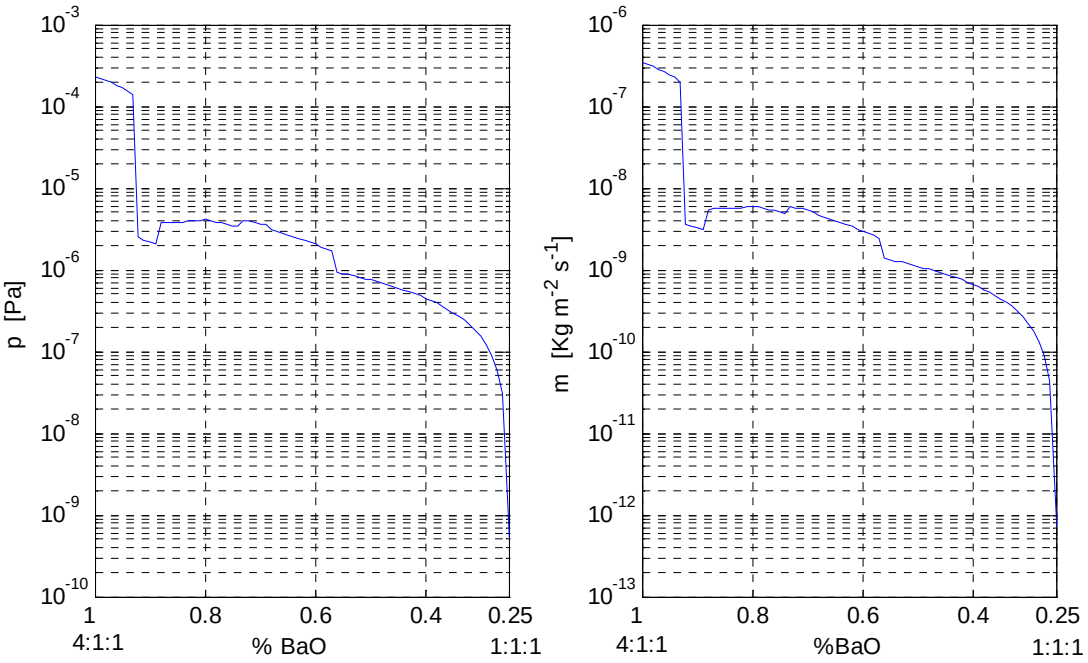

Figure 17 – Calculated BaO pressure and mass flow rate trend with barium oxide content

As we can see in Figure 17 the trend is strongly nonlinear and there are several orders of magnitude of difference between the BaO pressure and evaporation rate of a 4:1:1 composition and the ones of a 1:1:1.

It can also be noted how the mass flow and pressure trends present some discontinuities at about 93%, 88%, 74% and 57% of the initial BaO content.

These discontinuities are due to the fact that those concentrations correspond to the boundaries between different areas of the ternary diagram hence between different states of the system and so to those concentrations correspond the transition from one state of the system to another.

In reality these transitions are probably a smooth and gradual process but since we have no data regarding the kinetic chemistry of this system and we are forced to assume to be always in local chemical equilibrium, the transition between one state and another will happen suddenly changing instantaneously the compounds present and changing accordingly the evaporation rate producing such discontinuities.

Noting the strong non linearity of the mass flow rate trend we can state that the only way to evaluate barium oxide depletion from the insert is to know with the highest possible precision which compounds are present on the surface.

This can be made using the ternary diagram and the reaction given above, calculating at each time which compounds are present and their concentrations and coupling this with a model for barium oxide transfer from the inner part of the insert to the surface.

3.3 Barium oxide migration inside the insert

The motion of barium oxide from the interior part of the insert to the surface is the result of various different processes:

- Knudsen flow of gaseous Ba and BaO through the pores
- solid diffusion of Ba inside the BaO-CaO-Al_2O_3 impregnate
- solid diffusion of Ba inside tungsten
- surface diffusion of Ba along the pores surfaces

These processes are too complicated to be modelled in detail separately and, most of all, each of these is influenced by all the others so they will be represented globally with a single diffusion coefficient.

Ideally this diffusion coefficient is a function of local temperature, local BaO, CaO, Al_2O_3 and W concentration, and local matrix porosity.

Considering the difficulties of obtaining all these data for every point inside an insert and the actual lack of such detailed information the diffusion coefficient will be determined here with a simple theoretical approach [11] and later on §5.1.1 comparing the numerical result obtained with the 1-D model with the experimental measurements of barium oxide depletion published by Roquais [10].

In Ref [11] Jensen et al. have analytically modelled the bulk diffusion of barium. Their treatment is reported below.

Bulk diffusion is the result of the migration of barium atom inside the lattice of the impregnant and of tungsten. Barium atoms will migrate jumping from one vacancy to another inside the lattice. The "jump" is possible only if the atom has enough thermal energy and only if the target site in the lattice is effectively "vacant".

It can be easily shown that any diffusion coefficient is proportional to the ratio between the diffusion characteristic length squared and the characteristic time.

In fact taking a generic diffusion equation in the form

$$\frac{\partial}{\partial t} = D_a \frac{\partial^2}{\partial x^2} \tag{42}$$

And making it non-dimensional

$$\frac{1}{\tau}\frac{\partial}{\partial \tilde{t}} = D_a \frac{1}{L_{D_a}}\frac{\partial^2}{\partial \tilde{x}^2} \tag{43}$$

Noting that since the non dimensionalization $\frac{\partial}{\partial \tilde{t}}$ and $\frac{\partial}{\partial \tilde{x}^2}$ have the same order of magnitude we can write

$$D_a \propto \frac{L_{D_a}^2}{\tau} \tag{44}$$

if we now express the probability that an atom has enough thermal energy to jump from one vacancy to another and the probability that the target site is vacant respectively with the two activation energies E_m and E_f we can write the diffusion coefficient as

$$D_a = \frac{1}{6}\frac{L_{D_a}^2}{\tau} e^{-\frac{E_m+E_f}{kT}} \tag{45}$$

If we assume that the characteristic length is equal to the mean distance between the vacancies and that it can be approximated with $2R_{Ba}$ and that the characteristic time is the inverse of the vibration frequency of the atom around its lattice position Eq. (45) becomes

$$D_a = \frac{1}{6}\nu \left(2R_{Ba}\right)^2 e^{-\frac{E_m+E_f}{k_bT}} \tag{46}$$

Where the factor 1/6 takes into account the number of directions in which a jump can be made (in a cube).

The vibration frequency will be derived assuming that the atom vibrates about the minimum of the Lennard Jones potential

$$V(x) = 4E_m \left[\frac{1}{4}\left(\frac{R_{Ba}}{x}\right)^{12} - \frac{1}{2}\left(\frac{R_{Ba}}{x}\right)^{6}\right] \tag{47}$$

If the atom vibrates with a thermal energy equal to $\frac{1}{2}k_bT$ (considering a one dimensional vibration) the abscissa of the two extremes of the vibration can be found imposing

$$V(x) = \frac{1}{2}k_bT \tag{48}$$

Substituting Eq. (48) in Eq. (47) and solving, the abscissa of the extreme points of the vibration are

$$x_+ = R_{Ba}\left(1 - \sqrt{\frac{k_bT}{2E_m}}\right)^{-\frac{1}{6}} \quad x_- = R_{Ba}\left(1 + \sqrt{\frac{k_bT}{2E_m}}\right)^{-\frac{1}{6}} \tag{49}$$

Hence the amplitude of the vibration can be expressed as

$$a_\nu = x_+ - x_- \approx \frac{1}{6} R_{Ba} \sqrt{\frac{2k_b T}{E_m}} \tag{50}$$

Expanding $V(x)$ to the second order about its minimum and using the transit time calculated from the harmonic oscillator, the oscillation frequency can be derived as

$$\nu = \frac{1}{\pi a_\nu} \sqrt{\frac{k_b T}{2M_{Ba}}} \approx \frac{3}{\pi R_{Ba}} \sqrt{\frac{E_m}{M_{Ba}}} \tag{51}$$

Using Eq (46) and (51) the diffusion coefficient can be calculated.

The values of E_m and E_f are unknown. In Ref [11] it is proposed to use the value of the vaporization energy value of barium (1.45 eV) for both E_m and E_f. The value of D_a so obtained are reported below at different temperatures

Table 3 - Diffusion coefficient values according to Jensen et al. [11]

Temperature °C	D_a calculated from Eq (46). m^2/s
1100	$7.42 \cdot 10^{-16}$
1050	$3.61 \cdot 10^{-16}$
1000	$1.66 \cdot 10^{-16}$
950	$0.72 \cdot 10^{-16}$

This values will be used in section §5.1.1 as guess value to find the diffusion coefficient value that best fit the experimental data published in [10].

3.4 1-D insert model

Let's assume to have a one-dimensional insert impregnated with a mixture of barium calcium aluminates as shown in Figure 18

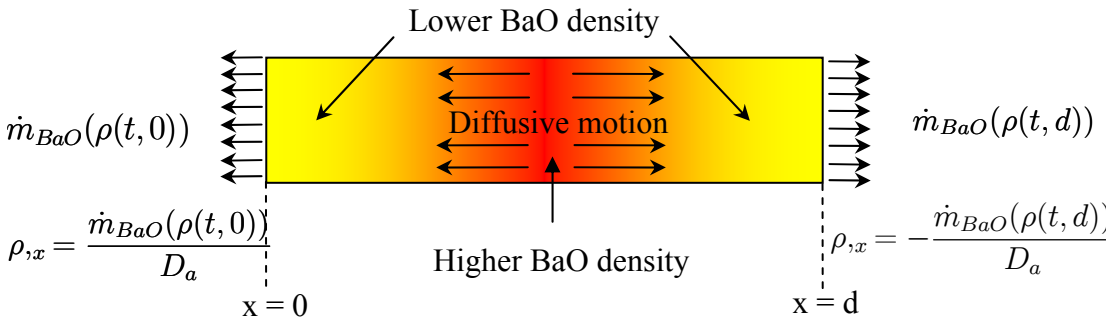

Figure 18 - One dimensional insert model

Due to the high temperature of the insert we have barium oxide evaporation from the free surfaces; this causes a barium oxide density gradient that gives rise to a diffusive motion of barium oxide inside the insert from its inner part towards the emitting surface. The problem we need to solve is therefore a diffusion problem where the unknown is the local barium oxide relative density. At the boundaries we have BaO evaporation calculated using the local concentration data together with the ternary diagram as explained in §3.2.

Using formulas we have

$$\begin{aligned} &\frac{\partial \rho}{\partial t} - D_a \frac{\partial^2 \rho}{\partial x^2} = 0 \\ &\rho(t=0,x) = \rho_0 \\ &\left.\frac{\partial \rho}{\partial t}\right|_{t,x=0} = \frac{\dot{m}(\rho(t,0))}{D_a} \\ &\left.\frac{\partial \rho}{\partial t}\right|_{t,x=d} = -\frac{\dot{m}(\rho(t,d))}{D_a} \end{aligned} \tag{52}$$

This system is strongly nonlinear because the boundary conditions depend on the solution itself through the presence of the mass flow rate that depends on the local BaO density (as shown in §3.2). Due to this strong nonlinearity no analytical solution exists so the system has been solved with an explicit finite difference method.

Such a numerical approach has been chosen for its simple implementation and for the easiness in generalizing it to a 3D case as will be done in §3.5.

The insert will be discretized in N+1 points so that point 0 corresponds to $x = 0$ and point N corresponds to $x = d$

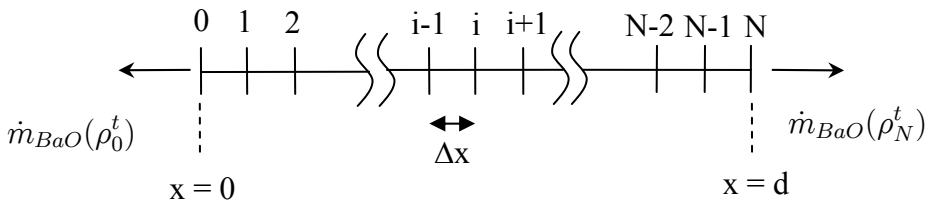

Figure 19 – mono-dimensional insert discretization

The derivative with respect to space and time are approximated as

$$\frac{\partial \rho_i^t}{\partial x^2} = \frac{\rho_{i+1}^t - 2\rho_i^t + \rho_{i-1}^t}{\Delta x^2} \qquad \frac{\partial \rho_i^t}{\partial t} = \frac{\rho_i^{t+1} - \rho_i^t}{\Delta t} \tag{53}$$

The system has been made dimensionless using the insert thickness *d* as characteristic length, the initial barium oxide density $\widehat{\rho}$ as characteristic density and defining the characteristic time so that the non-dimensional diffusion coefficient is 1 reducing the problem to the conventional form of the diffusion equation.

$$\widehat{\rho}\frac{\partial \rho_i^t}{\partial \widetilde{t}} = \frac{\tau}{d^2} D_a \widehat{\rho} \frac{\partial^2 \rho_i^t}{\partial \widetilde{x}^2} \qquad \tau = \frac{d^2}{D_a} \qquad \Downarrow \qquad \frac{\partial \rho_i^t}{\partial \widetilde{t}} = \frac{\partial^2 \rho_i^t}{\partial \widetilde{x}^2} \tag{54}$$

From now on unless specified we will always work with non dimensional quantities and so the superscript ~ will be omitted.

Barium oxide density inside the insert at the time step $t+1$ is calculated as

$$\rho_i^{t+1} = \rho_i^t + \frac{\Delta t}{\Delta x^2}\left(\rho_{i+1}^t - 2\rho_i^t + \rho_{i-1}^t\right) = \rho_i^t + \alpha\left(\rho_{i+1}^t - 2\rho_i^t + \rho_{i-1}^t\right) \quad i = 1...N-1 \tag{55}$$

This numerical method converges to a solution only if $\alpha = \frac{\Delta t}{\Delta x^2} < \frac{1}{2}$ (Appendix A), to obtain a good trade-off between precision and speed we have used $\alpha \leq 0.1$.

The boundary conditions are solved expanding the local BaO density in a second order Taylor series and then substituting into it the diffusion equation and the boundary condition itself (Appendix B) obtaining

$$\rho_0^{t+1} = \rho_0^t + 2\alpha(\rho_1^t - \rho_0^t) - \frac{\dot{m}(\rho_0^t)\, d}{D_a\, \widehat{\rho}} \frac{2\Delta t}{\Delta x}$$
$$\rho_N^{t+1} = \rho_N^t + 2\alpha(\rho_{N-1}^t - \rho_N^t) - \frac{\dot{m}(\rho_N^t)\, d}{D_a\, \widehat{\rho}} \frac{2\Delta t}{\Delta x} \tag{56}$$

Where $\dot{m}$ and D_a are the dimensional mass flow rate per unit area and diffusion coefficient.

3.5 3-D insert model

Once a one dimensional model has been developed it can be easily generalized to write a three dimensional cylindrical model.

Because of the cylindrical geometry we can reduce the 3D problem to a 2D problem on the r-z plane. This plane is sketched in Figure 20

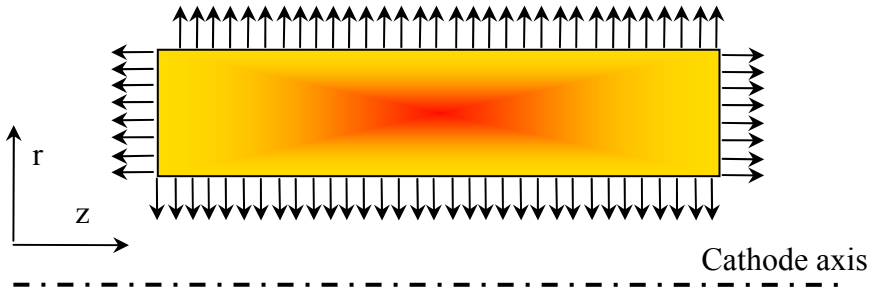

Figure 20 - 2-D insert model

In a cylindrical reference frame, the governing dimensional equations is

$$\frac{\partial \rho}{\partial t} - D_a \left(\frac{1}{r}\frac{\partial \rho}{\partial r} + \frac{\partial^2 \rho}{\partial r^2} + \frac{\partial^2 \rho}{\partial z^2} \right) - \frac{\partial \rho}{\partial z}\frac{\partial D_a}{\partial z} = 0 \tag{57}$$

where the derivatives with respect to θ have been neglected because of the symmetry and where D_a is now a function z because of the presence of a temperature profile along the length of the insert.

D_a do not depends from the radius r since the temperature profile is assumed to vary only with z being radially constant inside the insert.

The system can be non-dimensionalized using the insert thickness d as characteristic length, the maximum value of the initial density $\hat{\rho}$ as characteristic density, the maximum value of D_a as characteristic diffusion coefficient and where the characteristic time is calculated as in Eq (54).

The system has been the discretized as in Figure 21

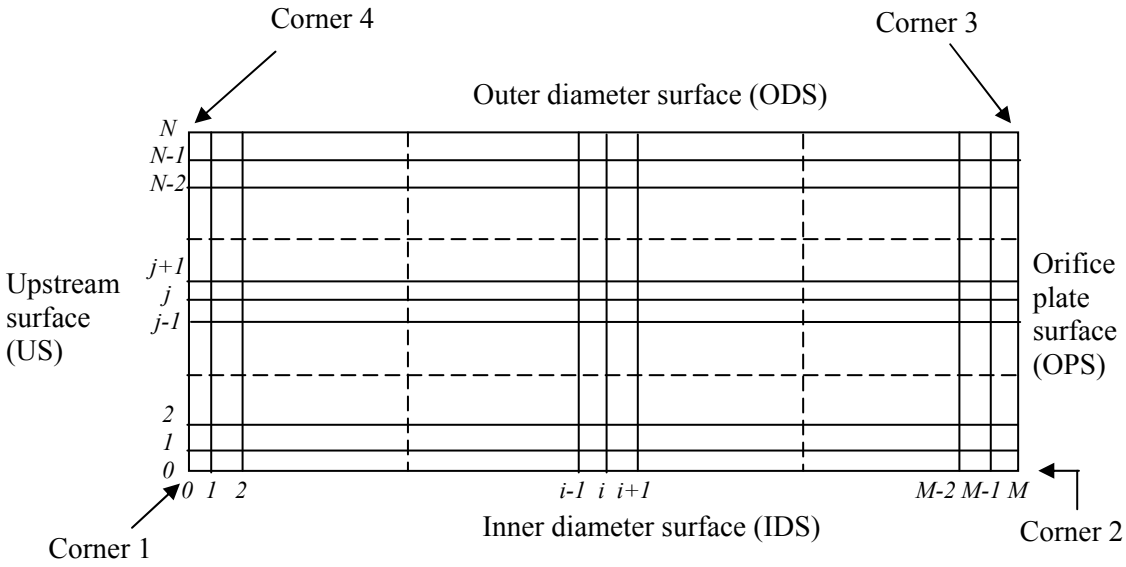

Figure 21 – Cylindrical insert discretization

It can be demonstrated that, using exactly the same method developed for the one dimensional case with a fixed space and time step, the algorithm still converges if $\alpha \leq 1/2$ and if the characteristic time is calculated using the maximum value of the diffusion coefficient.

The boundary conditions written with non dimensional quantities are (Appendix B)

- Upstream surface

$$\begin{aligned}\rho_{0,j}^{t+1} =& \rho_{0,j}^{t} + D_{a0,j}\left[2\alpha\left(\rho_{1,j}^{t} - \rho_{0,j}^{t} - \Delta x \frac{\dot{m}}{D_{a_{dim}0,j}}\frac{d}{\hat{\rho}}\right) + \right. \\ &+\alpha\left(\rho_{0,j+1}^{t} - 2\rho_{0,j}^{t} + \rho_{0,j-1}^{t}\right) + \left.\frac{\Delta t}{2r_j\Delta x}\left(\rho_{0,j+1}^{t} - \rho_{0,j-1}^{t}\right)\right] + \\ &+\Delta t \frac{D_{a1,j} - D_{a0,j}}{\Delta x}\frac{\dot{m}}{D_{a_{dim}0,j}}\frac{d}{\hat{\rho}}\end{aligned} \tag{58}$$

- Orifice Plate surface

$$\begin{aligned}\rho_{M,j}^{t+1} =& \rho_{M,j}^{t} + D_{aM,j}\left[2\alpha\left(\rho_{M-1,j}^{t} - \rho_{M,j}^{t} - \Delta x \frac{\dot{m}}{D_{a_{dim}M,j}}\frac{d}{\hat{\rho}}\right) + \right. \\ &+\alpha\left(\rho_{M,j+1}^{t} - 2\rho_{M,j}^{t} + \rho_{M,j-1}^{t}\right) + \left.\frac{\Delta t}{2r_j\Delta x}\left(\rho_{M,j+1}^{t} - \rho_{M,j-1}^{t}\right)\right] - \\ &-\Delta t \frac{D_{aM,j} - D_{aM-1,j}}{\Delta x}\frac{\dot{m}}{D_{a_{dim}M,j}}\frac{d}{\hat{\rho}}\end{aligned} \tag{59}$$

- Inner diameter

$$\begin{aligned}\rho_{i,0}^{t+1} =&\rho_{i,0}^{t} + D_{a\,i,0}\left[2\alpha\left(\rho_{i,1}^{t} - \rho_{i,0}^{t} - \Delta x\frac{\dot{m}}{D_{a_{dim}i,0}}\frac{d}{\hat{\rho}}\right) + \right.\\ &+\alpha\left(\rho_{i+1,0}^{t} - 2\rho_{i,0}^{t} + \rho_{j-1,0}^{t}\right) + \left.\frac{\Delta t}{r_{int}}\frac{\dot{m}}{D_{a_{dim}i,0}}\frac{d}{\hat{\rho}}\right] + \\ &+\alpha\frac{\rho_{i+1,0}^{t} - \rho_{i-1,0}^{t}}{2}\frac{D_{a\,i+1,0} - D_{a\,i-1,0}}{2}\end{aligned} \tag{60}$$

- Outer diameter

$$\begin{aligned}\rho_{i,N}^{t+1} =&\rho_{i,N}^{t} + D_{a\,i,N}\left[2\alpha\left(\rho_{i,N-1}^{t} - \rho_{i,N}^{t} - \Delta x\frac{\dot{m}}{D_{a_{dim}i,N}}\frac{d}{\hat{\rho}}\right) + \right.\\ &+\alpha\left(\rho_{i+1,N}^{t} - 2\rho_{i,N}^{t} + \rho_{j-1,N}^{t}\right) - \left.\frac{\Delta t}{r_{int}}\frac{\dot{m}}{D_{a_{dim}i,N}}\frac{d}{\hat{\rho}}\right] + \\ &+\alpha\frac{\rho_{i+1,N}^{t} - \rho_{i-1,N}^{t}}{2}\frac{D_{a\,i+1,N} - D_{a\,i-1,N}}{2}\end{aligned} \tag{61}$$

- Corner 1

$$\begin{aligned}\rho_{0,0}^{t+1} =&\rho_{0,0}^{t} + D_{a\,0,0}\left[2\alpha\left(\rho_{1,1}^{t} - \rho_{0,0}^{t} - \Delta x\frac{\dot{m}}{D_{a_{dim}0,0}}\frac{d}{\hat{\rho}}\right) + \right.\\ &+\left.\frac{\Delta t}{r_{int}}\frac{\dot{m}}{D_{a_{dim}0,0}}\frac{d}{\hat{\rho}}\right] + \Delta t\frac{D_{a\,1,0} - D_{a\,0,0}}{2}\frac{\dot{m}}{D_{a_{dim}0,0}}\frac{d}{\hat{\rho}}\end{aligned} \tag{62}$$

- Corner 2

$$\begin{aligned}\rho_{M,0}^{t+1} =&\rho_{M,0}^{t} + D_{a\,M,0}\left[2\alpha\left(\rho_{M-1,1}^{t} - \rho_{M,0}^{t} - \Delta x\frac{\dot{m}}{D_{a_{dim}M,0}}\frac{d}{\hat{\rho}}\right) + \right.\\ &+\left.\frac{\Delta t}{r_{int}}\frac{\dot{m}}{D_{a_{dim}M,0}}\frac{d}{\hat{\rho}}\right] - \Delta t\frac{D_{a\,M,0} - D_{a\,M-1,0}}{2}\frac{\dot{m}}{D_{a_{dim}M,0}}\frac{d}{\hat{\rho}}\end{aligned} \tag{63}$$

- Corner 3

$$\begin{aligned}\rho_{M,N}^{t+1} =&\rho_{M,N}^{t} + D_{a\,M,N}\left[2\alpha\left(\rho_{M-1,N-1}^{t} - \rho_{M,0}^{t} - \Delta x\frac{\dot{m}}{D_{a_{dim}M,N}}\frac{d}{\hat{\rho}}\right) + \right.\\ &+\left.\frac{\Delta t}{r_{int}}\frac{\dot{m}}{D_{a_{dim}M,N}}\frac{d}{\hat{\rho}}\right] - \Delta t\frac{D_{a\,M,N} - D_{a\,M-1,N}}{2}\frac{\dot{m}}{D_{a_{dim}M,N}}\frac{d}{\hat{\rho}}\end{aligned} \tag{64}$$

- Corner 4

$$\begin{aligned}\rho_{0,N}^{t+1} =&\rho_{0,N}^{t} + D_{a\,0,N}\left[2\alpha\left(\rho_{1,N-1}^{t} - \rho_{0,N}^{t} - \Delta x\frac{\dot{m}}{D_{a_{dim}0,N}}\frac{d}{\hat{\rho}}\right) - \right.\\ &-\left.\frac{\Delta t}{r_{int}}\frac{\dot{m}}{D_{a_{dim}0,N}}\frac{d}{\hat{\rho}}\right] + \Delta t\frac{D_{a\,1,N} - D_{a\,0,N}}{2}\frac{\dot{m}}{D_{a_{dim}0,N}}\frac{d}{\hat{\rho}}\end{aligned} \tag{65}$$

3.6 Barium oxide depletion modelling conclusions

Barium oxide depletion is the result of the combination of BaO evaporation from the insert surfaces and of the BaO diffusive motion inside the insert.

The first model that takes into account both the chemistry of the BaO-CaO-Al_2O_3 system and barium oxide diffusion inside the insert has been presented. The chemistry of the system has been explained pointing out the simplification made (the assumption of local thermodynamic equilibrium and the neglection of CaO and Al_2O_3 evaporation rates) and justifying them.

From the analysis of the BaO-CaO-Al_2O_3 system it has been shown how the BaO evaporation rate is extremely dependent on what kind of compounds are present on the pore surface hence on the local BaO concentration. From this it can be stated that the assumption according to which the evaporation of BaO is only the product of the reaction $BaO_{(s)} \rightarrow BaO_{(g)}$ (as done in most of the model published up to now [11], [12], [14]) is an oversimplification of the problem since, as shown in Figure 17, the variation of the BaO content from a 4:1:1 to a 1:1:1 composition due to BaO depletion will affect the evaporation rate lowering it by several order of magnitude.

A model to predict barium oxide diffusion inside the insert has been found in the literature and has been reported and will be used later on to obtain guess values for the BaO diffusion coefficient.

A one-dimensional model to simulate the evaporation of BaO and BaO diffusion (hence BaO depletion) has been written and a numerical scheme to solve it has been found; this model has been then generalized to a 3D model with cylindrical symmetry.

With the one-dimensional model a sensitivity analysis on the diffusion coefficient will be performed to match the numerical predicted barium depletion to the experimental data reported in Ref [10]. With this procedure the diffusion coefficient value can be calculated; the results will be reported in §5.1.1. The values of the diffusion coefficient so obtained will be then used in the 3D cylindrical model.

The cylindrical model will be validated comparing the numerical data with the experimental results to the NSTAR cathode [2] and to the QinetiQ Artemis T5 cathode [41] showing both qualitative and quantitative agreement. This comparison will be reported in §5.1.3 and §5.1.4.

4 Low work function compounds deposition and desorption [42][43]

In this chapter the processes relative to low work function compounds deposition and desorption from a hollow cathode insert surface will be presented and quantified.

In a hollow cathode due to the evaporation of BaO from the insert and its subsequent deposition on the emitter surface low work function compounds are formed.

These compounds lower the emitter surface work function from the value characteristic of the emitter material (for tungsten $\phi = 4.5\ eV$) down to about 2 eV allowing for the high current emission densities normally measured in hollow cathodes.

This deposition process is hindered mainly by two desorption mechanism: thermal desorption of the low work function compounds and ion sputtering.

During cathode life the evaporation rate of BaO from the insert tends to decrease due to the gradual depletion of BaO, with a consequential decrease of the low work function deposition rates.

Since the desorption mechanism, assuming constant insert temperature and plasma characteristics, will remain roughly constant in time this reduction in BaO evaporation rate will result in a reduction of the area covered by low work function compounds and hence in an increase of the average work function.

This process leads to a reduction of the thermionic current from the emitter that, in turn, will force the cathode to operate at a higher temperature increasing the BaO thermal desorption rates. This process will continue up to the point where the cathode is no longer able to operate.

The presence of low work function material on the cathode surface is also important during the ignition process, in fact during the ignition the electrons emitted from the cathode surface will lower the inter electrode resistance hence lowering the voltage needed to ignite the cathode.

It is then clear how the understanding of the evaporation and deposition process involving BaO and of the processes that results in low work function desorption from the surface is key in predicting the lifetime of the cathode.

In the next sections the main low work function compounds will be identified and the effects of calcium on the low work function compound characteristics will be qualitatively presented starting from the data found in Chang [29], Phillips[30],

Kreidler[31]. After that the main processes relative to low work function desorption and deposition will be analyzed starting from the data published by Resulhina[21], Bondarenko [19] and on some of the results found by Langmuir [44]-[48] .

4.1 Low work function compounds identification

Low work function compounds are the result of the interaction between barium, oxygen and tungsten.

During experimental studies it has been shown that on the activated surface of a tungsten cathode two layers exists. An oxygen layer is formed directly over the tungsten whereas on top of the oxygen a barium layer is formed [17].

Both the barium and the oxygen atoms are thought to be chemically bonded with the underlying layer (chemisorpted) with bonds between oxygen and tungsten much stronger than those between oxygen and barium [17].

These chemical bonds are still not well understood [17], [22], [23] for example the energy needed for the desorption of a bonded Ba atom is different from paper to paper.

It has been found and is commonly accepted that these three elements tend to react forming $BaWO_4$ and Ba_3WO_6 [21] even if the time needed for their formation is unknown.

In the american literature these compounds are normally indicated as “poisonous compounds” due to their very high temperature resistance (very low rate of barium released from them) and to the fact that they are commonly thought to provide no significant thermionic emission [49] .

The statement about their very low emission capability has first been found in a paper from the 50s by Huges et al. [49] whereas in this paper the value of the work function of these compounds is not reported. In the 60s Bondarenko published a paper in Russia [19] where the work function of the most important compounds formed by tungsten, oxygen and barium have been measured. These values are reported below in Table 4 assuming a linear trend of the work function with the temperature of the compound.

$$\phi = \phi_0 + \frac{d\phi}{dT}T \tag{66}$$

Table 4 - Barium – tungsten compounds work function [19]			
Compound	ϕ eV T=1100 °K	ϕ_0 eV	$\frac{d\phi}{dT}$ eV·K^{-1}
Ba_3WO_6	2.00	1.33	$6.09 \cdot 10^{-4}$
Ba_2WO_5	2.42	1.02	$12.72 \cdot 10^{-4}$.
$BaWO_4$	3.34	2.27	$9.72 \cdot 10^{-4}$

The overall work function trend with temperature of the surface of a tungsten emitter impregnated with BaO-CaO-Al_2O_3 has been derived by Palluel and Shroff [50] measuring the emitted current as a function of temperature and then, using the Richardson-Dushmann relation (Eq. (1)) and including the Schottky effect (Eq. (2)), calculating the effective work function. The values of the work function so derived are commonly used in the plasma model developed at JPL [5], [6], [36]; the derived work function trend with surface temperature is then

$$\phi = 1.41 + 5 \cdot 10^{-4} T \tag{67}$$

As it can be easily noted this trend is very close to the one of Ba_3WO_6 reported in Table 4. Plotting the work function relative to this compound together with the one in Eq (67) for various values of temperature (Figure 22) it can be found how the discrepancy between these two tends to increase with increasing temperatures.

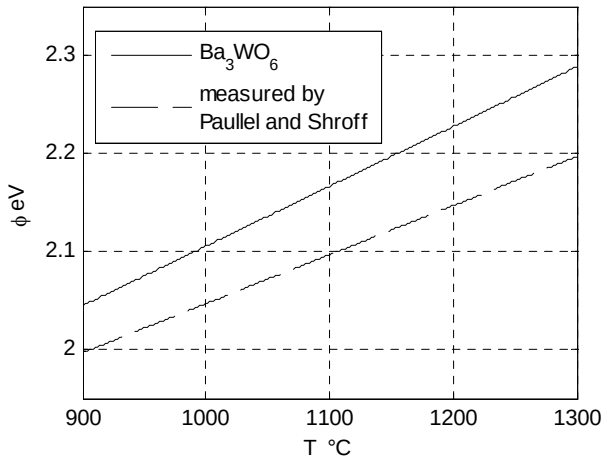

Figure 22 - Comparison between the measured HC work function and the one relative to Ba_3WO_6

If we consider that in normal conditions a cathode will operate at temperature below 1300 °C the maximum difference between the work function reported in Eq. (67) [50] and the one relative to Ba_3WO_6 is about 0.1 eV equivalent to 4% of the measured value.

If the data in Ref [19] are accurate Ba_3WO_6 seems to be a low work function compound whereas $BaWO_4$ presents a high work function according also to what measured by Huges [49].

These two compounds have been found by Sarver-Verhey [22], [23] in his surface inspection of the 28,000 hour test cathode (Figure 4). In particular Ba_3WO_6 has been found in the zone that the author believes to be the active zone of the cathode whereas $BaWO_4$ and tungsten have been found respectively upstream and downstream of it.

Sarver-Verhey [22], [23] uses these data to explain the death of the cathode saying that the deposition of these poisonous compounds on the upstream of the insert and on the active zone prevented the work function lowering process avoiding the ignition of the cathode.

Conversely, assuming that the data in [19] are right, the fact that Ba_3WO_6 has been found in the active zone can be seen as a confirmation of its low work function capabilities while the end of life of the cathode can be explained noting that only a small fraction of the insert is still covered with low work function compounds (since most of it is covered by $BaWO_4$ and W that are high work function materials) hence not lowering enough the overall cathode work function and that probably the barium oxide depletion of the insert has got to the point where the BaO production is too low to create enough the low work function compounds on the surface to permit the ignition of the cathode.

It must also be noted how in most of the surface coverage model in the literature [11]-[14], [15] the effect of ion bombardment on the surface coverage seems to be neglected since the desorption characteristic time is never considered to be a function of the plasma parameters.

Since the voltage drop across the sheath is about 10 eV [3], [4] the energy of the impacting ions will be of the same order of magnitude. This value is extremely high if compared to the energies commonly reported for Ba desorption (3-4 eV) [17] meaning that atomic barium will be desorpted very quickly.

The desorption energy of Ba_3WO_6 is instead much higher [21] and, assuming its work function is the one reported in [19], this can explain how low work function compounds can resist on the insert surface given such a high energy of the bombarding ions.

From all what has been said above the data in Ref [19] will be assumed to be correct and hence Ba_3WO_6 will be considered to be the compound responsible for lowering the insert work function.

To understand how this compound is formed and its resistance to temperature we will refer to the phase diagrams presented in Figure 23 - Figure 26 assuming that they will still be valid on the surface (or that they will be at least qualitatively valid).

In these diagrams all the possible combination of tungsten, oxygen, tungsten oxide, barium oxide and calcium oxide are presented.

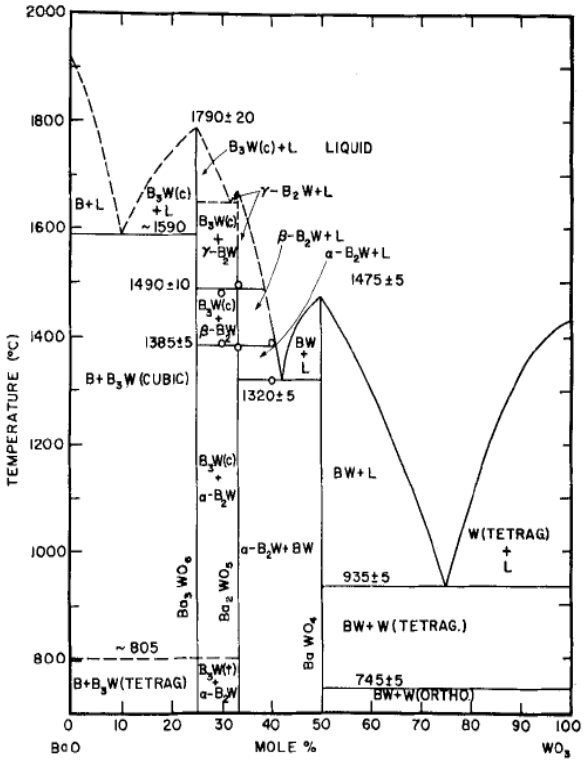

Figure 23 - Phase diagram BaO-WO_3[31]

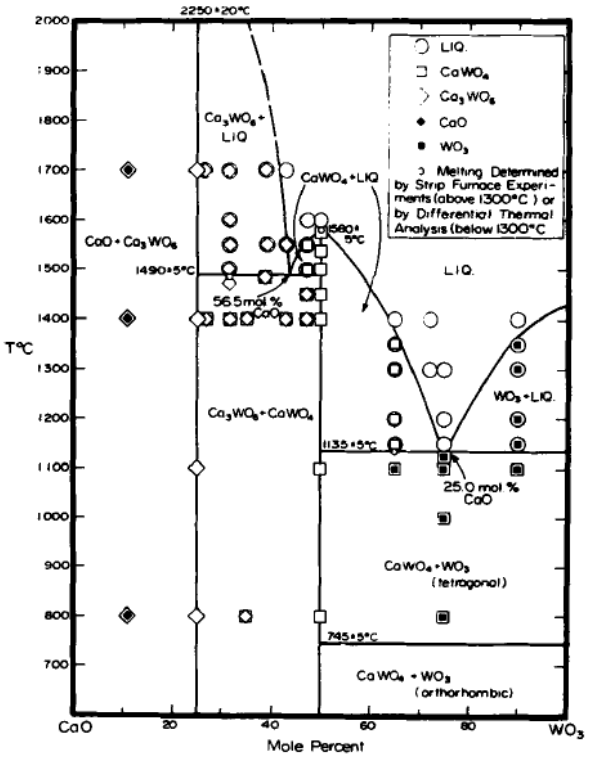

Figure 24 - Phase diagram CaO- WO_3[29]

Looking at Figure 23 we can see how Ba_3WO_6 is present in the BaO – WO_3 system from a concentration of barium oxide of 66.6% up to 100% and in the range of temperatures going from 800 °C up to 1600 °C. Over this temperature Ba_3WO_6 starts to melt.

From this we could assume that this compound is stable up to 1600 °C. Conversely in Ref [21] it has been found that Ba_3WO_6 at high temperatures tends to decompose to $BaWO_4$ and then this dissociates to WO_3 and gaseous BaO at about 1500 °C.

Both the maximum temperature derived from Figure 23 and that relative to Ba_3WO_6 decomposition found in Ref [21] are far above the normal working temperatures of a cathode, we should then expect Ba_3WO_6 to be stable during normal cathode operation.

The reaction involving Ba_3WO_6 and $BaWO_4$ formation and decomposition are reported below [20], [21].

Table 5 - Low work function compounds reactions

Reaction	ΔH eV	ΔS kJ/mol
$Ba_3WO_{6(s)} \iff 2BaO_{(g)} + BaWO_{3(s)}$	11.39	320.11
$BaWO_{4(s)} \iff BaO_{(g)} + WO_{3(s)}$	12.34	137.98

The pressure of the gaseous barium oxide phase involved in these reactions is directly proportional to the Ba_3WO_6 and $BaWO_4$ formation and decomposition rates.

This pressure (in atmospheres) can be expressed as:

$$p_{BaO} = e^{\left(-\frac{\Delta H}{k_b T}+\frac{\Delta S}{R}\right)\frac{1}{\xi_{BaO}}} \tag{68}$$

where ξ_{BaO} represents the stoichiometric coefficient of BaO in the reactions.

Looking at Figure 23, Figure 24 a strong similarity between the two phase diagrams can be found. Barium oxide and calcium oxide, in presence of WO_3, tend to form exactly the same kind of compounds.

This can be justified noting that both Ca and Ba belong to the same element group (ground alkali metals) hence presenting close similarities in their atomic structure.

The only difference between the compounds formed by calcium oxide and barium oxide is that the compounds formed by the Ca have a much higher resistance to temperature than those formed by Ba. In fact in Ref [29] Ca_3WO_6 is reported to melt at a temperature close to 2200 °C hence 700 degrees higher than the one relative to Ba_3WO_6.

Looking at Figure 25, Figure 26 it is possible to see how solid solution between BaO and CaO compounds can occur with partial substitution of barium oxide with calcium oxide. In particular it can be noted how solid solution mainly occur with X_3WO_6 and XWO_4 where X can be either calcium or barium.

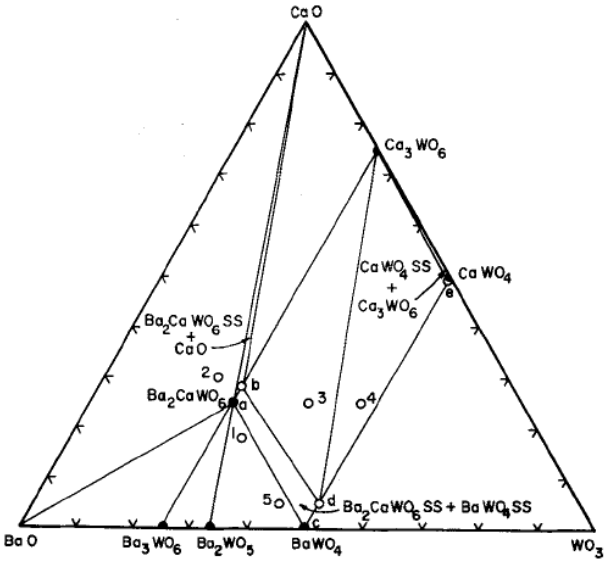

Figure 25 - Phase diagram BaO-CaO-WO_3 section at 1200 °C [29]

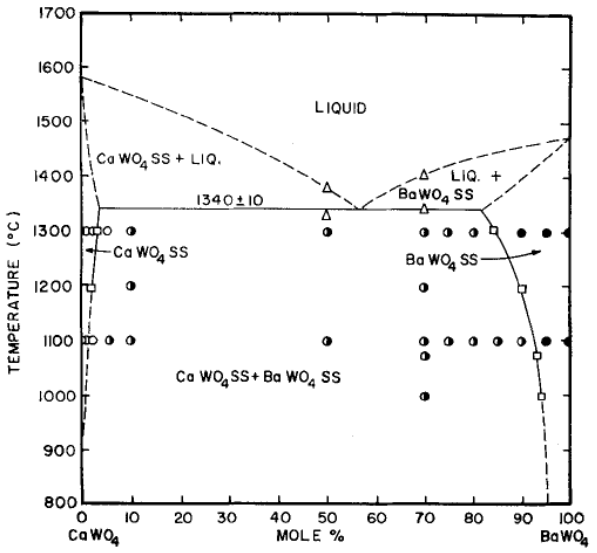

Figure 26 - $BaWO_4$ – $CaWO_4$ phase diagram [19]

A literature search has been performed to find the work functions of the calcium-tungsten compounds but unfortunately no data has been found.

Considering that the work function of calcium is close to the one of barium ($\phi_{Ca} = 2.9\,eV$, $\phi_{Ba} = 2.5\,eV$) and considering the similarities in atomic structure between these two elements it can be assumed that the work functions of the solid solutions $Ba_{3-x}Ca_xWO_6$ and $Ba_{1-x}Ca_xWO_4$ will not be sensibly different from the ones relative to Ba_3WO_6 and $BaWO_4$ reported in Table 4.

From these observations a justification of the presence of CaO inside the impregnate can be formulated.

Barium oxide is a low work function compound that evaporates at relatively low temperatures, once evaporated it deposits on the surface of the emitter reacting with tungsten and creating low work function compounds (Ba_3WO_6).

Calcium oxide is still a low work compound but with a higher resistance to temperatures than barium oxide hence with lower evaporation rates.

Therefore a partial substitution of barium oxide with calcium oxide in Ba_3WO_6 will increase the temperature resistance of this compound without sensibly raising the value of its work function generating a high temperature resistant low work function compound.

It can then be hypothesized that the main function of CaO inside the impregnate is, substituting part of the BaO, to increase the temperature resistance of the low work function compounds.

It could be now objected that, since CaO seems to have the same good emission characteristics as BaO and is able to bond with tungsten to create compounds that are more resistant to temperature than the one based on BaO, the insert impregnant could be based only on calcium oxide without the need of barium oxide.

Since CaO has a higher resistance to temperature than BaO, given an insert temperature the CaO evaporation rate from the insert impregnant will be much lower than the one of barium oxide. This means that to sustain the supply of calcium oxide from the insert needed to form low work function compounds the insert temperature should be higher than with BaO based impregnants.

To maintain and higher insert temperature the power input from the cathode plasma must increase hence either the plasma density or the plasma voltage will increase raising the total power required to run the cathode.

Considering what has been said above the usual 4:1 ratio between BaO and CaO can be qualitatively explained.

Using the ternary diagram reported in Figure 25 from the knowledge of the relative concentration of BaO, CaO and WO_3 the exact surface composition could be derived. Unfortunately this diagram is not complete since we do not know which compounds are present in each area of the diagram and no more detailed quantitative information has been found in the literature.

4.2 Low work function compounds deposition rates

Deposition of barium oxide on the emitter surface is the result of the reactions reported in Table 5 when these proceed from right to left hence when one BaO molecule in the gaseous form reacting with the surface forms a low work function compound molecule.

To predict the exact behaviour of deposition with time the forward and backward reactions constants are needed. Unfortunately these data have not been found in the literature; the only data available are relative to the equilibrium constant of the reactions.

The rates of change of Ba_3WO_6 and $BaWO_4$ can be expressed as a function of the reacting species composition as

$$[\dot{BaWO_4}] = kb\,[BaO][WO_3] - kf\,[BaWO_4] \tag{69}$$

$$[\dot{Ba_3WO_6}] = kb\,[BaO]^2[BaWO_4] - kf\,[Ba_3WO_6] \tag{70}$$

By definition [51] the equilibrium constant is defined as

$$K_p = \frac{kf}{kb} = e^{-\frac{\Delta H}{k_b T} + \frac{\Delta S}{R}} \tag{71}$$

If the equilibrium constant is much smaller than one ($K_p \ll 1$) the forward constant will be much smaller than the backward one ($kf \ll kb$) hence the rate of production of Ba_3WO_6 and $BaWO_4$ will be at their maximum quickly moving the reactions toward a left shifted equilibrium where all the barium oxide and tungsten trioxide have reacted to form low work function compounds.

Conversely if the equilibrium reaction constants are much bigger than one the reactions will be quickly pushed towards a right shifted equilibrium where all the compounds are dissociated into BaO and WO_3.

The values of the K_p calculated using Eq. (71) and the data in Table 5 from Ref. [20] and [21] are reported in Table 6

Table 6 - Reactions equilibrium constant at 1100 °C

Reaction	K_p	
$Ba_3WO_{6(s)} \iff 2BaO_{(g)} + BaWO_{3(s)}$	$8.91 \cdot 10^{-26}$	$kf \ll kb$
$BaWO_{4(s)} \iff BaO_{(g)} + WO_{3(s)}$	$8.95 \cdot 10^{-39}$	$kf \ll kb$

As can be seen in Table 6 the equilibrium constant of these two reactions are very small meaning that the reactions are completely shifted to the left.

As said before this means that barium oxide react with tungsten very easily and quickly to form $BaWO_4$ and then Ba_3WO_6.

Based on this we can formulate the hypothesis that all the barium oxide arriving at the surface deposits on it creating firstly $BaWO_4$ and then Ba_3WO_6.

Using this assumption the low work function compounds deposition rates can be expressed as

$$\dot{N}^+_{BaWO_4} = \theta_W \left(1 - \Pi\right) \frac{\dot{m}_{BaO}}{m_{BaO}} \tag{72}$$

$$\dot{N}^+_{Ba_3WO_6} = \frac{1}{2}\theta_{BaWO_4} \left(1 - \Pi\right) \frac{\dot{m}_{BaO}}{m_{BaO}} \tag{73}$$

Where $\dot{m}_{BaO}$ is the mass flow rate of BaO arriving to the surface of the insert and Π is the porosity of the insert.

The term $(1-\Pi)$ takes into account the fact that these low work function compounds can be formed only on the tungsten surface of the insert and not on the pores (since the pores are filled with the impregnant) whereas the terms θ_W and θ_{BaWO_4} take into account respectively the fact that $BaWO_4$ is formed starting form tungsten and that Ba_3WO_6 is formed starting from $BaWO_4$

4.3 Thermal desorption of low work function compounds

Thermal desorption of low work function compounds is the result of the reactions reported in Table 5 when these proceed from left to right hence when a low work function compound molecule dissociates releasing a molecule of BaO in the gaseous form. As shown before the equilibrium constant of these reactions is much smaller than unity meaning that these are completely shifted to the left hence very small desorption rates must be expected.

Using Knudsen-Hertz-Langmuir formula Eq. (41) the desorption rates can be calculated from the vapour pressure of the low work function compounds.

Hence the thermal desorption rates in molecules per unit area per unit time are

$$\dot{N}^{-th}_{Ba_3WO_6} = \frac{1}{2}\theta_{Ba_3WO_6}(1-\Pi)\frac{e^{\left(-\frac{\Delta H}{kT}+\frac{\Delta S}{R}\right)\frac{1}{2}}}{m_{BaO}}\frac{10^5}{\sqrt{\frac{2\pi RT}{M_{BaO}}}} \tag{74}$$

$$\dot{N}^{-th}_{BaWO_4} = \theta_{BaWO_4}(1-\Pi)\frac{e^{\left(-\frac{\Delta H}{kT}+\frac{\Delta S}{R}\right)}}{m_{BaO}}\frac{10^5}{\sqrt{\frac{2\pi RT}{M_{BaO}}}} \tag{75}$$

where the term $1-\Pi$ takes into account the fact that deposition can will occur only on the tungsten part of the insert and not on the pores.

A comparison between these two desorption rates is presented in Table 7

Table 7 - Ba_3WO_6 and $BaWO_4$ thermal desorption rates at different temperatures

Compound	T = 900 °C	T = 1000 °C	T = 1100 °C	T = 1200 °C
Ba_3WO_6	$2.69\cdot10^{10}$	$2.14\cdot10^{12}$	$9\cdot10^{13}$	$2.27\cdot10^{15}$
$BaWO_4$	$9.71\cdot10^{-20}$	$1.35\cdot10^{-15}$	$4.67\cdot10^{-12}$	$5.32\cdot10^{-9}$

These desorption rates can be converted from molecules per unit area per unit time to kilograms per unit area per unit time by multiplying them by the molecular weight (in kilograms) of Ba_3WO_6 and $BaWO_4$. From this we obtain that a desorption rate of 10^{14} molecules per meter squared per second for Ba_3WO_6 is roughly equivalent to 10^{-11} Kg/(m^2s) and comparing the values in Table 7 to the ones in Figure 17 it can be seen how small these desorption rates are.

It can be also noted how the $BaWO_4$ desorption rates are extremely small with values that, if expressed in kilograms per meter squared per second, vary from 10^{-45} to 10^{-34}.

4.4 Ion sputtering desorption

As already said before (§4) there are two main low work function compounds desorption mechanisms: thermal desorption and ion sputtering caused by the hollow cathode plasma.

Thermal desoprtion has been analyzed and quantified in the section above; now the ion sputtering process will be studied.

Assuming to have a plasma of ion density n_i and assuming that the ion flux to the insert is determined by the thermal motion of the ions the low work function desorption rate can be written as

$$\dot{N}^{-bomb} = n_i v_{th} (1 - \Pi) \theta Y_{sputt} \tag{76}$$

Where v_{th} is the sputtered particle thermal velocity that can be expressed as

$$v_{th} = \sqrt{\frac{kT}{2\pi m}} \tag{77}$$

and Y_{sputt} is the sputtering yield of Ba_3WO_6 or $BaWO_4$.

A literature search has been carried out to find data relative to the sputtering yield of the work function compounds but no data have been found.

The theories that are commonly used to calculate the sputtering yield are based on data that are currently unknown for these compounds like surface binding energy and collision cross sections.

It has then be decided to calculate the sputtering using the theory developed by Langmuir[45].

In this theory the sputtering process is explained as follows: *"...an ion striking on the cathode surface will drive the cathode atom it strikes into the surface creating a local*

depression…" the ion is then reflected and after the reflection *"the ion may have enough momentum to knock off a cathode atom around the edge of the depression"* [45]. The sputtering process is then the results of two collisions.

Assuming that the first collision can be approximated as the one between a free ion and a free atom and neglecting the velocity of the atom before the collision the conservation of momentum and energy can be written as [45]

$$m_c v_{c2} = m_g \left(v_{g1} - v_{g2}\right) \tag{78}$$

$$\frac{1}{2} m_c v_{c2}^2 = \frac{1}{2} m_g \left(v_{g1}^2 - v_{g2}^2\right) \tag{79}$$

Where the subscripts *c* and *g* indicates quantities relative respectively to the cathode atom and to the ion and where the subscripts *1* and *2* refers to quantities before and after the first collision.

Combining Eq. (78) and (79) the velocity of the ion after this collision can be derived as a function of the impacting velocity.

$$v_{g2} = v_{g1} \frac{m_g - m_c}{m_g + m_c} \tag{80}$$

After the first collision the ion gets reflected and impacts on another surface atom. Treating this collision as the one before and indicating with *2* and *3* the quantities before and after this collision the conservation of momentum and energy are

$$m_c v_{c3} = m_g \left(v_{g2} - v_{g3}\right) \tag{81}$$

$$\frac{1}{2} m_c v_{c3}^2 = \frac{1}{2} m_g \left(v_{g2}^2 - v_{g3}^2\right) \tag{82}$$

Combining Eq. (81), (82) and (80) the velocity of the cathode atom after the second collision can be derived as a function of the velocity of the ion before the first collision.

$$v_{c3} = 2 v_{g1} m_g \frac{m_g - m_c}{(m_g + m_c)^2} \tag{83}$$

From this the energy transferred to the cathode atom during the second collision is

$$E_{trans} = \frac{1}{2} m_c v_{c3}^2 = 2 m_c v_{g1}^2 m_g^2 \frac{(m_g - m_c)^2}{(m_g + m_c)^2} \tag{84}$$

Noting that $1/2\, m_c v_{g1}^2$ is the initial kinetic energy of the impacting ion, the transferred energy can be expressed as

$$E_{trans} = \alpha E_0 \tag{85}$$

where α is a coefficient defined as follows [45]

$$\alpha = 4m_c m_g \left[\frac{m_g - m_c}{(m_g + m_c)^2}\right]^2 \tag{86}$$

Once we know the energy transferred from the ion to the cathode surface the probability that a cathode atom is sputtered is related to the ratio between the activation energy needed for the cathode atom evaporation process and the energy transferred by the impacting ions.

If the energy of the impacting ions is of the order of some electronvolts the sputtering yield will most probably be smaller than unity hence we can express Y_{sputt} as [45]

$$Y_{sputt} = e^{-\frac{E_{act}}{E_{trans}}} = e^{-\frac{E_{act}}{\alpha E_0}} \tag{87}$$

The activation energies of the decomposition processes relative to Ba_3WO_6 and $BaWO_4$ are unknown.

By definition the activation energy is the minimum energy necessary for a specific reaction to occur [51]. The activation energy is the energy needed to bring the reactants from their "quiet" state to the "transition state".

The transition state is, along a reaction coordinate, *the point of maximum free energy, where bond-making and bond-breaking are balanced* [52]. From this state the atomic bonds can rearrange to form the reaction products or can go back to the form the reaction reactants.

In both cases in the bond-making process to form either the reaction products or the reactants some energy will be released. The difference between the free energy spent to get to the "transition state" and the free energy released in the formation of the reaction products is the free Gibbs energy of the reaction [51].

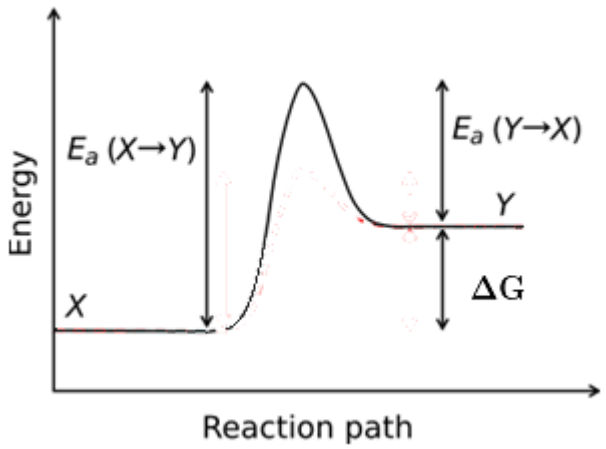

Figure 27 – Energy pattern in the reaction $X \rightarrow Y$

From what said above the hypothesis of assuming the activation energies of the reaction involving the decomposition of Ba_3WO_6 and $BaWO_4$ equal to the correspondents free Gibbs energies calculated with the data reported in Table 5

$$E_{act} = \Delta G = \Delta H - T\Delta S \tag{88}$$

will produce higher values of the sputtering yield and consequently of the desorption rates therefore giving a conservative estimate of the low work function surface coverage evolution.

In Eq. (88) the values of *ΔH*, *ΔS* and *ΔG* are expressed in J/mol hence the value of *ΔH* in Table 5 must be converted from eV to this unit of measurement.

Considering that the initial energy of the impacting ion is equal to the voltage drop in the sheath it will be handy to express the activation energy in eV.

Rewriting Eq. (88) so that the values in Table 5 can be used without any conversion we have

$$E_{act} = \Delta G = \Delta H - \frac{k_b}{qR} T\Delta S \tag{89}$$

So substituting Eq. (87) and (88) into Eq. (76) and assuming that the voltage drop is much higher than the ion temperature expressed in eV (so that the latter can be neglected) we get the final expression of the ion sputtering desorption rate

$$\dot{N}^{-bomb} = n_i v_{th} (1 - \Pi)\, \theta\, e^{\frac{-E_{act}}{\alpha \Delta V_{sheat}}} \tag{90}$$

As already done for the thermal desorption rate we can compare the sputtering ones for Ba_3WO_6 and $BaWO_4$. The results are reported in Table 8

Table 8 - Ba_3WO_6 and $BaWO_4$ sputtering desorption rates at different temperatures

n_i	ΔV_{sheath}	Π	4.4.1 θ
10^{20}	5 V	80%	1
Compound	T = 1000 °C	T = 1100 °C	T = 1200 °C
Ba_3WO_6	$7.21 \cdot 10^{19}$	$9.7 \cdot 10^{19}$	$1.32 \cdot 10^{20}$
$BaWO_4$	$2.32 \cdot 10^{17}$	$2.82 \cdot 10^{17}$	$3.42 \cdot 10^{17}$

As we can see also in this case the desorption rates relative to $BaWO_4$ are much smaller than the one relative Ba_3WO_6.

Comparing the desorption rates reported in Table 8 with those in Table 7 it can be noted how the sputtering desorption rates are several order of magnitude higher than the thermal ones.

The sputtering desorption rates if converted in $Kg/(m^2s)$ are of the same order of magnitude as the barium oxide evaporation rates from the insert. This means that for the conditions reported in Table 8 the ratio at which low work function compounds are desorpted is close the one at which new compounds are formed resulting in a surface coverage that is more or less stable in time. If the voltage drop or the ion density increase or if the evaporation rate decreases the desorption rate will become much higher than the deposition one resulting in the depletion of low work function compounds from the surface; on the contrary a decrease in ΔV_{sheath} or n_i or an increase in the evaporation rate of BaO will result in accumulation of low work function compounds.

4.5 Low work function surface coverage model

Once the deposition and desorption rates have been quantified and analyzed the surface coverage of low work function compounds can be derived.

In the real functioning of a cathode only a part of the barium oxide produced by evaporation of the impregnant will react with the surface of the insert to form low work function compounds whereas the rest will be "lost" inside the hollow cathode plasma; moreover the barium oxide produced by the decomposition of the low work function compounds will not completely get "lost" inside the hollow cathode plasma but part of it will react again with the surface to form new low work function compounds.

Furthermore the barium oxide "lost" inside the plasma, due to collision with electrons, will be firstly divided in barium and oxygen atoms and subsequently ionized. Part of these ionized atoms will, due to their thermal motion, get close to the insert surface enough to be attracted to it because of the voltage sheath. Part of the barium and oxygen atoms so attracted to the surface will stick on it reacting with the tungsten and creating new low work function compounds.

From this we can see how also the barium oxide that before has been considered "lost" inside the plasma will be partially recovered.

This situation is made more complicated by the fact that, due to the thermal gradient along the insert, the level of BaO depletion will vary in different location of the insert increasing from the upstream region (where the temperature is lower) to the downstream one (where the temperature is higher).

Since the barium oxide depletion inside the insert is a function of time and since the evaporation rate is a strongly non linear function of the BaO insert content (see §3.2) this variation in barium oxide content and temperature along the insert will produce evaporation rates, and hence BaO gaseous concentration, that will vary strongly from one location of the insert to another and that will be function of time.

This concentration non-uniformity will give raise to a time and space dependent diffusion motion of the evaporated barium oxide from areas where its concentration is higher to areas where its concentration is lower.

Since this diffusion motion takes place just above the insert surface it will be most probably influenced by the processes happening inside the plasma sheath.

The diffusion coefficient governing this motion will be then likely a function of the local sheath voltage drop and ion and electron temperatures and densities.

As it can be noticed in this brief explanation the processes taking place in the gaseous phase above the insert surface are complex and influenced by the characteristics of the surrounding plasma.

To model them properly a chemical plasma model able to take into account barium, barium oxide, oxygen and the working gas of the cathode would be needed. This model should also take into account the chemical reaction involving Ba, O, BaO and the low work function compounds and should be able to model the sheath processes in high detail.

To solve this problem a semi-empirical or an empirical approach can not be used since in the literature there are no direct measurements relative to barium and barium oxide return from the plasma to the insert surface and no measurements that can be used to derive it.

Hence to avoid the extremely high level of complexity related to the development of a chemical plasma model some simplifying assumptions will be made and their global effect will be analyzed.

The first set of assumptions will be that all the barium oxide produced by the impregnant evaporation will take part in the surface reaction, that all the barium oxide produced by low work function decomposition will be definitely “lost” inside the plasma and that no barium or barium oxide will be come back to the insert surface from the plasma.

These assumptions, neglecting the possibility of recovering some of the barium produced by compounds desorption, will globally produce an underestimation of the Ba and BaO rates to the surface hence resulting in an underestimation of the low work function compounds formation rate.

The second assumption consists in neglecting the diffusive motion of gaseous BaO along the insert surface.

Doing this we will consider that all the barium oxide evaporated from the impregnant in a pore will eventually react only with the part of insert surface close to that pore hence gaseous BaO will not migrate along the insert to react in a location of the insert that is further upstream or downstream of the one it evaporated from.

After some thousands of hours of functioning of a hollow cathode, since the insert temperature is higher in the downstream end of the cathode than in upstream one, the BaO content in the downstream area will be lower than in the upstream one. Because of this difference in BaO content the barium oxide evaporation rate from the insert will be

much higher upstream than downstream due to the nonlinear relation between evaporation and local BaO content (Figure 17). It must be also noted that due to the fact that the insert temperature, plasma ion density and sheath voltage drop in the downstream region are normally higher than in the upstream one, the low work function compounds desorption rates will be much higher downstream than upstream.

In the real functioning of a cathode due to the gaseous BaO diffusive motion some of the barium oxide produced upstream will be transported downstream and there will react with the surface creating low work function compound helping to contrast the high depletion rates and to maintain a higher value of low work function surface coverage.

Neglecting this gaseous BaO diffusion transport will result in an underestimation of the surface coverage in the downstream region of the cathode.

Since both the assumptions made result in an underestimation of the low-work-function-coverage of the insert surface they will produce higher values of the insert work function and so worse performances of the cathode ultimately producing a conservative estimate of the hollow cathode lifetime.

4.5.1 Model development and analytical solution

Assuming that for a full coverage every tungsten atom that was originally on the surface is bonded with barium and oxygen to form Ba_3WO_6 and that the desorption process of Ba_3WO_6 will produce $BaWO_4$ together with gaseous BaO whereas the creation of Ba_3WO_6 needs a gaseous BaO and a $BaWO_4$ molecule, the rate of change of the surface coverage can be expressed as

$$\dot{\theta}_{BaWO_4} = \frac{m_{BaO}}{\sigma_{BaO}} \left[\dot{N}^{+}_{BaWO_4} + \left(\dot{N}^{-th}_{Ba_3WO_6} + \dot{N}^{-bomb}_{Ba_3WO_6} - \dot{N}^{+}_{Ba_3WO_6} \right) - \left(\dot{N}^{-th}_{BaWO_4} + \dot{N}^{-bomb}_{BaWO_4} \right) \right] \tag{91}$$

$$\dot{\theta}_{Ba_3WO_6} = \frac{m_{BaO}}{\sigma_{BaO}} \left[\dot{N}^{+}_{Ba_3WO_6} - \left(\dot{N}^{-th}_{Ba_3WO_6} + \dot{N}^{-bomb}_{Ba_3WO_6} \right) \right] \tag{92}$$

where m_{BaO} and σ_{BaO} are the atomic mass and the surface density of barium oxide.

Using Eq. (90),(72) – (75) and noting that the portion of the surface covered in tungsten θ_W can be expressed as

$$\theta_W = 1 - \theta_{BaWO_4} - \theta_{Ba_3WO_6} \tag{93}$$

The system of differential equation consisting of Eq. (91) and (92) can be rewritten as

$$\begin{bmatrix} \dot{\theta}_{Ba_3WO_6} \\ \dot{\theta}_{BaWO_4} \end{bmatrix} = \begin{bmatrix} F_{11} & F_{12} \\ F_{21} & F_{22} \end{bmatrix} \begin{bmatrix} \theta_{Ba_3WO_6} \\ \theta_{BaWO_4} \end{bmatrix} + \begin{bmatrix} U_1 \\ U_2 \end{bmatrix} \tag{94}$$

where

$$F_{11} = -\frac{m_{BaO}}{\sigma_{BaO}} \left[(1-\Pi) \frac{e^{\left(-\frac{\Delta H}{kT}+\frac{\Delta S}{R}\right)}}{m_{BaO}} \frac{10^5}{\sqrt{\frac{2\pi RT}{M_{BaO}}}} + n_i v_{th} (1-\Pi) \theta \, e^{\frac{-E_{act}}{\alpha \Delta V_{sheat}}} \right] \Bigg|_{Ba_3WO_6} \tag{95}$$

$$F_{12} = \frac{1}{2} (1-\Pi) \frac{\dot{m}_{BaO}}{\sigma_{BaO}} \tag{96}$$

$$F_{21} = \frac{m_{BaO}}{\sigma_{BaO}} \left[(1-\Pi) \frac{e^{\left(-\frac{\Delta H}{kT}+\frac{\Delta S}{R}\right)}}{m_{BaO}} \frac{10^5}{\sqrt{\frac{2\pi RT}{M_{BaO}}}} + n_i v_{th} (1-\Pi) \theta \, e^{\frac{-E_{act}}{\alpha \Delta V_{sheat}}} \right] \Bigg|_{Ba_3WO_6} \tag{97}$$

$$F_{22} = -\frac{m_{BaO}}{\sigma_{BaO}} \left[(1-\Pi) \frac{e^{\left(-\frac{\Delta H}{kT}+\frac{\Delta S}{R}\right)}}{m_{BaO}} \frac{10^5}{\sqrt{\frac{2\pi RT}{M_{BaO}}}} + n_i v_{th} (1-\Pi) \theta \, e^{\frac{-E_{act}}{\alpha \Delta V_{sheat}}} \right] \Bigg|_{BaWO_4} - \\ -\frac{1}{2} (1-\Pi) \frac{\dot{m}_{BaO}}{\sigma_{BaO}} \tag{98}$$

$$U_1 = 0 \qquad\qquad U_2 = (1-\Pi) \frac{\dot{m}_{BaO}}{\sigma_{BaO}} \tag{99}$$

A differential equation of the form

$$\dot{\Theta} = F(t)\Theta + U(t) \tag{100}$$

where Θ and U are time dependent vectors and F is a time dependent matrix can be solved analytically (appendix C). The general solution is

$$\Theta(t) = e_M^{\int_0^t F(t)dt} \left(\Theta(0) + \int_0^t U(t) e_M^{-\int_0^\tau F(\tau)d\tau} dt \right) \tag{101}$$

where the e_M is used to indicate the matrix exponential operator to avoid confusion with the scalar exponential.

The values of $\theta_{Ba_3WO_6}$ and θ_{BaWO_4} so found are relative to the low work function coverage of the tungsten surface of the insert, we must consider that also the barium oxide present in the pores will contribute in lowering the average work function.

The coverage relative to the barium oxide inside the pores is

$$\theta_{BaO} = \Pi \rho_{BaO}(t) \tag{102}$$

Where ρ_{BaO} is the relative concentration of barium oxide inside the pores calculated through the model presented in §3.5.

4.5.2 Overall work function calculation

Given a metal surface of low work function ϕ_m and given a coverage θ of this surface with a compound of work function ϕ_c the overall work function of the surface $\bar{\phi}$ can be calculated using the formula proposed by Longo[14]

$$\bar{\phi} = \phi_m \left(\frac{\Gamma\phi_m}{\phi_c}\right)^{\frac{\Gamma\theta}{1-\Gamma}} + \phi_c \left[1 - \left(\frac{\Gamma\phi_m}{\phi_c}\right)^{\frac{\theta}{1-\Gamma}}\right] \tag{103}$$

where Γ is a coefficient determined by finding the zero of the first derivative of Eq. (103) given the minimum value of the overall work function[14].

$$\begin{gathered} \left.\frac{d\bar{\phi}}{d\Gamma}\right|_{\theta=1} = 0 \\ \bar{\phi}\left(\Gamma, \theta = 1\right) = \phi_{min} \end{gathered} \tag{104}$$

According to what derived above we have that the tungsten surface of an insert is covered partially with $BaWO_4$ and partially Ba_3WO_6, to this that part of the pores surface that is partially covered with BaO must be added.

To calculate the overall work function of such a surface some assumptions will be made.

Firstly we will assume that the work function relative to the BaO contained inside the pores is the same as the one relative to Ba_3WO_6.

Doing this we can define a coverage that takes into account both the Ba_3WO_6 and the pores as

$$\theta_1 = \theta_{Ba_3WO_6} + \theta_{BaO} \tag{105}$$

whose work function is

$$\phi_1 = \phi_{Ba_3WO_6} = 1.33 + 6.09 \cdot 10^{-4} T \tag{106}$$

We will then assume that the low work function relative to the tungsten surface plus the $BaWO_4$ coverage can be calculated as

$$\phi_2 = \frac{\phi_{BaWO_4}\theta_{BaWO_4} + \phi_W\theta_W}{\theta_{BaWO_4} + \theta_W} \tag{107}$$

And that ϕ_2 is relative to the coverage

$$\theta_2 = \theta_{BaWO_4} + \theta_W \tag{108}$$

From Eq. (93) we have

$$\theta_1 + \theta_2 = 1 \tag{109}$$

Thanks to these assumptions we have reduced the original problem to that of the coverage of a high work function surface (that is made up of tungsten and $BaWO_4$) with low work function compound (meaning both the BaO contained inside the pores and Ba_3WO_6). This low work function compound has a work function equal to ϕ_1 and covers a portion of the surface equal to θ_1. The uncovered portion of the high work function surface is equal to θ_2 and has a work function ϕ_2.

Hence imposing in Eq. (103) and (104) that $\theta = \theta_1$ and $\phi_m = \phi_2$, and that the work function lowering compounds is barium ($\phi_c = \phi_{Ba} = 2.55\, eV$), and that the minimum work function relative to a monolayer coverage is the one relative to Ba_3WO_6 ($\phi_{min} = \phi_1$) the overall work function of the surface can be calculated.

This value of the work function is then lowered thanks to the Schottky effect generated by the presence of an electric field on the emitting surface.

As already said in §1.3 the Schottky effect can be quantified as

$$\Delta\phi = \sqrt{\frac{q\,|E|}{4\pi\epsilon_0}} \tag{110}$$

Where E is the value of the electric field at the surface and will be calculated using the formula derived by Siegfried and Wilbur [32].

Hence the effective work function will be equal to

$$\phi_{eff} = \bar{\phi} - \Delta\phi = \bar{\phi} - \sqrt{\frac{q}{4\pi\epsilon_0}\left(\frac{n_e k_b T_e}{\epsilon_0}\right)^{1/2}\left[2\left(1 + 2\frac{q\Delta V}{k_b T_e}\right)^{1/2} - 4\right]^{1/2}} \tag{111}$$

From the knowledge of the evolution of the effective work function and of the barium oxide content inside the insert an end-of-life criterion can be derived.

The derivation of the end-of-life criterion will be done later in §5.4.1.1 based on the emitted current and surface coverage trends computed relatively to the hollow cathode used by T. R. Sarver-Verhey in Ref. [22], [23].

4.5.3 Plasma parameter update

As it can be seen in the sections above the knowledge of the hollow cathode plasma parameters and of the insert temperatures are essential to estimate the desorption rates and hence the surface coverage of low work function compounds.

To do so the ideal solution will be to have a plasma model that starting from inputs like total cathode current, mass flow rate and cathode dimension will be able to calculate the ion and electron temperature and density profiles along the insert length together with the voltage fall and insert temperature profile.

The only model that at present is able to fit these requirements is the plasma model developed at JPL [5], [6], [35], [36];

Since is impossible to gain access to this code and since replicating it starting from the published material will take a very long time adding no novelty to the work presented in this thesis an alternative way to obtain such plasma parameters will be developed.

The possibility of modifying the model developed by Salhi and Turchi [7] to include the dependency of densities, temperatures and voltage fall from the cathode abscissa has been taken into account but no results have been obtained.

Considering what said above and considering that the final aim of the work presented in this thesis is not the development of a plasma model but the development of a model able to predict the hollow cathode lifetime, the plasma parameters will be obtained through a semi-empirical approach.

We will assume that, given a hollow cathode to simulate with the model described above, the plasma parameters at the beginning of life are known by measurements.

The only plasma parameter that is not measured at all is the ion temperature. To estimate this we will refer to the numerical data obtained by Salhi and Turchi [7] and by Mikellides [36].

Looking at these data it can be noted how the trend of the ion temperature (T_i) and of the insert temperature (T_w) are quite close, with T_i being very close to T_w upstream the cathode whereas downstream T_i is higher than T_w with a maximum value of twice the insert temperature.

Considering that no experimental data exist relatively to the ion temperature and that, to be exact, what we need is the square root of the ion temperature since it will be only used to calculate the ion flux as in Eq. (10) we will make the simplifying assumption that the ion temperature is always equal to the insert temperature.

Considering that the sheath thickness is orders of magnitude smaller than the cathode radius (this thickness is about 10^{-5} m whereas the cathode radius is of the order of a millimetre) and considering that if the ion density were sensibly different from the electron one, very intense electric fields would arise and that such electric fields have never been detected we will also assume the ion density to be equal to the electron density (quasi-neutrality $n_i = n_e = n$) everywhere except the sheath region.

To simplify the problem we will assume that the dependency of the plasma parameters on time and space can be split into two separate functions so that is possible to write

$$\begin{aligned} \Delta V_{sheath}(t,x) &= k_{\Delta V}(t)\ \Delta V_{sheath}(0,x) \\ n(t,x) &= k_n(t)\ n(0,x) \\ T_e(t,x) &= k_{T_e}(t)\ T_e(0,x) \\ T_w(t,x) &= k_{T_w}(t)\ T_w(0,x) \end{aligned} \tag{112}$$

meaning that the plasma parameters values will be shifted up or down by a multiplicative constant.

It could be argued that the ion density profile is linked to the thermionic emission profile hence a change in the surface coverage distribution will affect consequently the particle density trend invalidating the last of the assumptions above.

To judge this a comparison between the plasma electron density profile taken from the experimental data in Ref [36] relative to the NSTAR cathode functioning at 12 A, and the emitted electron density profile relative to the same cathode calculated using the insert temperature reported in [25] is shown below

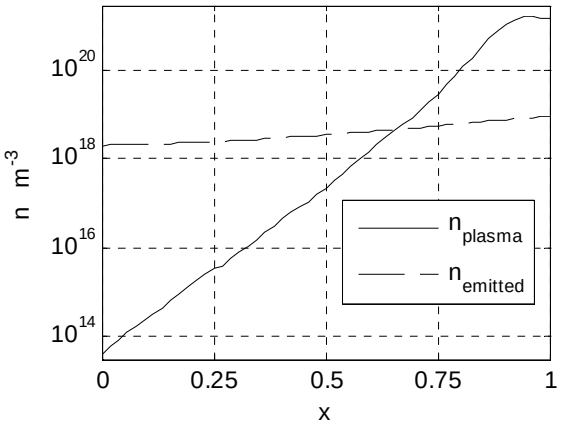

Figure 28 – Comparison between plasma electron density [36] and emitted electron density

where x is the non-dimensional cathode abscissa (along the cathode length) and where the emitted electron density is calculated assuming that the electrons leave the surface with the thermal speed relative to the surface temperature (since the emitted electrons leave the surface will have a temperature equal to the surface one [53])

$$n_{emitted} = \frac{J_{th}}{q}\sqrt{\frac{2\pi m_e}{k_b T_w}} \tag{113}$$

From Figure 28 we can see how the electron plasma density is much higher than the emitted one in the downstream region contrarily to what happen in the upstream one.

From this we can infer that the shape of the plasma density profile downstream is mainly influenced by the processes taking place close to the orifice due to the strong area contraction and to the presence of the orifice. Upstream the plasma profile must definitely be influenced by the emitted electron profile but in this area the depletion rates due to ion bombardment are expected to be less severe than in the downstream region.

Considering all what said above and considering that the most important region is the downstream one we can conclude that the assumption of constant shape of the electron density profile during the cathode life is acceptable.

Once this assumption has been accepted it might extended to the plasma voltage drop and to the electron and wall temperature since all these quantities are strictly interdependent.

We will also assume that the electron temperature will not vary sensibly due to a change in the surface coverage as its value has been shown to have small variations over a wide range of cathode operating conditions [4], §5.3.

From all the assumptions above the update of the plasma parameters has been reduced to the calculation of three time-dependent multiplicative parameters ($k_{\Delta V_{sheath}}$, k_n, k_{T_w}).

To derive these parameters the power balance at the cathode surface and the total emitted current conservation will be imposed

$$\begin{aligned}\int J_{th}\left(\phi_{eff} + \frac{5kT_e}{2q}\right) dA = \int J_e\left(\phi_{eff} + \frac{5kT_w}{2q}\right) dA + \\ + \int J_i\left(E_{ion} + \Delta V_{sheath} - \phi_{eff}\right) dA + f q_r\end{aligned} \tag{13}$$

$$\int \left(J_{th} + J_i - J_e\right) dA = I_D \tag{18}$$

During the simulation of the hollow cathode the plasma parameters will be updated at fixed time steps. The distance between two consecutive time steps will be defined to obtain accurate simulations with reasonable computing times and will be of the order of 10 hours of simulated functioning (meaning that if 10,000 hours of cathode functioning are simulated the plasma parameters will be updated about 1000 times).

At every update Eq. (13), (18) will be solved assuming constant wall temperature deriving the values of $k_{\Delta V_{sheath}}$ and k_n. It might happen that a solution of these equations cannot be found. This means that the insert temperature is too low to provide enough thermionic emission to meet the total current emission requirements set by the power supply. In this case the insert temperature will be increased by 10 °C steps until a solution of Eq. (13) and (18) can be found.

4.6 Low work function compounds deposition and desorption modelling conclusion

In this chapter the compounds lowering the work function of a hollow cathode insert have been studied.

Starting from the data in Ref [19] Ba_3WO_6 has been identified as the main low work function compound. Its deposition and desorption rates have been modelled taking into account both thermal desorption and ion sputtering.

To derive these rates several hypotheses have been formulated due to the high complexity of the problem and to the lack of kinetic chemistry data regarding the formation and decomposition of $BaWO_4$ and Ba_3WO_6.

All the hypotheses made have been justified and all of them have been formulated to produce conservative estimates of the low work function coverage and hence of the hollow cathode lifetime.

A model for the low work function coverage has then been formulated and solved analytically.

From this solution the evolution of the surface effective work function can be derived and from this an end-of-life criterion will be formulated later in §5.4.1.1.

Since the desorption rates and the effective work function are strongly dependent on the plasma characteristics a method to update the plasma parameters has been developed.

This method is semi-empirical and is based on the assumption of quasi neutrality, on the approximation that the heavy particle temperature is the same as the surface temperature and on the assumption that the dependence of the plasma parameters from time and space can be split in two separate functions.

The outputs of this model will be validated and commented on later in §5.4.

5 Results

In this chapter the results obtained with the models presented in §3-4 will be reported. We will first report the results relative to the diffusion coefficient calculation for barium oxide migration from the insert core to the surface (§5.1.1). The diffusion coefficient will be calculated performing a sensitivity analysis to match the barium oxide depletion predicted numerically with the one dimensional model to the experimental data reported in Ref [10].

Using the values of the diffusion coefficient so obtained the validation of the barium oxide depletion model will be performed using the data relative to the T5 Artemis cathode by QinetiQ (§5.1.3) and to the NSTAR cathode from the Deep Space One Long Duration Test (§5.1.4) and comparing them with the results obtained with the 3D cylindrical model.

The comparison with these experimental data will show both qualitative and quantitative agreement.

Once the depletion model has been validated we will move to the plasma parameter update process presented in §4.5.3 and then the deposition/desorption model will be tested simulating the cathode in Ref [22]. Using the data obtained from this simulation a criterion for the cathode end of life will be developed and then applied to the cathode in Ref. [2].

5.1 Barium Depletion Chemical Model [39] [40] [41]

5.1.1 Diffusion coefficient determination

In chapter §3 a model for barium oxide depletion from the insert has been presented. One of the unknowns of this model is the value of the diffusion coefficient D_a that globally represents all the diffusion processes that lead to BaO transport from the insert core to the insert surface.

To calculate this parameter and its behaviour with temperature and porosity a comparison with the data published by Roquais [10] will be done.

In Ref. [10] tungsten discs obtained by pressing tungsten powder of 4 - 5 μm average particle size and impregnated with a 4:1:1 $BaO\text{-}CaO\text{-}Al_2O_3$ impregnant have been inserted in tantalum cups welded to cylindrical tantalum sleeves, and then brought to the desired temperature (ranging from 950 to 1100 °C) by a heater.

The barium depletion from the insert has been then measured using EDX mapping, setting the location of barium depletion front at 50% of the EDX signal intensity on profiles of barium concentration.

With such an experimental set up BaO evaporation is supposed to occur only from the open surface producing a one-dimensional depletion profile.

The depletion profiles so found are in fact one-dimensional but barium oxide evaporation and consequent depletion has been found to occur also from the closed surface.

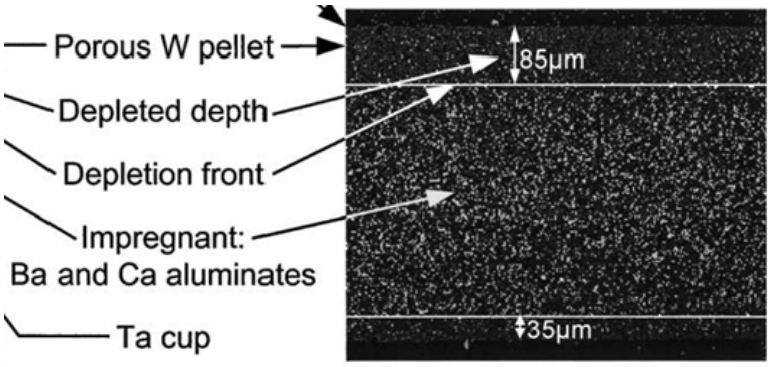

Figure 29 – Example of the depletion profile measure by Roquais [10]

To reflect this Eq. (52) will be numerically integrated using the scheme reported in §3.4 imposing that evaporation occurs at both ends of the insert and varying the value of the diffusion coefficient until the computed data match the measured ones.

The results are reported below

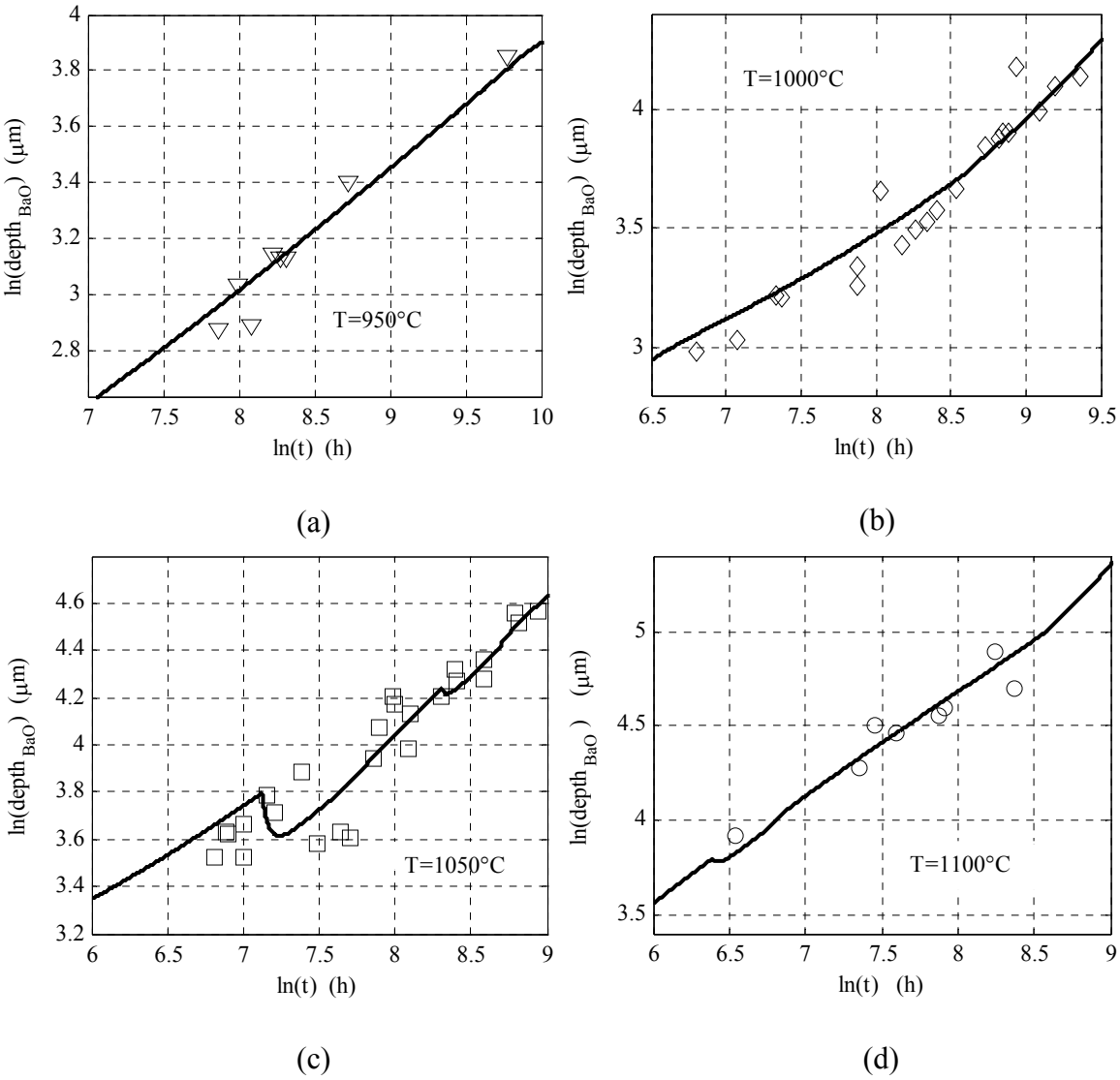

Figure 30 - Comparison between experimental and computed data. Π=0.186 (a) T=950 °C, (b) T=1000 °C, (c) T=1050 °C, (d) T1100 °C. Points are experimental values from Ref [10] solid lines are data computed with the model

As it can be seen in Figure 30 a very good agreement has been found between the prediction of the model and the experimental results obtaining numerical trends that closely fit the experimental points. The only discrepancy is found in Figure 30(c) relative to a temperature of 1050°C where a "knee" is present in the numerical data. Such a trend is quite strange but can be explained noting that at that time there is probably the transition from one area of the ternary diagram to another with the consequent drastic change in the evaporation rates.

Looking at the experimental data it can be seen how, at the time when the "knee" in the numerical data appears, some of the measured points (those relative to 3.6 μm) are quite far from an ideal mean-least-squares straight interpolating line suggesting that there might be also a physical explanation for this.

The values of D_a found are supposed to follow an Arrhenius trend ($D_a = e^{\frac{-qE_{D_a}}{k_b T}}$) hence interpolating the diffusion coefficient values with an exponential regression the activation energy of the diffusion process can be derived.

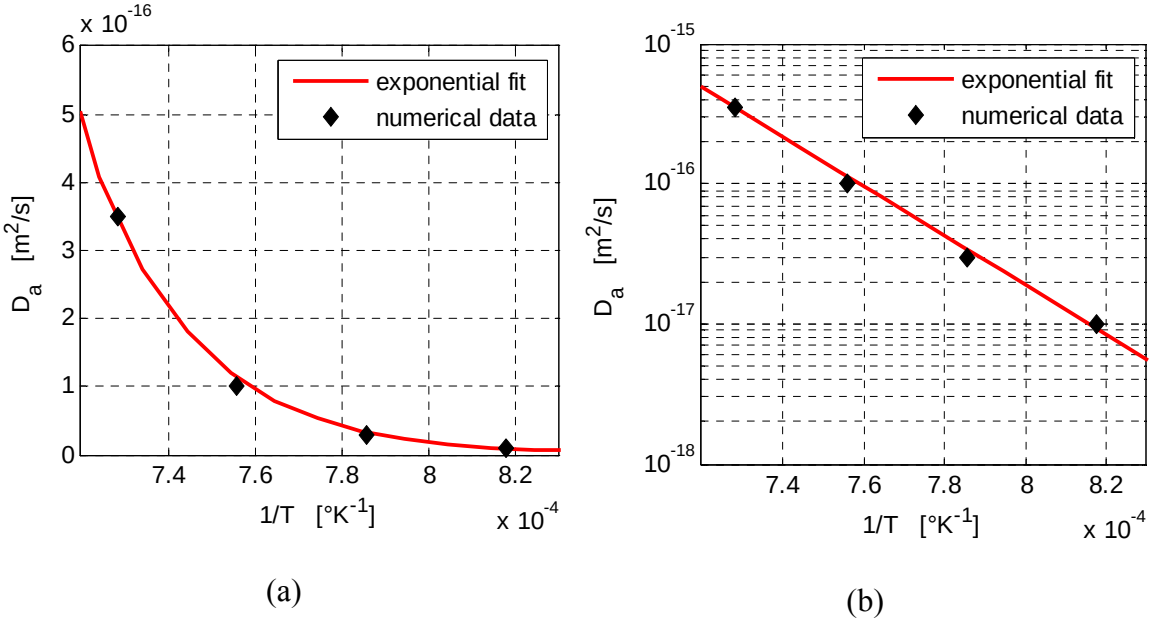

(a) (b)

Figure 31 - Arrhenius interpolation of the D_a values found numerically

The exponential interpolation shows an excellent fit to the numerical data with an R-square parameter of 0.997 (if R-square is equal to 1 the fit is perfect meaning that the fitted points belong to the fitting curve).

The derived activation energy (E_{D_a}) is equal to 3.5 eV.

We must point out that the value so calculated is a time average value of the diffusion coefficient since it is, in theory, not only a function of temperature but also a function of the local concentration of barium oxide, calcium oxide and alumina.

The activation energy is, as expected, close to the energy of evaporation of barium oxide (4.32 eV) but lower because the diffusion process involves just the movement of BaO inside the impregnant structure and not its complete detachment from this structure.

The diffusion coefficient has been calculated theoretically before in Ref. [11] as already pointed out in §2.2.1 and §3.3.

The values of the diffusion coefficient found according to the derivation reported in Ref [11] are reported below together with the values found numerically.

Table 9 – Comparison of the D_a values found numerically and with the theory developed in Ref [11]

Temperature °C	Numerical D_a [m^2/s]	D_a calculated from Eq. (46) Ref [11] [m^2/s]
1100	$3.5 \cdot 10^{-16}$	$7.42 \cdot 10^{-16}$
1050	$1 \cdot 10^{-16}$	$3.61 \cdot 10^{-16}$
1000	$0.3 \cdot 10^{-16}$	$1.66 \cdot 10^{-16}$
950	$0.1 \cdot 10^{-16}$	$0.72 \cdot 10^{-16}$

The values of D_a obtained from the numerical model and those obtained theoretically are of the same order of magnitude providing an evidence of the goodness of the model. The difference between them can be explained noting that the theoretical treatment derived in [11] does not take into account the evolution of the BaO – CaO – Al_2O_3 chemistry assuming that the barium atoms are migrating inside the barium crystalline structure.

From this assumption the value of the total activation energy ($E_f + E_m$) results to be lower (2.2 eV) than the one obtained numerically (3.5 eV) since the energy needed for barium evaporation is higher when it is bonded with calcium and alumina than when it is only bonded with oxygen as it can be easily noted looking at Table 2.

Another reason of the discrepancy between the theoretical and numerical data is that in the theoretical derivation the distance between two vacancies is assumed to be equal to $2R_{Ba}$ whereas this distance, being a function of the impregnate composition, depends on the chemical evolution of the BaO-CaO-Al_2O_3 system.

Since in Ref [11] there are also data relative to different level of porosity (in particular 0.167, 0.187 and 0.223) the same procedure used before has been applied to determine the trend of the diffusion coefficient with porosity. The values of D_a so found are reported below.

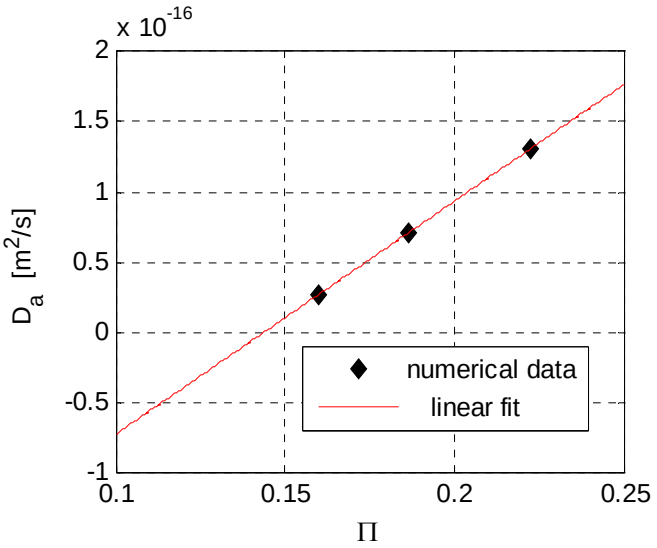

Figure 32 – D_a trend with insert porosity

In [10] Roquais assumes a linear trend of the diffusion coefficient with porosity. A linear interpolation is reported in Figure 32 showing a good fit of the data.

If the linear regression is extrapolated until the D_a value goes to zero a threshold value of the porosity can be found. This value is about 0.14.

The presence of a threshold porosity value has been explained by Roquais saying that under such a value the interconnection between the pores is too poor to allow for barium diffusion to the surface; in spite of this the presence of a porosity threshold value has not been reported in any experimental work hence this threshold value will not be considered valid and the interpolation here derived is hence reliable only between Π*=0.167* and Π*=0.223*.

Then, assuming that the diffusion coefficient is linearly dependent on the porosity and exponentially related to the inverse of the temperature, the diffusion coefficient formula is

$$\begin{aligned} D_a &= (b\Pi + c)\, e^{-\frac{qE_{Da}}{k_b T}} \\ b &= 0.1165\ m^2/s \\ c &= -0.01653\ m^2/s \\ E_{D_a} &= 3.5eV \end{aligned} \tag{114}$$

5.1.2 BaO depletion sensitivity to temperature profile

Before moving to the validation of the 3D cylindrical model, this model will be used to show the importance of the knowledge of the temperature profile along the insert. It will

be shown how, the use of different temperature profiles with the same average value, will produce depletion profiles and total depletion that are completely different.

To do so two simulations have been run using two different temperature profiles with the same average temperature.

These two profiles are reported below

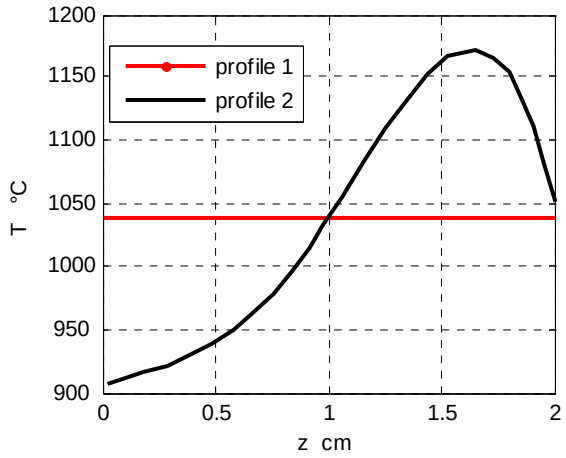

Figure 33 – Different temperature profile with the same average temperature

Usually temperature profiles along hollow cathode inserts do not present a peak like profile 2 in Figure 33 and are not flat like profile 1 but instead are more or less linearly increasing from the upstream region ($z = 0$) to the orifice plate end of the insert ($z = 2$).

The profiles in Figure 33 have been deliberately chosen to show how BaO depletion is more related to the maximum temperature in the profile than to its average value.

The insert has been simulated for 30,000 hours assuming that BaO evaporation occurs only from the inner and from the upstream surface of the insert and that at the beginning of life the insert is completely full of BaO (this means that at $t = 0$ the relative BaO density is 1 everywhere).

The colormaps showing BaO depletion from the insert after 30000 hours for the two cases are reported below

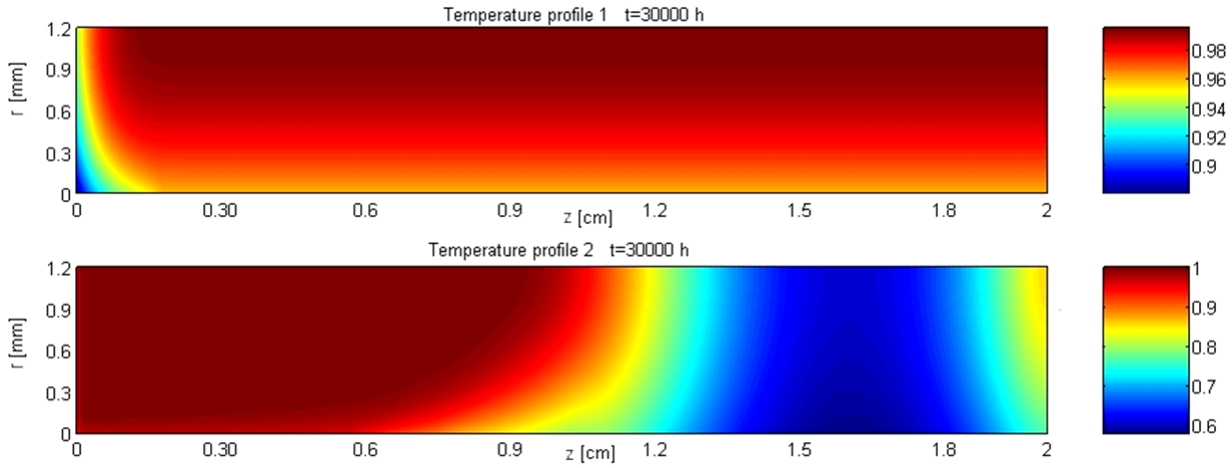

Figure 34 – Colormaps showing BaO content in the insert after 30000 hours of simulated operations

As can be easily noted from Figure 34 barium oxide depletion closely follows the temperature trend, higher depletion occurs where the temperature is higher because both evaporation and diffusion rate are exponentially proportional to it.

In the colormap relative to the first temperature profile the higher depletion at the upstream end is due to the fact that also the upstream surface is "open" to barium oxide evaporation.

The same effect is not noticed in the colormap relative to the second profile because of the different colorscale.

The evolution of the total BaO content inside the insert is show below for the two cases

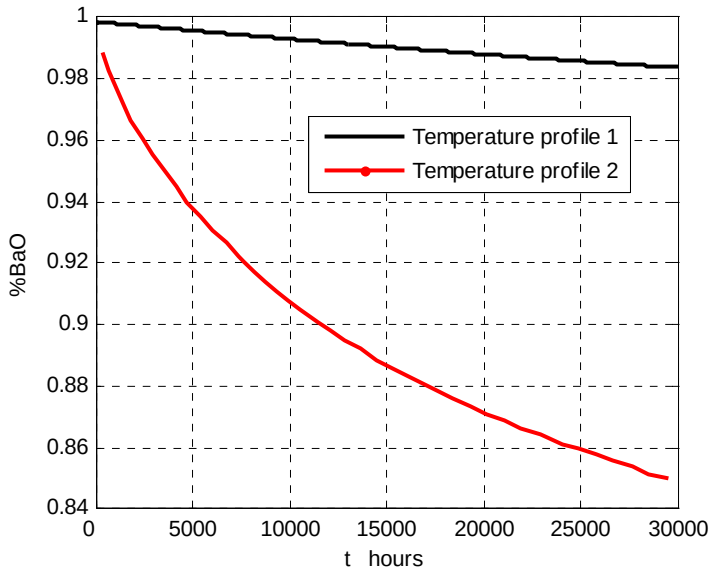

Figure 35 - Total Barium oxide content inside the insert versus time for different temperature profile

Looking at Figure 35 we can see that with $T = 1038\,°C$ after 30 thousand hours only 2% of the initial barium oxide content has evaporated, whereas with temperature profile 2, the evaporated barium is 15%.

Hence it can be seen how the knowledge of the temperature profile is far more important than the mean temperature values, because a high temperature spot causes an high local evaporation rate (since the evaporation rate is exponentially proportional to the temperature) and, at the same time, an high diffusion rate (since D_a is exponentially proportional to T) that allows more barium oxide to reach that spot and evaporate there.

Once the dependence of barium oxide depletion from the temperature has been shown we will move on to the validation of the depletion model comparing the numerical results with the experimental values measure by QinetiQ and at JPL.

5.1.3 Comparison with experimental result – QinetiQ [41]

QinetiQ, to prove the suitability of their cathode technology for future high-impulse long-duration missions such as Bepi-Colombo, has carried out an experimental campaign to test the T series of their cathodes [41].

The Artemis T5 cathode and the T6 cathodes were tested in representative discharge chamber conditions.

Four T5 cathodes have accumulated 15,000 hours of operation plus 5000 on/off cycles while two T6 cathodes have accumulated respectively 800 and 4000 hours of operation.

The anode voltage of all these cathodes has been recorded during the test showing no changes during the test meaning that the cathodes were most probably far from their end of life.

After the 15,000 hours test one of the T5 cathodes has been destructively analyzed. Both the insert and the cathode tube were analyzed.

The external surface of the T5 insert was found to be covered in a greenish white crust (Figure 36). This crust has been subjected to an EDX analysis that indicated that it was primarily barium containing impregnated material. The T5 cathode tube was found to mirror this, with a similar barium containing deposit covering its inner bore.

(a) (b)

Figure 36 - (a) Exterior surface of T5 cathode insert after 15,000 hours showing barium containing crust. (b) Interior surface of T5 cathode tube showing barium containing deposit [41]

These results are in agreement with previous observation relative to the NSTAR cathode [2] where similar deposits on the cathode tube internal surface have been found. This observation together with the observed depletion from the closed surface of the tantalum cups made by Roquais ([10] and §5.1) indicates that the impregnate reaction products escape from all available surfaces and not just the insert's inner and upstream surface.

The insert of the T5 cathode has been fractioned and analyzed using a Scanning Electron Microscope EDX to map the Lα lines of barium and the Mα line of tungsten.

The result of this experimental analysis is reported in Figure 37 where the region extending 1.6 mm upstream of the orifice plate (downstream end of the cathode) is presented.

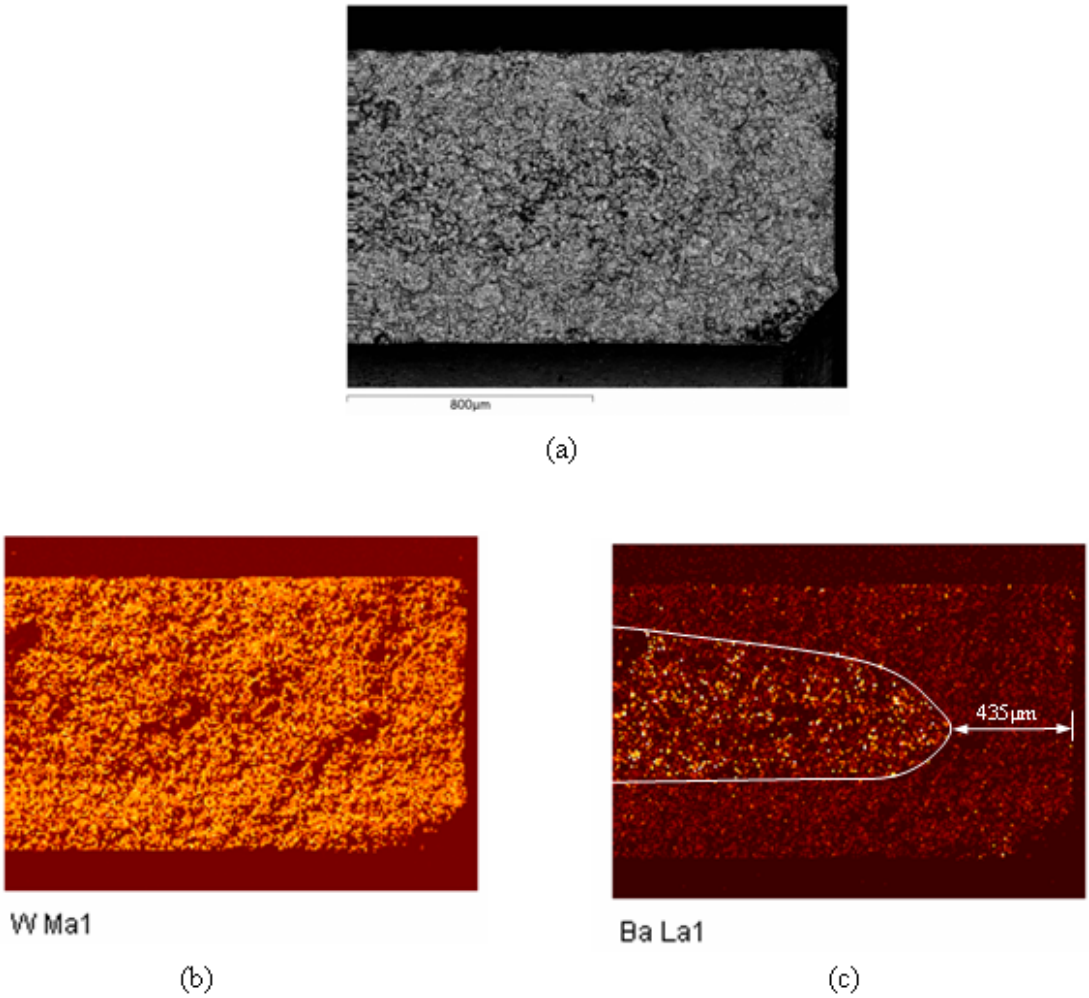

Figure 37 - EDX analysis of a fractured 15,000 Artemis T5 insert downstream end. (a) Backscattered electron image of downstream end (b) EDX mapping of Tungsten Mα line (c) EDX mapping of Barium L α line, showing 435 µm of depletion from the downstream face after 15,000 hours of operation [41]

Figure 37 (a) and (b) are respectively a backscattered electron image of downstream end of the cathode and an EDX mapping of Tungsten Mα line. To the extent of barium oxide depletion detection the most important data are the one reported in Figure 37 (c). In Figure 37 (c) the darker zones indicate areas where barium has been depleted whereas the brighter ones stand for areas where a high content of barium is still present. Unfortunately no quantitative data on barium depletion have been derived from this analysis hence from the picture above the barium depletion radial and axial profile can be only qualitatively derived. In particular it can be seen how the depletion takes a "tongue" shape at the downstream end of the cathode with a depletion depth of 435 µm from the orifice plate.

Also the T6 cathodes operated for 800 and 4000 hours have been sectioned and analyzed using EDX scanning. The 800 hour cathode showed "*pristine conditions*" [41] with no appreciable depletion whereas the 4000 hour insert was accidentally fractured during the analyses.

The T5 and T6 cathode will be now simulated for 15,000 hours with the model presented in §3.5. The insert temperature profiles used to run these simulations are the ones measured by QinetiQ prior to the testing of the cathodes at the same operating conditions (Figure 38)

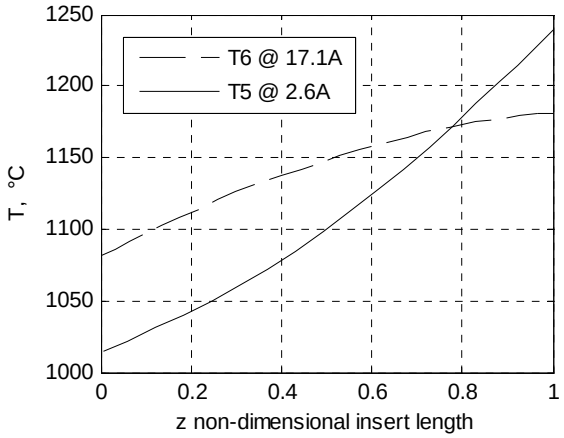

Figure 38 – T5 and T6 insert temperature profiles

We will also assume that at the beginning of life the barium content inside the insert is maximum with the insert perfectly filled by the impregnate with an homogeneous barium distribution. We will impose evaporation to occur from the upstream surface and from the internal and external surface of the cathode as shown by the experimental observations.

The colormap relative to barium oxide depletion from the insert of the 800 hours T6 cathode is reported below

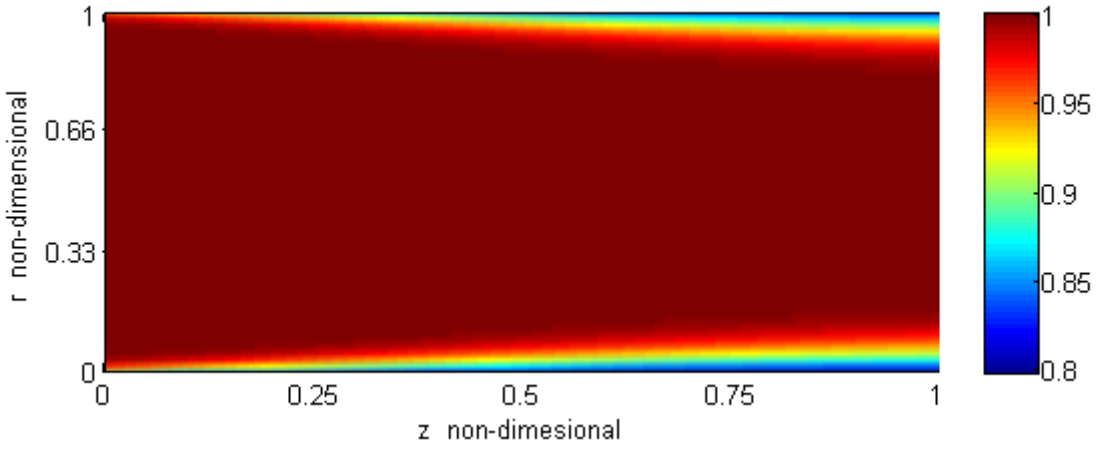

Figure 39 – Barium colormap of the T6 cathode after 800 hours at 17.1 A

As can be seen in Figure 39 the model predicts a very low level of depletion as observed in the experimental analyses.

To have a better comparison between numerical and experimental data the barium colormap relative to the T5 after 15,000 hours of functioning is reported below.

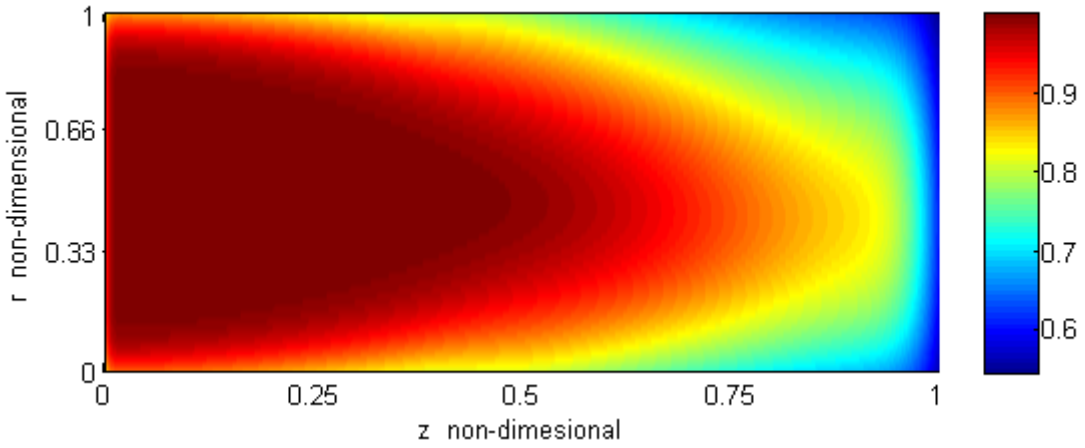

Figure 40– Barium colormap of the T5 cathode after 15,000 hours at 2.6 A

In Figure 40 a shape similar to the "tongue" found in the experimental analyses of the cathode can be seen. To verify the similarities between the computed and measured depletion profile the same downstream area of the cathode is reported in the next figure.

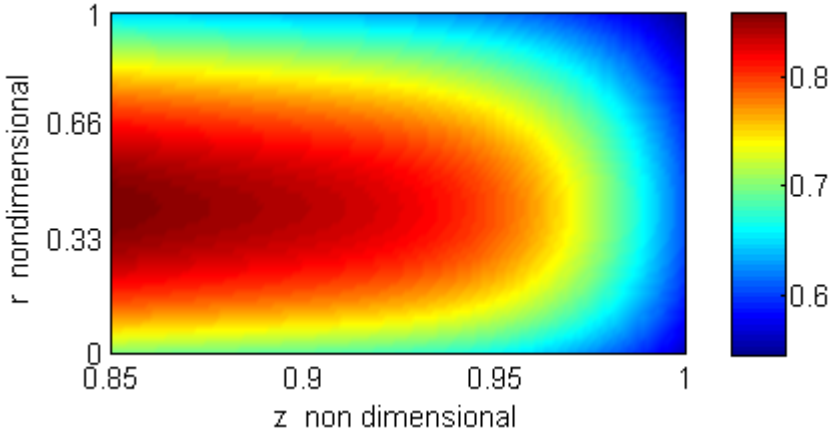

Figure 41– Barium colormap correspondent to the measurements in Figure 37

From Figure 41 it is clear how the qualitative trends of the computed and measured profiles are quite close. To judge how good this agreement is we will take the barium iso-depletion contour relative to 435 μm of depletion from the orifice plate and superimpose it to the experimentally derived figure.

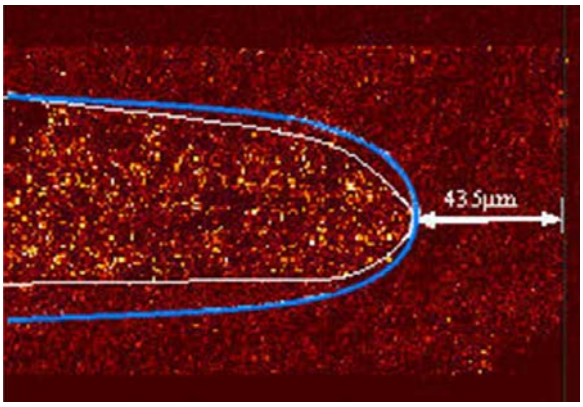

Figure 42 – Comparison between the experimental depletion profile(white line) and the correspondent barium iso-depletion contour (blue line, correspondent to 74% of the initial BaO content) calculated numerically

The barium iso-depletion line is relative to a residual amount of BaO equal to 74% of the initial content.

As it can be seen the barium iso-depletion line closely follows the experimentally derived depletion profile. The line follows the experimental result very closely in this top part while the bottom one is a bit more distant.

The reason of this could be that the model, having the outer and inner diameter surface perfectly free to evaporate BaO, presents a strong symmetry whereas this symmetry is probably non-realistic since the outer surface of the cathode is still enclosed by the cathode tube hence allowing evaporation of barium oxide until the deposition over the cathode tube will fill the gap existing between it and the insert.

As it can be seen in Figure 38 the temperature profiles for the T6 cathode at 17.1 A and the T5 at 2.6 A have similar trends with the T6 having an higher mean value (1142 °C) but a lower temperature gradient along the insert whereas the T5 has a lower mean temperature value (1104 °C) but a higher gradient with a maximum temperature value of 1240 °C against the 1180 °C of the T6 profiles.

It might be interesting to compare the different barium oxide depletions of these two cathodes. To do so the barium oxide colormap relative to the T6 cathode after 15,000 hours is reported below.

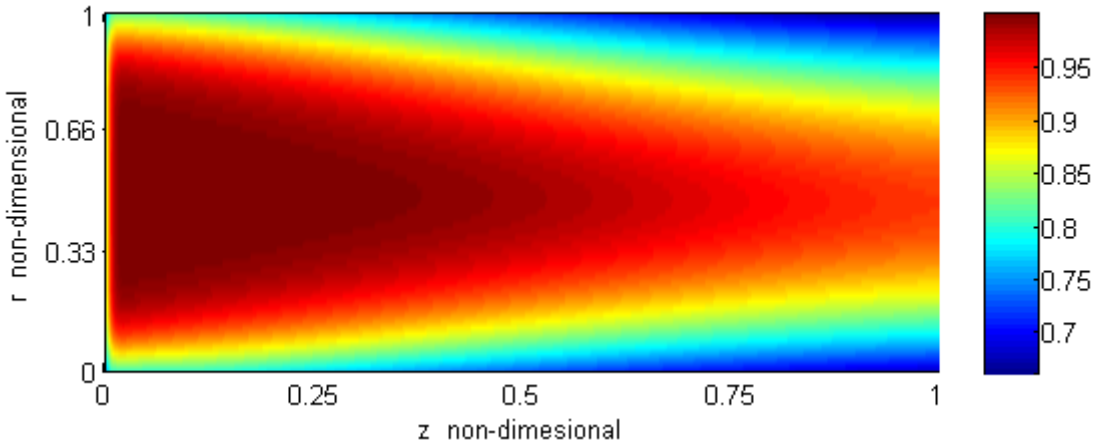

Figure 43 - Barium oxide colormap of the T6 cathode after 15000 hours at 17.1 A

To better visualize the difference in the depletion for these two cathodes a colormap with the difference between the barium content in the T6 and T5 is reported below where the numbers on the colorbar represent the increase (positive value) or decrease (negative value) in the barium oxide content in the T6 with respect to the T5.

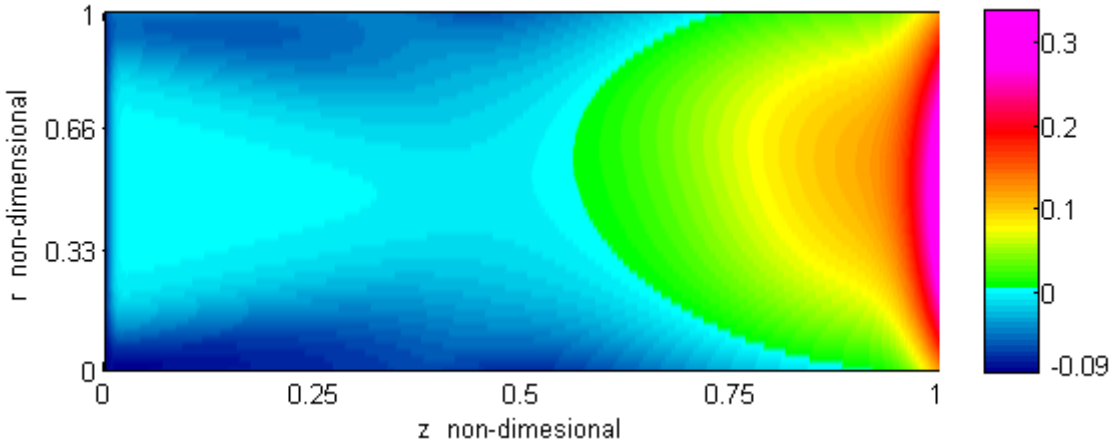

Figure 44 – Difference between the barium oxide content of the T6 and the T5 after 15,000 hours

As it can be seen the effect of the temperature peak of the T5 profile is much stronger than the effect of the higher average temperature of the T6 profile since in the downstream end the T6 has between 10% and 30% barium oxide more than the T5 (referred to the barium oxide content at the beginning of life) while in the upstream end the T6 has only up to 9% barium oxide less.

Below the total barium oxide content evolution with time for both T6 and T5 is reported

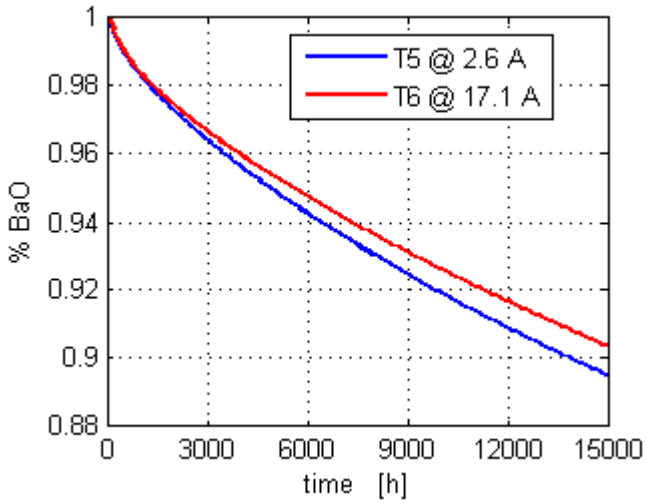

Figure 45 – Total barium oxide content inside the T5 and T6 cathode with time

As it can be seen even if the downstream of the T6 the local oxide barium content is much higher than the T5 one the total oxide barium oxide content in the T6 is slightly lower due to the fact that the average temperature is about 35°C higher.

The T6 cathode has also been simulated for 15,000 hours at various throttle conditions corresponding to 11, 13, 15, 17, 19, 20 Amperes of total current.

The temperature profiles for these throttle conditions have been measured at the beginning of the tests at QinetiQ and are reported below together with the trend of the total barium oxide content inside the insert with time.

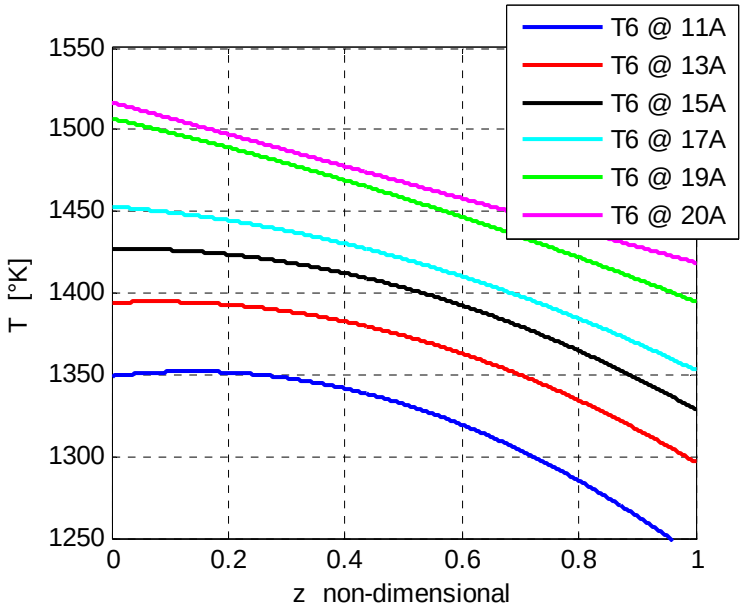

Figure 46 – T6 temperature profiles at different cathode currents

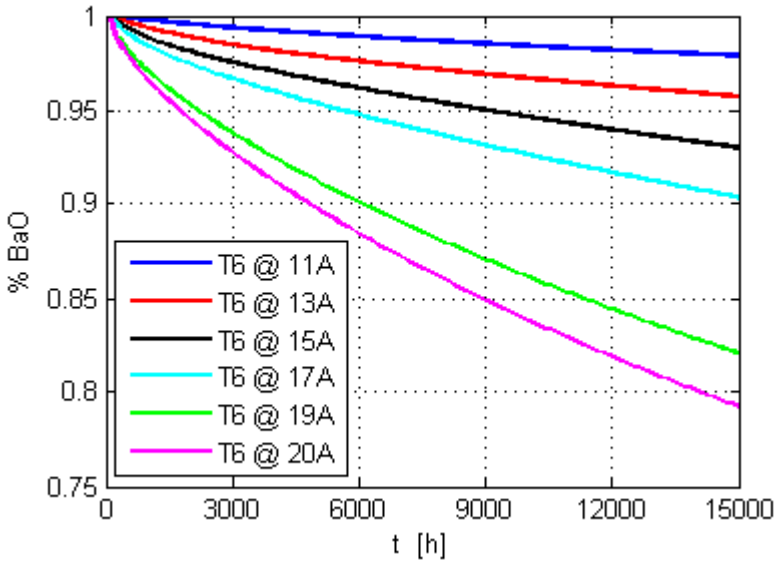

Figure 47 – Total barium oxide content inside the T6 at different cathode currents

As expected the total barium oxide current follow the temperature trend showing lower barium oxide content for higher temperature profile and in particular for the 19 and 20 Ampere case.

It must be noted how the T6, if operated up to 15 A, even if its current levels is much higher than the T5, exhibits lower barium oxide depletion thanks to its lower insert temperature.

In conclusion the chemistry of the T5 and T6 cathode has been simulated showing good qualitative agreement (since no quantitative data is available) with the experimental data measured by QinetiQ and the effect of the temperature profile on the barium oxide content inside the insert has been shown using the data relative to the T5 cathode at 2.6 A of current and to the T6 at 11, 13, 15, 17, 19 and 20 amperes.

5.1.4 Comparison with experimental result – NASA NSTAR ELT cathode*

As part of Deep Space 1 life test the NASA NSTAR ELT discharge cathode has been run for 30,372 hours at different throttle levels as reported below.

* All the experimental results reported in this section are taken from Ref. [2].

Table 10 - ELT discharge cathode throttle settings [2]		
TH level	Accumulated hours	Discharge Current
12	0 - 500	9.9
15	500 - 4800	13.5
8	4800 - 10500	7.6
15	10500 - 15500	13.5
0	15500 - 21500	4.9
15	21500 - 25500	13.5
5	25500 - 30000	6.9

After 30,372 hours the test has been stopped intentionally and the cathode has then been sectioned and analyzed by means of EDX scanning and to measure the Ba/W ratio in various points of the insert.

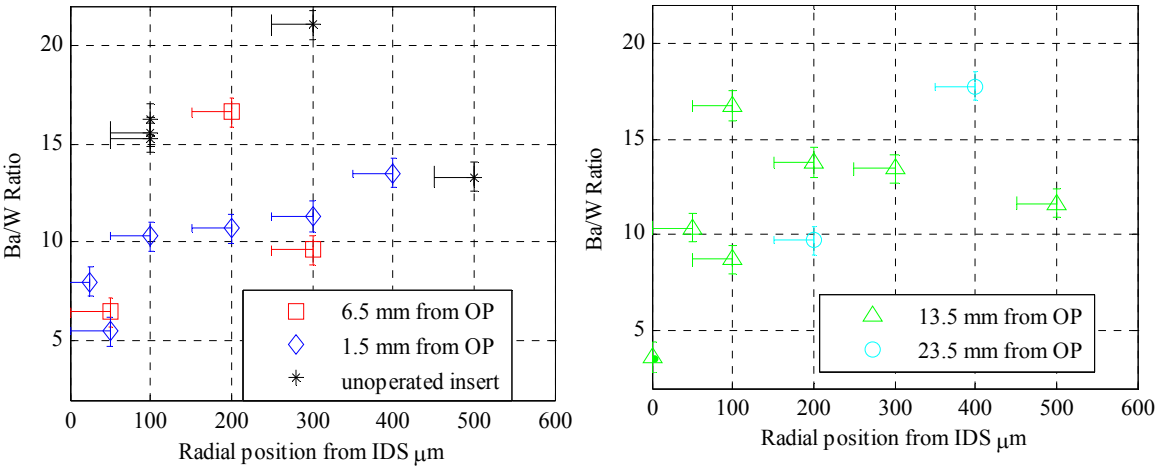

Figure 48 – Ba/W ratio value for different radial and axial position [2]

The barium-over-tungsten ratio has been also measured before the beginning of the test as shown by the black points in Figure 48. Looking at these data two hypotheses relative to the initial barium content in the insert have been made.

The first hypothesis is that at the beginning of the test the insert is completely filled with the impregnate, hence the initial BaO profile is flat (dashed line in Figure 49) with a value that is the average of the measured values.

The second hypothesis is that due to the impregnation process the BaO profile is not flat; in this case its trend has been derived interpolating the measurements (solid line in Figure 49).

The two profiles are represented below

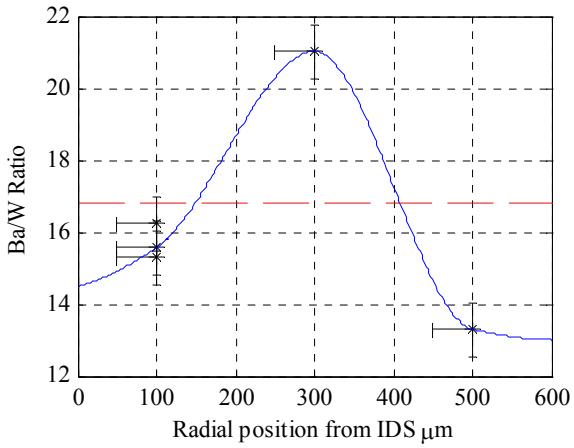

Figure 49 - Different initial BaO profile.

The temperature profiles needed to simulate the insert chemistry, when possible, has been taken directly from the literature [25] otherwise they have been derived interpolating the published profiles assuming a linear trend of the insert temperature with the discharge current (Figure 50).

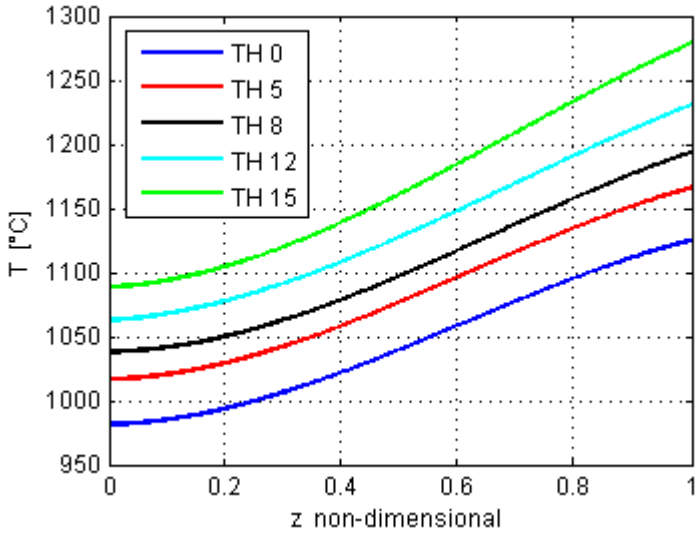

Figure 50 – Temperature profiles for the different throttle levels [25]

The insert has been simulated with both the flat and the interpolated initial BaO profile and assuming evaporation to occur always from the inner diameter and from the upstream surface whereas different simulation have been done regarding the conditions of the outer diameter and orifice plate surface.

The complete set of boundary conditions used is reported in Table 11 where with "open" we indicate a surface where evaporation occurs and with "closed" a surface where it does not.

Table 11. Different set of boundary conditions				
	Boundary Conditions Set 1	Boundary Conditions Set 2	Boundary Conditions Set 3	Boundary Conditions Set 4
Flat BaO profile	IDS = open US = open ODS = closed OP = closed	IDS = open US = open ODS = open OP = closed	IDS = open US = open ODS = closed OP = open	IDS = open US = open ODS = open OP = open
Interpolated BaO profile	IDS = open US = open ODS = closed OP = closed	IDS = open US = open ODS = open OP = closed	IDS = open US = open ODS = closed OP = open	IDS = open US = open ODS = open OP = open

The best results have been obtained using BC Set 1 and 2 where the orifice plate surface is "closed".

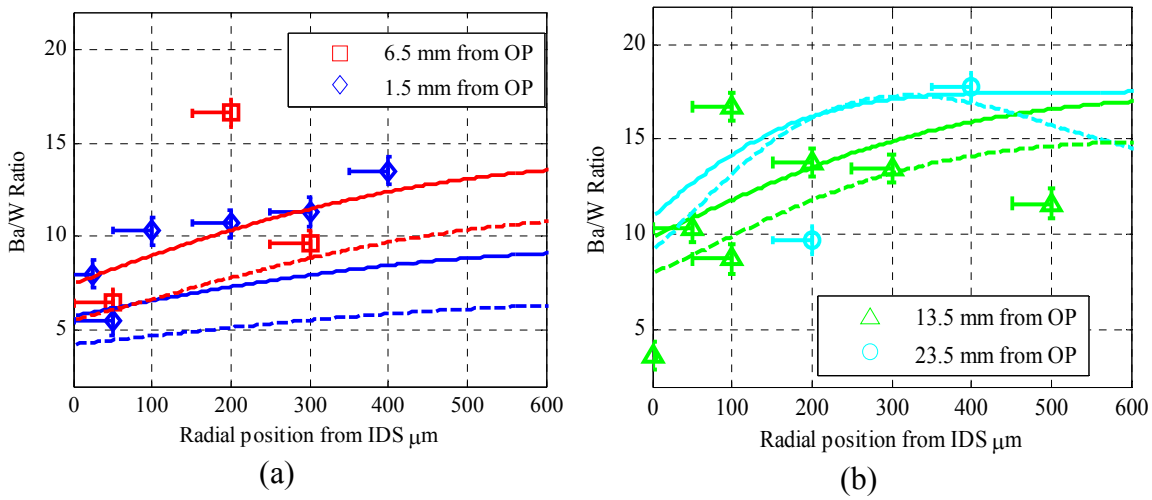

Figure 51 – Comparison between numerical and experimental results
BC Set 1. solid line = flat profile, dashed line = interpolated profile

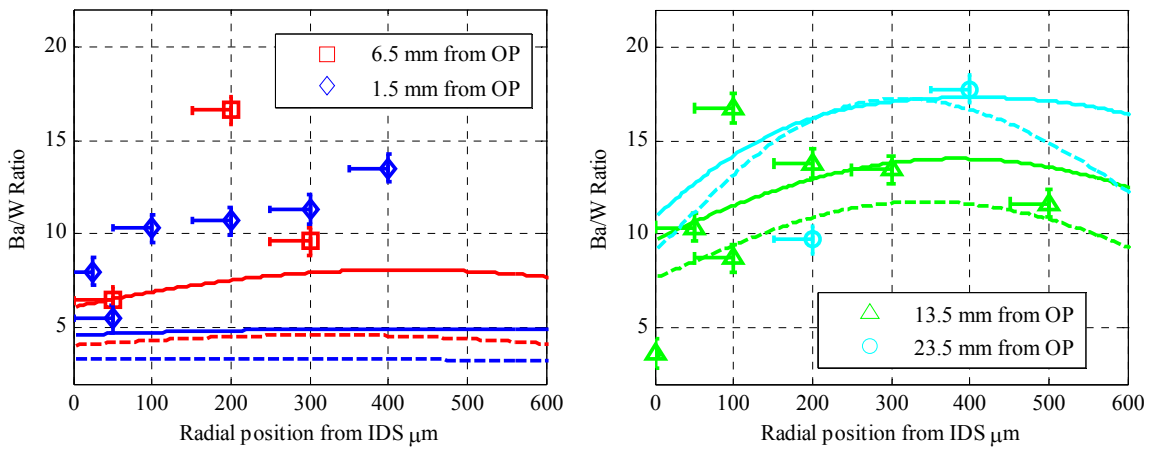

(a) (b)

Figure 52 – Comparison between numerical and experimental results BC Set 2. solid line = flat profile, dashed line = interpolated profile

Looking at Figure 51 and Figure 52 it can be see how the data relative to 13.5 and 23.5 mm from the orifice plate have generally a better agreement with the experimental measurements than the one relative to 1.5 and 6.5 mm.

This can be explained noting that the data relative to 13.5 mm from the orifice plate refer to the middle of the insert (since its length is 25 mm) where the effect of the boundary conditions on the upstream and downstream surface is weakest, and noting that the data relative to 23.5 mm refer to the upstream surface that is clearly open to evaporation simplifying its simulation. It must also be said that at the upstream end of the cathode the temperature is relatively low reducing the effect of barium oxide evaporation.

Looking at the data relative to 13.5 and 23.5 mm from the orifice plate it can be also noted how the data relative to the flat initial barium oxide profile (solid lines) show a better agreement with the experimental data than those relative to the initial interpolated BaO profile.

Hence in the next simulations we will assume that the initial barium oxide content profile is flat avoiding to use the interpolated profile.

Looking at the data relative to 1.5 and 6.5 mm from the OP it can be noted how the agreement between numerical and experimental data is generally poor; this can be explained noting that these data are the ones that are most influenced by the boundary conditions on the orifice plate and that, being in the area of the cathode with the highest temperature, they are heavily influenced by any difference between the real conditions experienced by the cathode insert and the condition imposed in the simulation (like insert temperature profile, initial barium oxide content and boundary conditions).

Comparing Figure 51 and Figure 52 it can be seen how in the upstream end of the cathode the agreement between the experimental data and the numerical one is better with BC2 than with BC1 whereas in the downstream end the contrary happens.

Considering what said above and considering that in the destructive analyses of the NSTAR cathode barium deposition has been found on the external surface of the insert [2] (as already happened with the QinetiQ T5 cathode) we will consider BC Set 2 to be the boundary condition set that best represent the real conditions of the cathode functioning.

To improve the results of the simulation we will now take into account the effect of the outer insert surface.

This surface, as shown by the experimental investigation, is open to barium oxide evaporation nevertheless the evaporation will probably not occur from this surface during the whole cathode life. BaO evaporation from the insert external surface must be imputed to the presence of a small gap between the insert and the cathode tube.

The barium oxide evaporated from the external surface of the insert creates deposits on the cathode tube as observed in [2]. If these deposits are big enough to fill completely the gap between the insert and the cathode tube they will end up occluding the insert pores preventing BaO evaporation.

Several numerical simulations have been run using BC set 2, assuming an initial flat BaO content profile and assuming different gap size between the insert and the cathode tube.

The gap sizes used are 25, 50, 75 and 100 μm. The best results were obtained with 100 μm.

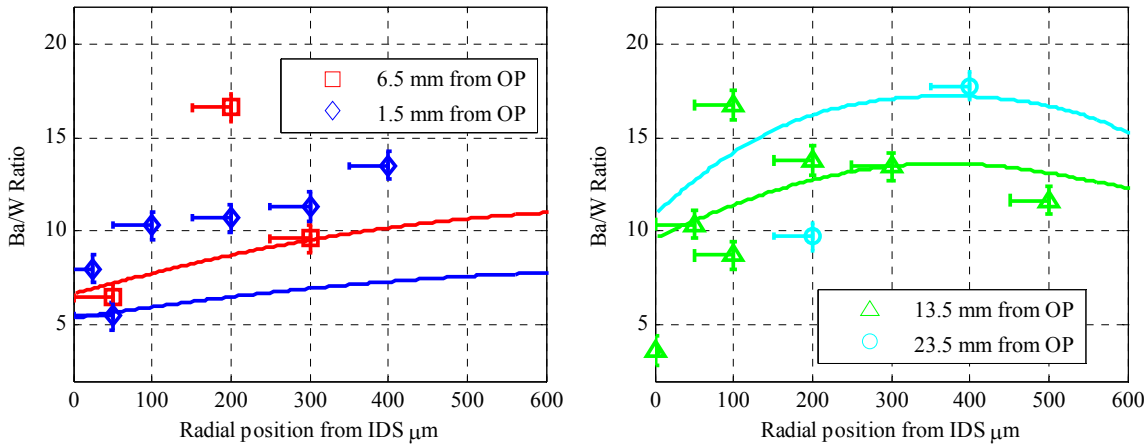

Figure 53 - Comparison between numerical and experimental results
IDS deposition Eq. 2, ODS – cathode tube gap = 100 μm

The numerical results relative to 1.5 mm in Figure 53 show a very poor agreement with the experimental data. This can be explained noting that the downstream area of the cathode has been reported to be influenced by tungsten deposition and erosion [17]. These processes are not included in the model and hence a discrepancy between the numerical and the experimental data must be expected. In particular the computed data are conservative underestimating the barium oxide content inside the insert.

Regarding the data relative to 6.5 mm from the OP it can be noted that the experimental trend is quite unusual showing a peak of barium content at one quarter of the insert thickness.

If we neglect the point relative to 6.5 mm from the OP and 200 μm from the IDS the computed data are in good agreement with the experimental ones.

Looking at the data relative to 13.5 and 23.5 mm from the OP we can note that these data are not influenced by the introduction of deposition effect hence showing the same good agreement with the experimental data shown in Figure 52 by the data relative to the flat initial profile.

In conclusion the chemistry of the ELT cathode has been successfully simulated showing how the agreement between the computed and the experimental data improves when the boundary conditions get closer to the real functioning of the cathode showing not only the goodness of the model but also its sensitivity to different operating conditions of the cathode.

5.2 Chemical model conclusions

The first model that takes into account both BaO diffusion in the insert and the BaO-CaO-Al_2O_3 chemistry has been formulated in §3 and the results obtained with this model have been reported in this chapter.

The chemistry used in this model is based on pure chemical data (no "data fitting" process has been done to modify such data) whereas the diffusion coefficient has been derived with a sensitivity analysis to best-fit the depletion measurements published in Ref [10].

The diffusion coefficient values so found respect the theoretical expectation following an Arrhenius trend with an activation energy close to the one relative to barium oxide evaporation.

The values have also been compared to the theoretical calculation performed in Ref [11] showing a good qualitative agreement. The quantitative discrepancy between the data calculated in [11] and the one found with this model has been explained and is mainly due to the assumptions formulated in [11] to arrive to an analytical expression of the diffusion coefficient neglecting the chemistry of the BaO-CaO-Al_2O_3 system.

The model has then been validated with the experimental data by QinetiQ and NASA Jet Propulsion Laboratory.

A qualitative agreement has been found with the data from QinetiQ since no quantitative data are available.

For the data from the NSTAR cathode a good quantitative agreement has been found. In the areas of the cathode where this agreement was not satisfactory (close to the orifice plate) the boundary conditions have been modified according to the experimental evidences to closely represent the real functioning conditions of the cathode. This has produced data that are in close agreement with the experimental measurements in every area of the insert.

The sensitivity of the model to the temperature and to the boundary conditions has been presented showing how, the closer the conditions imposed in the simulation are to the real functioning of the cathode the better the agreement between experimental and numerical data, confirming the goodness and the physical and chemical correctness of the model.

Considering what is said above we can conclude saying that the model developed in §3 and tested in this chapter is the first model able to simulate the chemistry of barium oxide depletion of a three-dimensional cathode insert providing results that are in reasonable agreement with the measurement.

5.3 Plasma Parameter Update

Prior to start using the surface coverage model developed in §4.5 the plasma parameter update process must be validated.

In this section the procedure developed in §4.5.3 will be tested with the data available in the literature relative to the same cathode that will be simulated later in §5.4.

In Ref [3] and [36] the data relative to NSTAR cathode electron temperature, ion/electron number density and plasma voltage have been reported relatively to discharge currents of 7.6 (TH8), 12 and 13.5 A (TH13).

To simulate the NSTAR cathode the plasma characteristics relative to the throttle level TH12, TH5 and TH0 are needed; these data will be derived using the parameter update process described in §4.5.3 assuming that the ion/electron density is constant among all the TH levels.

If we compare the densities relative to 7.6 A, 12 A and to 13.5 A of discharge current we can see how these three trends are quite close even if from TH15 to TH8 the discharge current drops to almost half of its value.

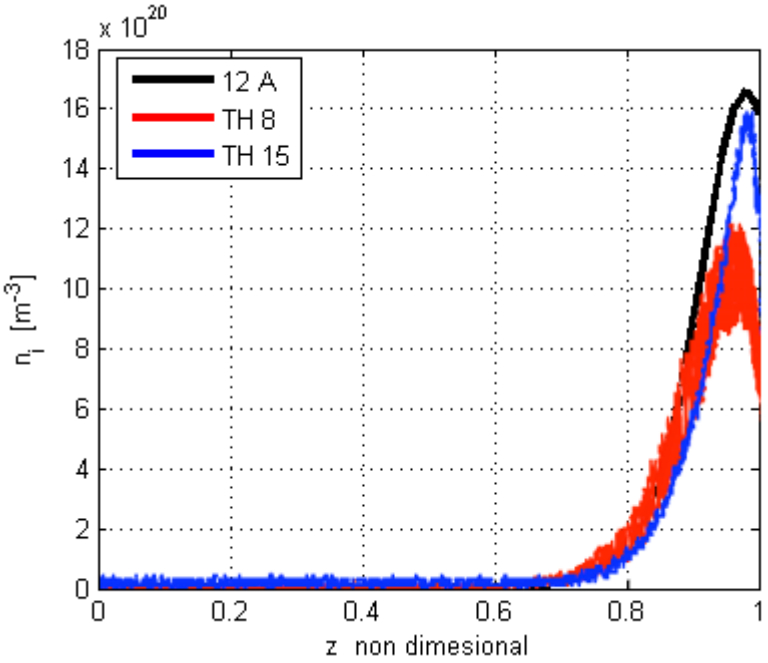

Figure 54 – Ion density at TH15, TH8 and at 12 A of discharge current [3], [36]

Since the ion density relative to 12 ampere of discharge current is the highest between the measured ones if we assume that the ion density is constant for all the THs and equal to the one relative to 12A we will most probably overestimate n_i hence overestimating the ion sputtering desorption rates. An overestimation of the desorption

rates will produce and underestimation of the low-work-function-coverage hence predicting an higher value of the work function (worse performances of the cathode) finally producing conservative estimates of the cathode lifetime.

Once the hypothesis of constant ion/electron density has been done the axial trend of ΔV and T_e can be derived from the measured data relative to 12 A whereas the radial profile of these quantities will be neglected due to the lack of such information (the radial profiles have never been measured) and to the fact that the sheath thickness is much smaller than the cathode radius.

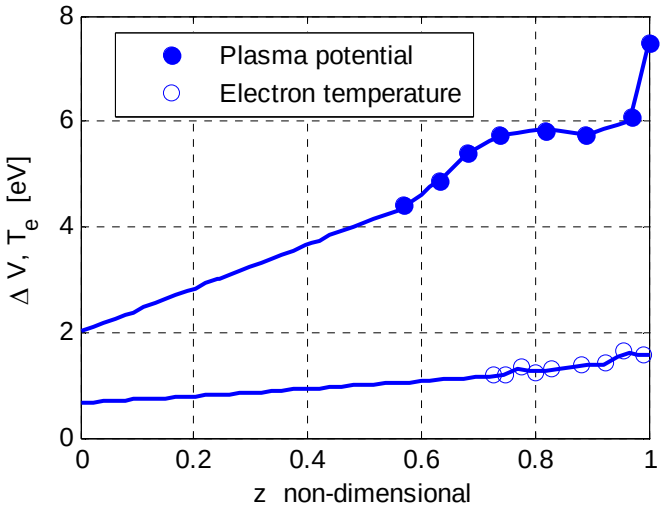

Figure 55 – Measure plasma potential and electron temperature (circles) for 12 A and assumed fitting profiles (solid lines) [36]

Using the hypothesis of constant n_i and the profiles of ΔV and T_e shown above, solving Eq. (13) and (15), the plasma voltage and electron temperature of every TH level can be derived.

Below is a comparison between the calculated values of ΔV and T_e, and the experimental ones for TH15 and TH8 reported in Ref. [3].

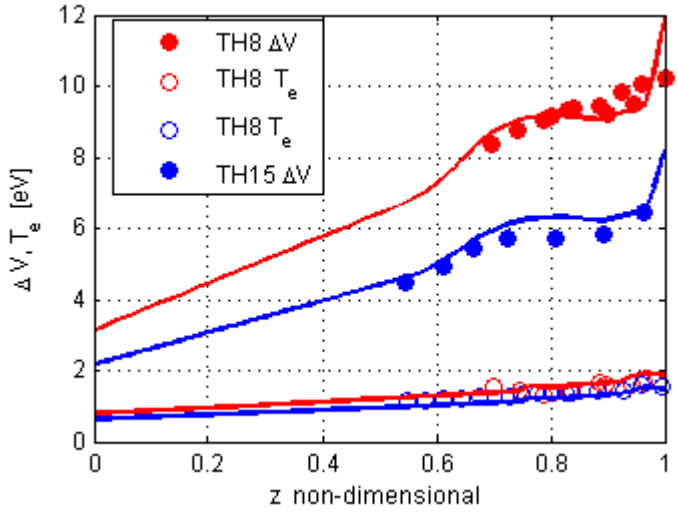

Figure 56 – Comparison between calculated and measure plasma parameters for TH8 and TH15

As it can be seen the computed data show a very good agreement with the measured one proving the goodness of the plasma parameters update procedure shown in §4.5.3.
Once this procedure has been validated the plasma parameters of the remaining throttle levels can be calculated. The results are reported below.

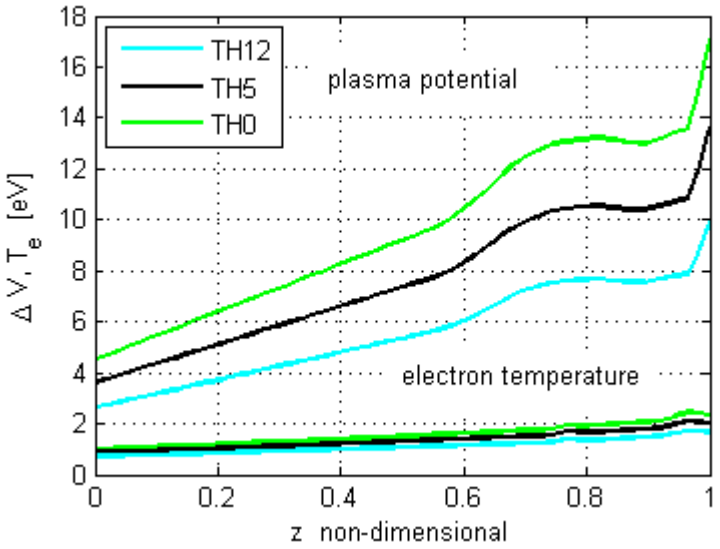

Figure 57 – Calculated plasma voltage and temperature profiles for TH12, TH5 and TH0

As it can be seen the plasma voltage tends to increase as the discharge current decrease. This can be explained looking at the thermionic emitted current for each throttle level and comparing them with the discharge currents.

Table 12 – Emitted and discharge currents

TH level	Emitted currents [A]	Discharge Current [A]
0	9.07	4.9
5	13.46	6.9
8	16.85	7.6
12	22.8	9.9
15	32.3	13.5

The cathode insert always emit currents that are in excess of the desired discharge current value, this means that for every TH the electron flux must be modulated by the interaction of electron temperature and voltage fall so that the total current flowing into the cathode is equal to the value fixed by the power supply (discharge current).

Since the variations in electron temperature are small and the electron density is assumed to be constant, the plasma voltage will be the parameter that mainly influences the electron flux.

Since the electron flux needed at lower discharge currents is smaller than at the higher ones and since the higher plasma voltage the lower is the electron current, the plasma voltage must be higher at low THs than at high THs hence explaining the trend shown in Figure 56 and Figure 57.

5.4 Deposition model

In this chapter the surface coverage model developed in §4.5 will be tested with the hollow cathode operated for 28,000 hours by Sarver-Verhey [22], [23] and with the ELT NSTAR cathode [2].

Using the data obtained from the cathode tested in [22] and [23] an end of life criterion will be developed. This criterion will be then used to predict the life of the NSTAR cathode.

5.4.1 28,000 hours cathode simulation

The cathode reported in Ref [22] and [23] has been tested for 28,000 hours at 12 A of discharge current.

We will assume that its insert temperature profile and plasma parameters are the same as those reported for the NSTAR cathode at 12A.

Using this assumption the cathode surface has been simulated for 28,000 hours. During this simulation the plasma parameters have been updated every 50 hours assuming the electron temperature to be constant during the whole simulation of the cathode.

This assumption can be justified noting that the plasma temperature has shown small variations over a wide range of discharge currents and emitted currents (Figure 55-Figure 57) whereas the plasma voltage has shown to be deeply dependant on the emission and discharge currents.

Regarding the ion density we can note that if the thermionically emitted current drops below the discharge current value the ion flux from the plasma to the surface must become big enough to overcome the electron flux providing the additional current needed to reach the discharge value. Hence a reduction in the emitted current due to a reduction in the surface coverage will result in an increase of the ion density (to increase the ion current) and in an increase of the plasma voltage to decrease the electron current that, otherwise, since quasi-neutrality has been assumed, will increase proportionally to the ion flux.

The computed surface coverage relative to Ba_3WO_6 and $BaWO_4$ and the work function evolution are reported below

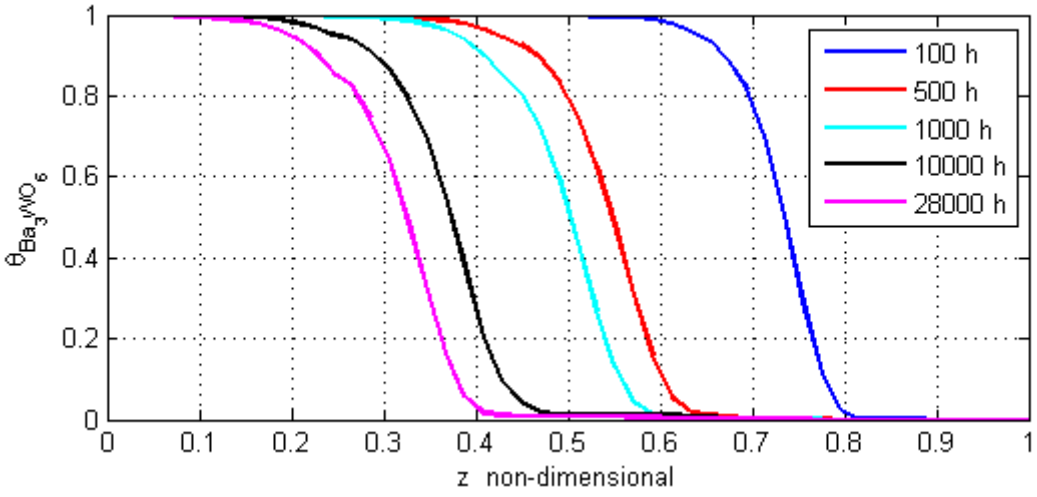

Figure 58 – Ba_3WO_6 surface coverage – 12A

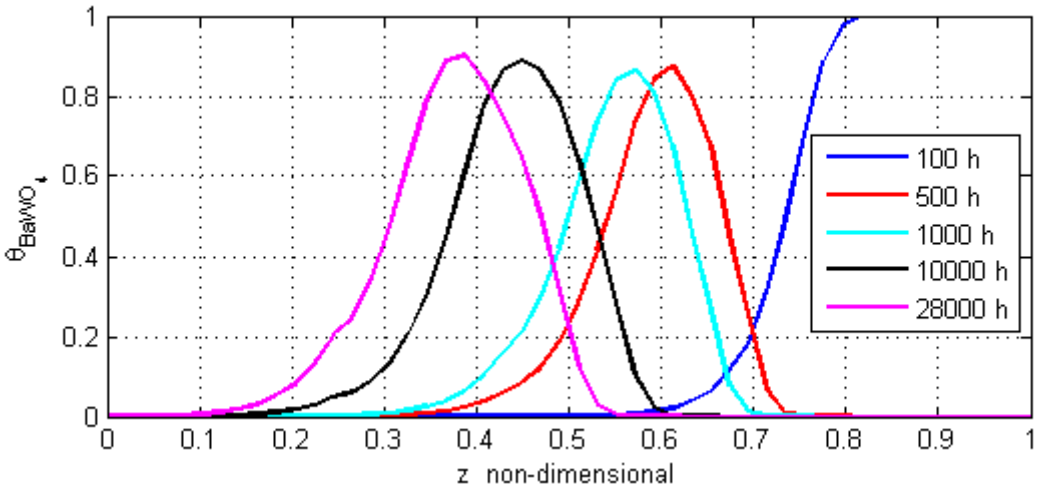

Figure 59 - $BaWO_4$ surface coverage – 12A

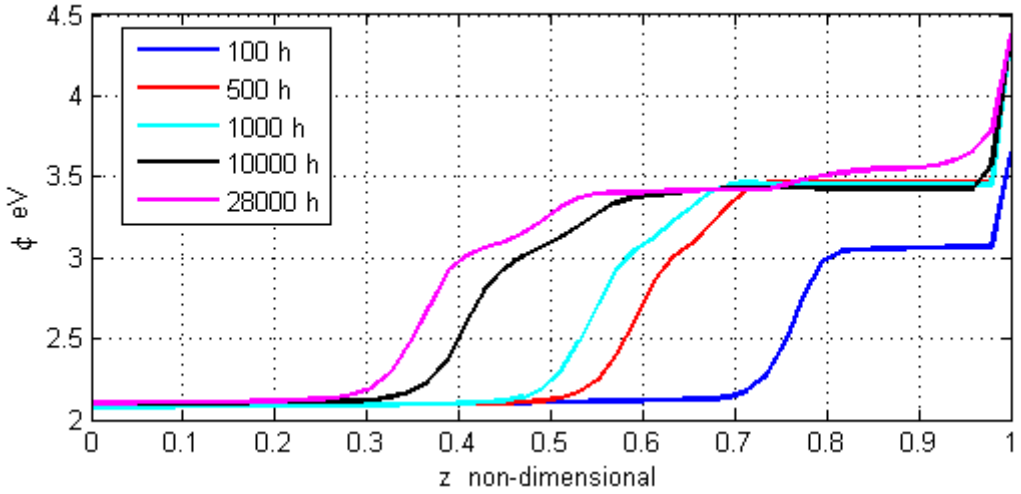

Figure 60 – Surface work function – 12A

As it can be noted in the figures above the low work function compounds depletion starts at the downstream end of the cathode and then slowly moves upstream. This is due to the fact that the sputtering desorption rate is proportional to ion density and plasma voltage and that these two parameters are maximum at the downstream end of the cathode.

It must also be noted how the time needed to remove $BaWO_4$ from the surface is longer than the one needed to remove Ba_3WO_6 mitigating the work function increase.

Looking at Figure 60 we can see how even when all the Ba_3WO_6 and $BaWO_4$ have been removed from the surface the work function is still below the bare tungsten value. This is due to the presence of barium oxide in the pores that contribute to the overall emission hence lowering the average work function value of the surface.

We can now analyze the evolution of the plasma voltage and ion/electron density with time. The values of the constants k_n and $k_{\Delta V}$ as defined in Eq. (112) are reported below.

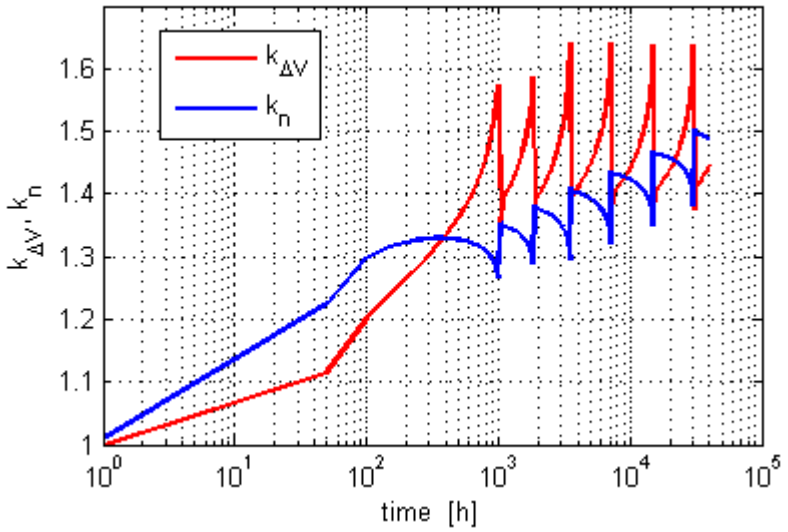

Figure 61 – k_n and $k_{\Delta V}$ trend with time – 12A

The periodic oscillations in the values of these constants are the effect of the hypotheses made in §4.5.3. In fact we have assumed the insert temperature profile to be constant with time whereas changes in the surface coverage will definitely affect its value. The insert temperature has been updated only when no solution to Eq. (13) and (18) can be found meaning that the thermionic emission from the surface is too low to reach the required discharge current. The update procedure consists in increasing the insert temperature value by steps of 10°C until a solution for Eq. (13) and (18) can be found.

In the real functioning of the cathode the insert temperature will vary gradually together with the plasma voltage and ion density. Forcing the temperature to increase only when the cathode has reached a critical condition (emitted current too low to reach the required discharge current as for example after 1000 hours in Figure 61) will produce an overestimation of the plasma voltage since the cathode, not being able to get enough current from the thermionic emission, will try to increase the ion current and to decrease the electron one to meet the required discharge current hence increasing both the value of ΔV and n.

When a critical condition is going to be reached the plasma voltage will increase and the plasma density will decrease reducing the value of the electron current so that the total discharge current can be obtained by the sum of I_{th} and I_i. This explains the behaviour of $k_{\Delta V}$ and k_n just before the "steps" in Figure 61.

When the critical condition is finally reached the insert temperature is suddenly increased increasing the thermionic emitted current hence allowing the cathode to reduce the plasma potential and to increase the particle density bringing them to a value close to the one they had before the critical condition was approached. This explains the trend of $k_{\Delta V}$ and k_n just after the "steps" in Figure 61.

Since the ion current is directly proportional to the plasma number density the electron current will be reduced mainly increasing the plasma voltage hence justifying the bigger variation in $k_{\Delta V}$ than in k_n as reported in the figure above.

Once the values of plasma voltage, particle density and work function are known the currents flowing at the cathode surface can be calculated.

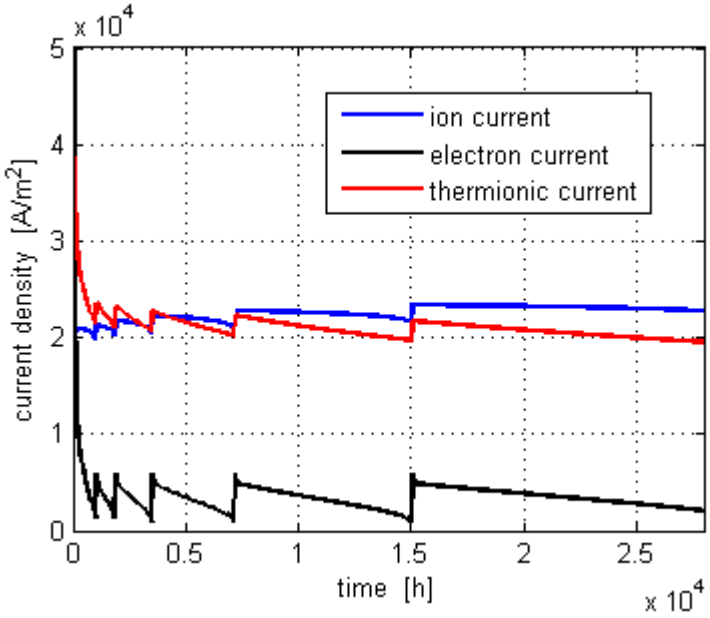

Figure 62 – Calculated currents to the cathode surface – 12A

As it can be noted in Figure 62, the current plot shows the same "steps" already noticed before. This is due to the fact the currents are calculated using the values reported in Figure 61.

In none of the long duration cathode life tests an increase of the hollow cathode operating voltage (anode voltage) has been measured whereas in Figure 61 the increase of the plasma voltage is clearly shown.

This can be explained noting that the anode voltage is the voltage "seen" by the power supply or, in other words, the voltage that the power supply needs to provide to maintain the required discharge current.

This voltage is clearly a function of the plasma voltage, of the ionic, thermionic and electron current at the cathode surface and of the processes taking place in the orifice

and in the cathode plume. Hence assuming that the contributions of these processes taking place on the cathode surface in the plasma and in the plume are independent we can write

$$V_{PowSupply} = V_{surface} + V_{orifice} + V_{plume} \tag{115}$$

For what concerns the processes taking place at the cathode surface we can write

$$V_{surface} = \frac{1}{I_D} \int_0^{L_c} \left[J_{th}(z) + J_i(z) - J_e(z)\right] \Delta V(z) 2\pi r_{int}\, dz \tag{116}$$

Since the power provided by the power supply relatively to the cathode surface must be equal to the electrical power relative to the ion, electron and thermionic current flow at the surface.

Applying Eq. (116) we can calculate $V_{surface}$

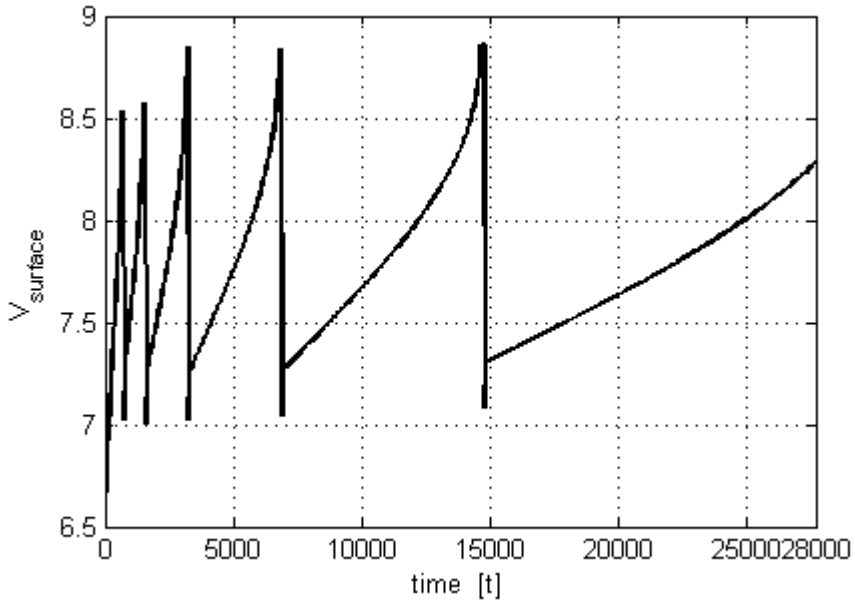

Figure 63 - $V_{surface}$ trend with time – 12A

As it can be seen in the figure above despite of the wide variation in $k_{\Delta V}$ the value of $V_{surface}$ oscillates around an average value that is more or less constant with time (~ 7.7 V) with variations of only ±1 V.

If this is compared to the experimentally recorded voltage (Figure 64) we can see how these oscillations, even if generated by the assumptions made to simplify the plasma parameter update procedure, have a value that is smaller than the real oscillation of the voltage and how, as expected, $V_{surface}$ is smaller than $V_{PowSupply}$ since the insert surface

voltage fall represents only a part of the total voltage fall between the cathode and the anode.

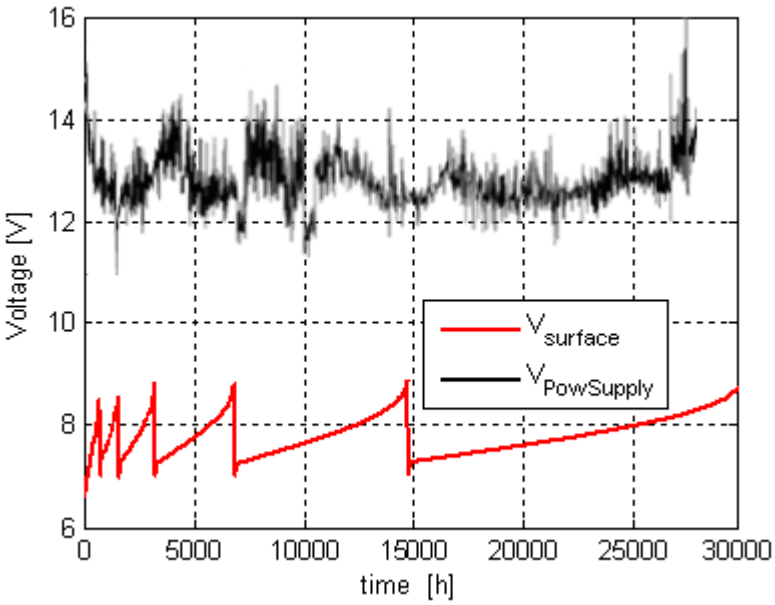

Figure 64 – Measured cathode voltages [22]

Noting what has been said above, noting that the average value of $V_{surface}$ is more or less constant with time and noting the comparison reported in Figure 56, we can conclude that the whole process used to update the plasma parameters gives reasonable results even when it is coupled with the surface coverage model.

From the data relative to the ion, electron and thermionic current densities we can calculate the value of the total current density and from it derive how the "active zone" of the cathode moves during life.

The total emission profiles along the insert length are showed below for different times

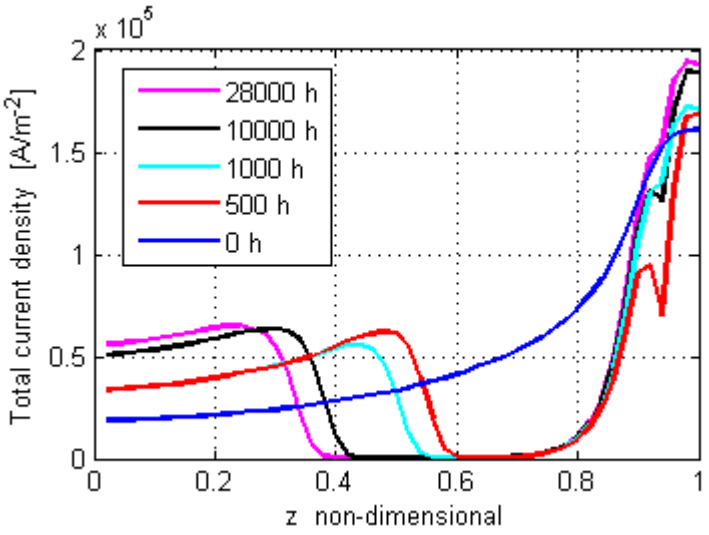

Figure 65 – Total emission profiles at different times – 12 A

As it can be seen at the beginning of life the total emission profile is smooth and gradually increasing from the upstream to the downstream end of the cathode. The "active zone" (the zone of highest emission) is then located at the downstream end.
As the cathode accumulates hours of operation the surface coverage changes due the depletion of low work function compounds starting from the downstream end of the insert. The active zone is then expected to move upstream.
Looking at Figure 65 we can see how the emission profiles presents two distinct peaks of comparable intensity. The first peak at the downstream end of the cathode is due to the ion flux from the plasma to the insert surface and tends to increase with time to balance the reduction in thermionic emission due to low work function depletion.
The second peak is located roughly at half the length of the cathode and is relative to the thermionic emission. This peak corresponds to the front of the low work function depletion and moves upstream with time following the depletion profiles shown in Figure 58 and Figure 60.
At the end of life the predicted emission zone is at 20% of the insert length from the upstream end of the cathode. Comparing this prediction with what has been derived by Sarver-Verhey in Ref. [22] we can note how the model predictions are very conservative.
This can be explained noting the many conservative assumptions made in the development of this model like neglecting the increase of temperature resistance of Ba_3WO_6 due to barium substitution by calcium and the assumption that the barium oxide evaporated from the insert will deposit only in the location close to where it has evaporated.

5.4.1.1 End of life criterion development

As shown before the surface coverage model and the plasma parameter update procedure produce results that are in agreement with the expectations and with the measured data.
Once the evolution of the surface coverage has been derived we can now develop an end of life criterion.
Commonly in hollow cathodes operation the end of life is assumed to occur when the cathode cannot be started within the power supply capabilities.

This means that the cathode is considered to be dead when the ignition voltage goes beyond the maximum voltage that can be produced by the power supply.

A detailed modelling of the ignition process from first principle will require a full three-dimensional electrical transient simulation of the hollow cathode. In the literature the development of such a model has never been tried hence the problem will be solved in a semi-empirical way.

The voltage needed to cause the break down discharge in the cathode can be assumed to be inversely proportional to the electron density inside the cathode and in the cathode – keeper region since the higher is the electron density the lower is the resistance between the electrodes.

Such electron density is certainly proportional to the emission from the cathode walls and hence from the thermionic emission.

$$\Delta V_{breakdown} \propto \frac{1}{n_e} \propto \frac{1}{J_{th}} \tag{117}$$

The thermionic emission at the ignition is proportional to the surface coverage that can be achieved at the end of the start up process.

If we assume that the start up phase begins at t_{start} and lasts for Δt_{start} seconds and that the insert is kept to a temperature T_{start} during the start-up phase the total barium oxide mass evaporated from the insert and the total mass needed to reach a full coverage are respectively

$$\begin{aligned} m_{BaO\,evap} &= \int_0^{\Delta t_{start}} \int_{S_{insert}} \dot{m}_{BaO}[T, \rho_{BaO}(t_{start})]\, dS\, dt \\ m_{BaO\,needed} &= [(1-\theta(t_{start}))\, S_{insert}\, (1-\Pi) + S_{OP}]\, \sigma_{BaO} \end{aligned} \tag{118}$$

where σ_{BaO} is the barium oxide density per unit area. If we assume that the start up time is 10 minutes and that the start up temperature is 1100 °C the trend of $m_{BaO\,evap}$ and $m_{BaO\,needed}$ with time is reported below.

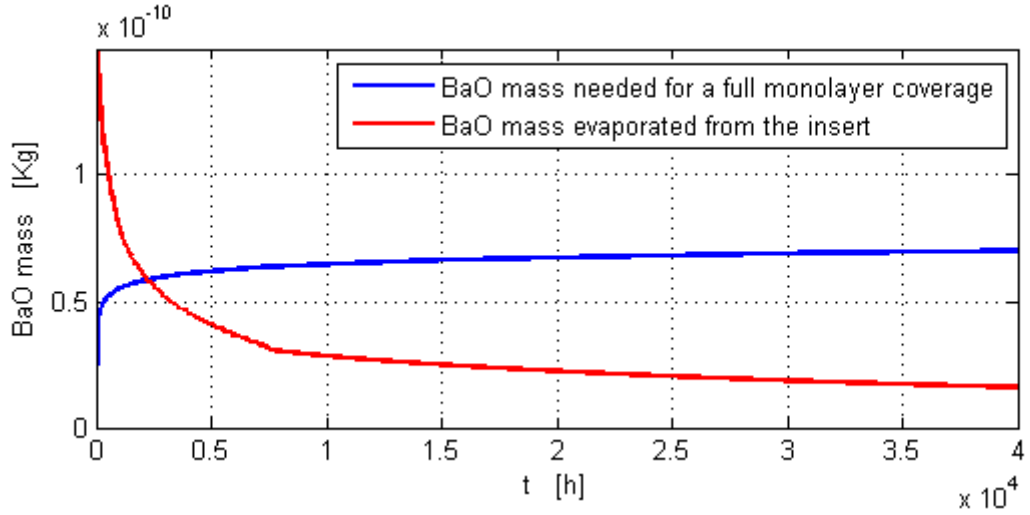

Figure 66 – BaO mass needed for a full coverage at start-up and evaporated mass during start-up T_{start}=1100 °C – 12A

Once the needed and deposited mass are known the average coverage can be calculated as

$$\theta_{startup} = \theta(t_{start}) + \frac{m_{BaO\ evap}}{m_{BaO\ needed}} \tag{119}$$

From this value of the coverage the average work function can be calculated and so the thermionically emitted current.

Since from Eq. (117) we only know that the voltage is proportional to $1/J_{th}$ we can define a voltage breakdown amplification factor as

$$\beta = \frac{V(t)}{V_0} = \frac{J_{th0}}{J_{th}(\theta)} \tag{120}$$

where V_0 is the breakdown voltage at the beginning of life, J_{th0} is the emission current relative to the temperature T_{start} and to a full surface low work function coverage.

The calculated trend of the amplification factor for the cathode tested by Saver- Verhey in Ref [22] is reported below

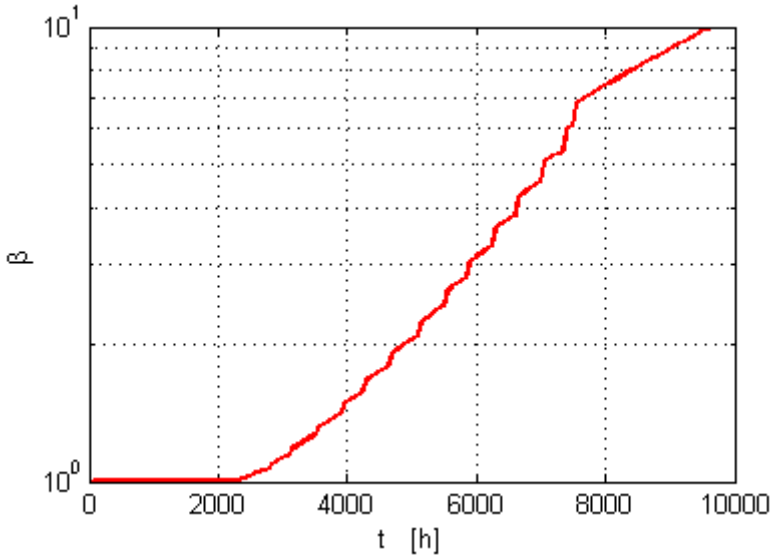

Figure 67 – Calculated voltage amplification factor – 12A

The experimental value of the amplification factor can be calculated form Figure 5

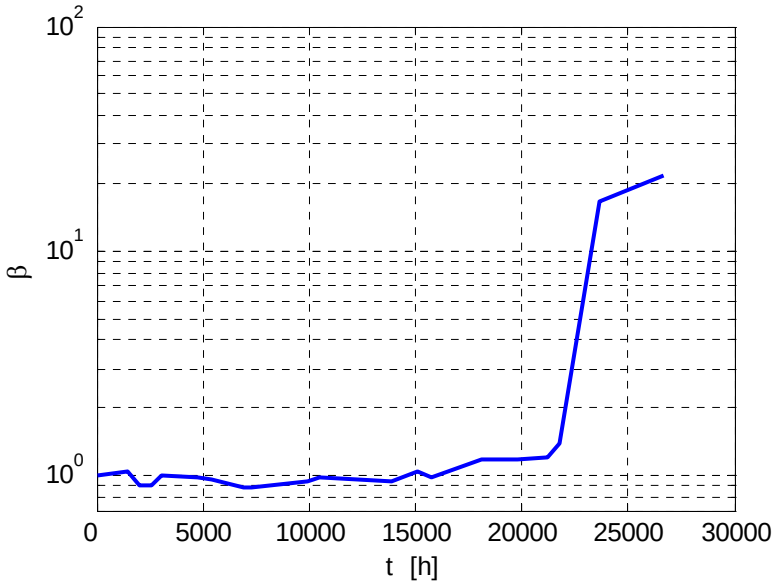

Figure 68 - Experimental voltage amplification factor [22]

Comparing the data in Figure 67 and Figure 68 it can seen how both the time values and the amplification values are out of scale. In spite of this the shape of the experimental and numerical β curves are similar showing a phase where the start up voltage stays constant (numerical 0-2,000 hours / experimental 0-21,000 hours) a phase of quick increase of the voltage (numerical 2,000-8,000 hours / experimental 22,000-24,000 hours) and then a phase of slower constant rate increase (numerical from 8,000 hours onwards / experimental 24,000 hours onwards).

The shift in the timescale can be explained noting that in the model a lot of conservative hypotheses have been made resulting in a voltage increase (cathode death) that for $T_{start} = 1100$ °C happens much before than in reality. The difference in the amplification values can be explained noting that Eq. (117) represents only a very easy interpretation of the relation between surface coverage and start up voltage.

The qualitative similarities found between these two trends could be interpreted as evidences of the goodness of the model stressing its conservative nature.

Comparing Figure 66 and Figure 67 we can note how the voltage increase happens when the evaporated barium oxide mass becomes less than the needed one hence and end of life criterion can be stated as:

"Given the temperature and the duration of the start up procedure the end of life of a cathode is reached when the barium oxide mass evaporated from the insert during the start up phase is not enough to provide a full coverage over all the internal cathode surfaces"

Using this criterion we will now change T_{start} until the calculated end of life of the cathode reported in Ref [22] matches the experimental value of 28,000 hours.

The experimental value is matched when the start up temperature is 1145 °C. We must note how this value is very close to the 1100 °C commonly used during the cathode start up process highlighting the extremely high sensitivity of the model to the initial start-up temperature.

The graph of the evaporated and needed mass relative to this condition is reported below

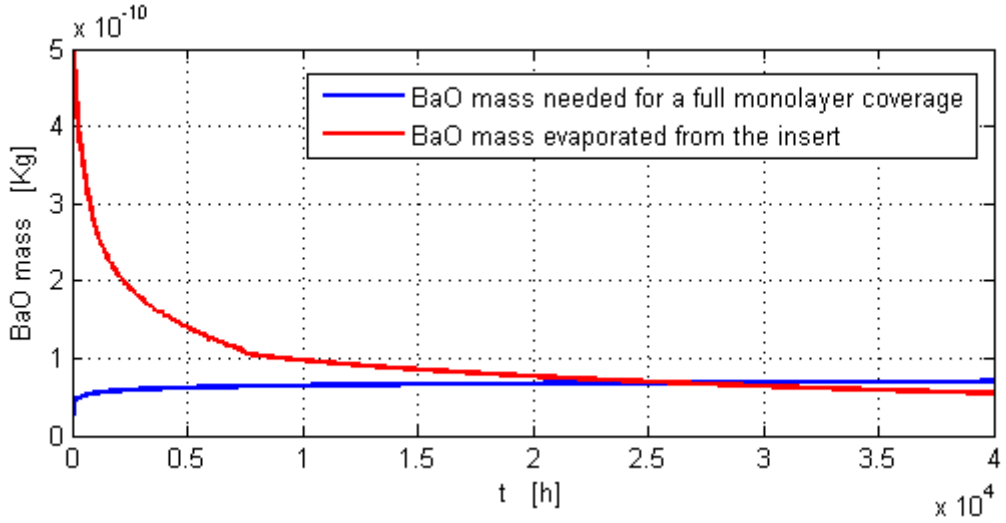

Figure 69 – BaO mass needed for a full coverage at start-up and evaporated mass during start-up T_{start}=1145 °C – 12A

Now that an end of life criterion has been developed and tuned with the data in Ref [22] the ELT discharge cathode will be simulated.

5.4.2 ELT discharge cathode surface coverage and lifetime simulation

The ELT discharge cathode has been simulated for the throttle levels TH0, TH8 and TH15 and then it has been simulated using the throttle level history relative to the Deep Space 1 flight spare ion engine test reported in Table 10 [2].
Below all the data relative to surface coverage, work function, and end of life are presented for every throttle setting.

5.4.2.1 TH0 – 4.9 A

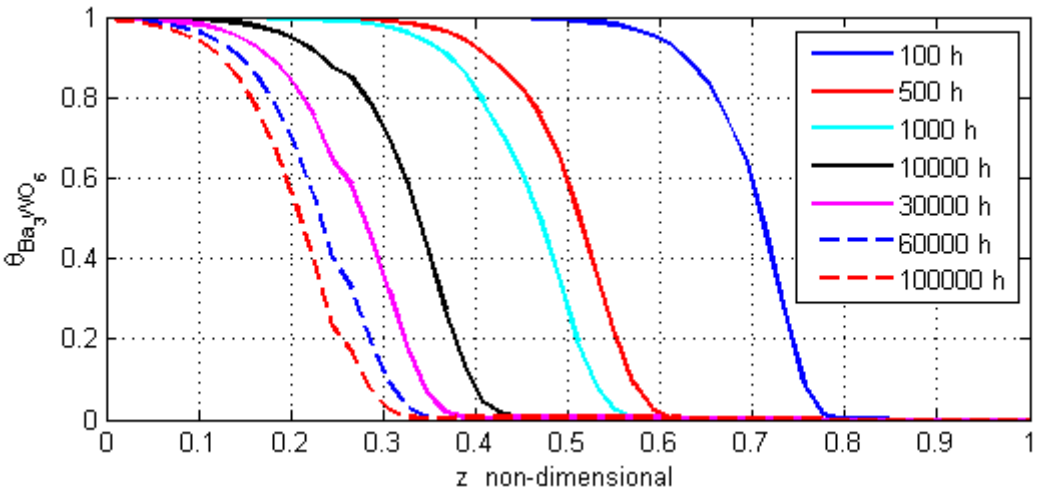

Figure 70 – Ba_3WO_6 surface coverage – TH0

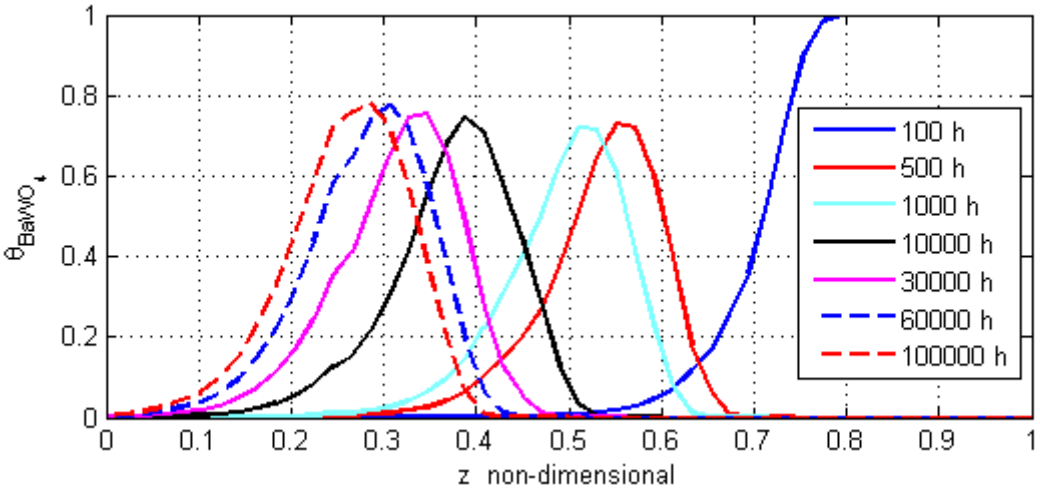

Figure 71 – $BaWO_4$ surface coverage – TH0

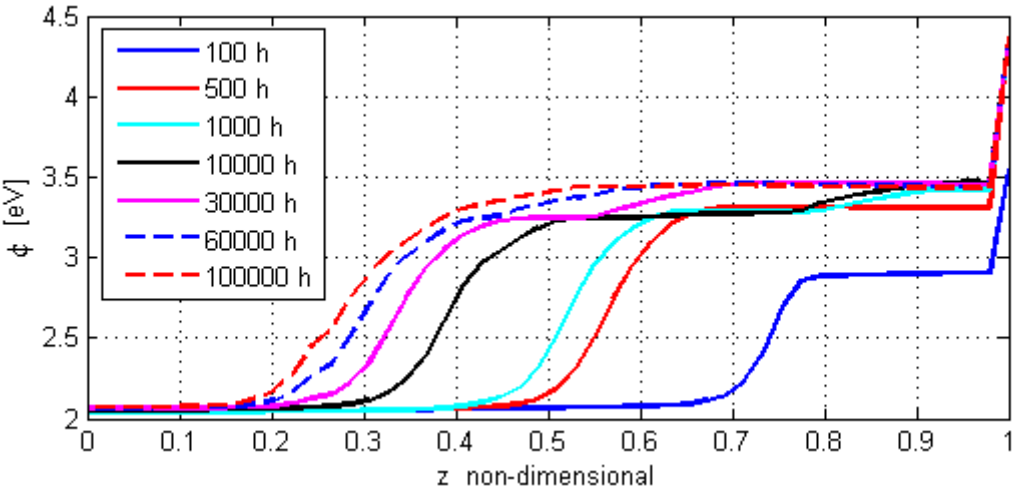

Figure 72 – surface work function – TH0

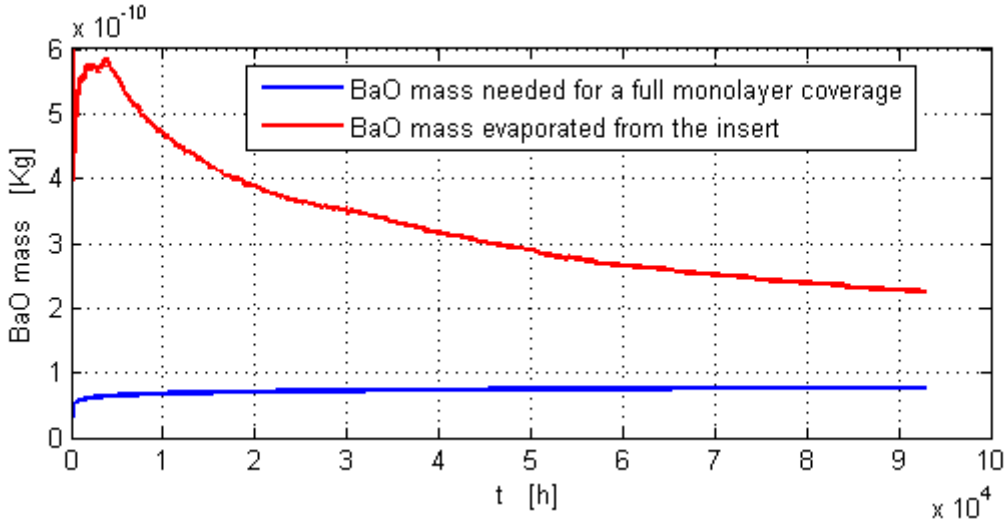

Figure 73 – BaO mass needed for a full coverage at start-up and evaporated mass during start-up T=1450 °C – TH0

All the comments made about the cathode tested in Ref [22] relatively to the low work function coverage and the work function evolution are still valid for the ELT cathode. Regarding the end of life a 100 thousands hours simulation shows that the cathode at TH0 is still far from the end of life. From an interpolation of the curves in Figure 73 the end of life can be estimated to occur after 200,000 hours.

5.4.2.2 TH8 – 7.6A

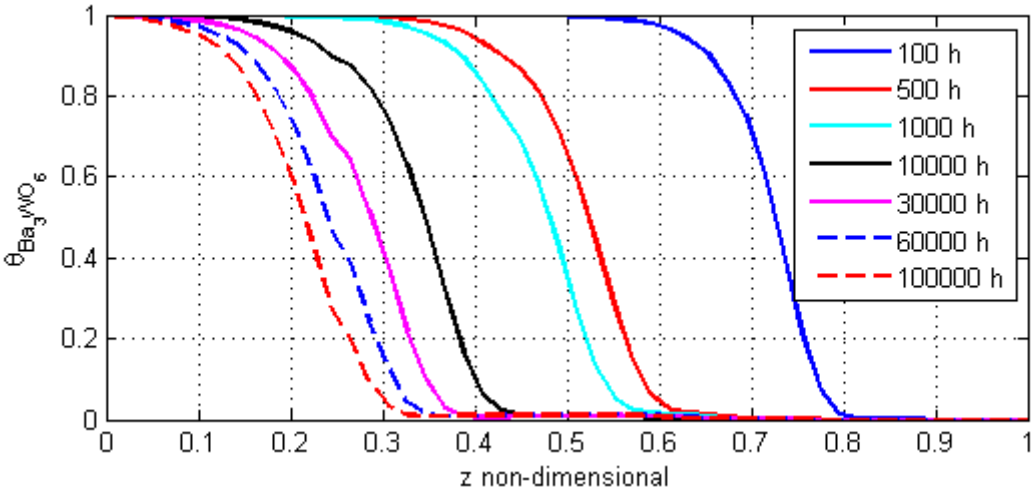

Figure 74 – Ba_3WO_6 surface coverage – TH8

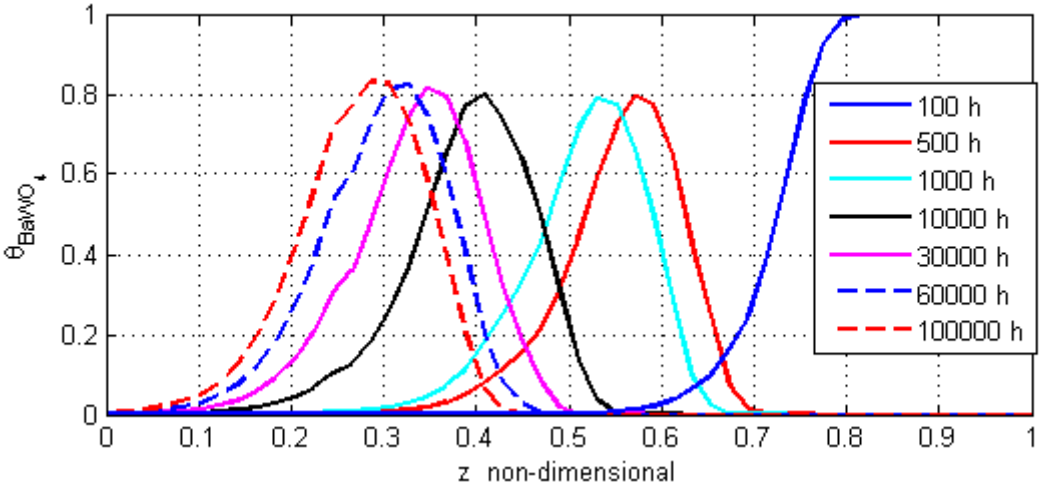

Figure 75 – $BaWO_4$ surface coverage – TH8

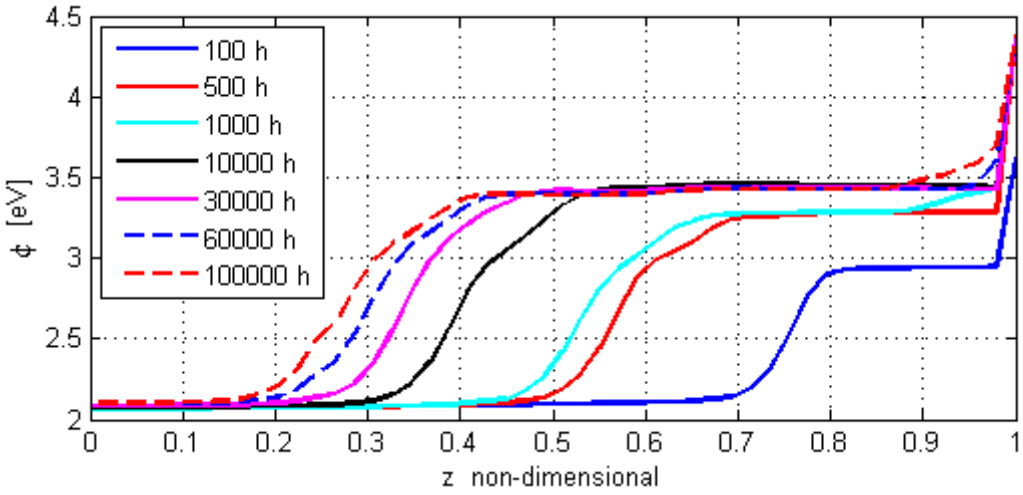

Figure 76 – surface work function – TH8

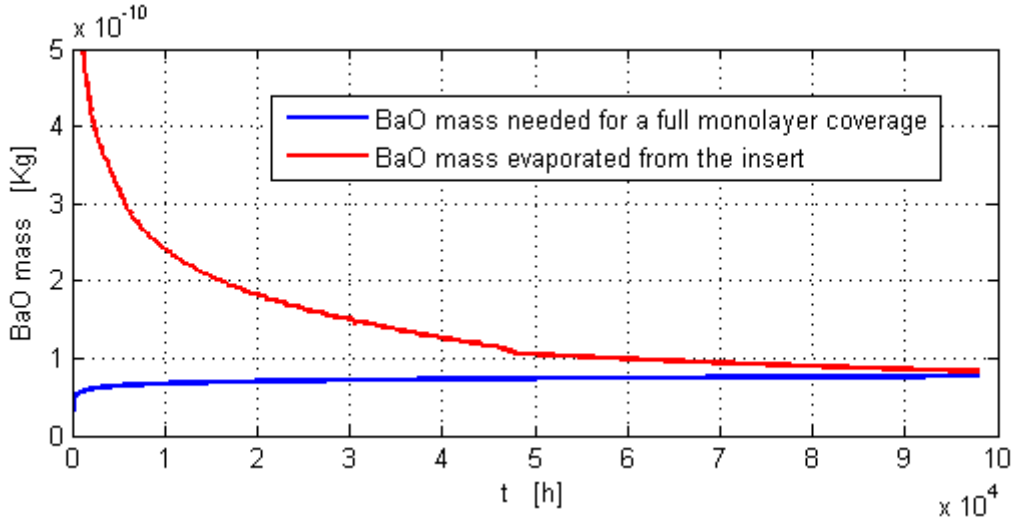

Figure 77 – BaO mass needed for a full coverage at start-up and evaporated mass during start-up T_{start}=1145 °C – TH8

The surface coverage and work function evolution are similar to the one reported for TH0 whereas the lifetime is shown to be 100,000 hours. The strong reduction in lifetime is not due to a higher low work function depletion (since the work function profiles in Figure 72 and Figure 76 and are quite similar and also the needed mass reported in Figure 73 and Figure 77 have similar values) but to a quicker ageing of the insert chemistry due to the fact that the insert temperature is higher at TH8 than at TH0 (Fig. 50).

5.4.2.3 TH15 – 13.5A

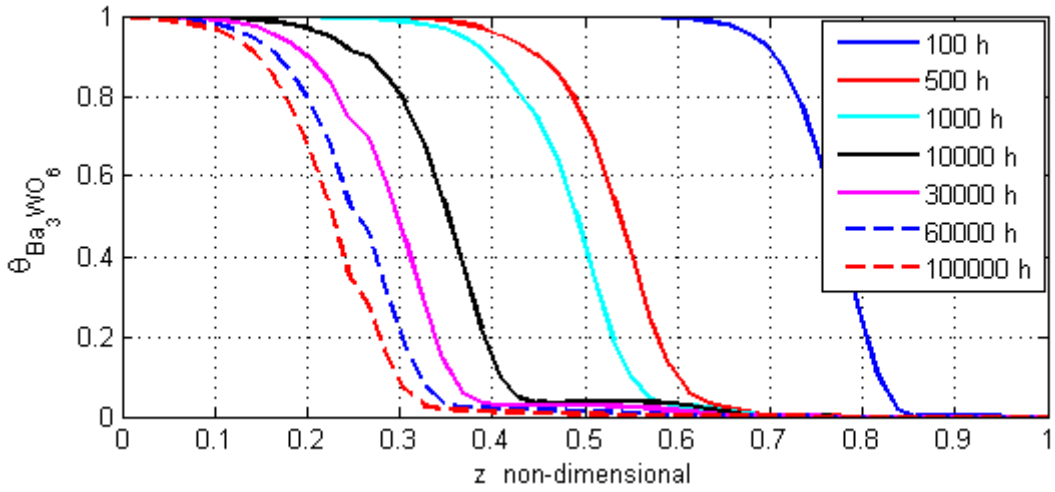

Figure 78 – Ba_3WO_6 surface coverage – 15

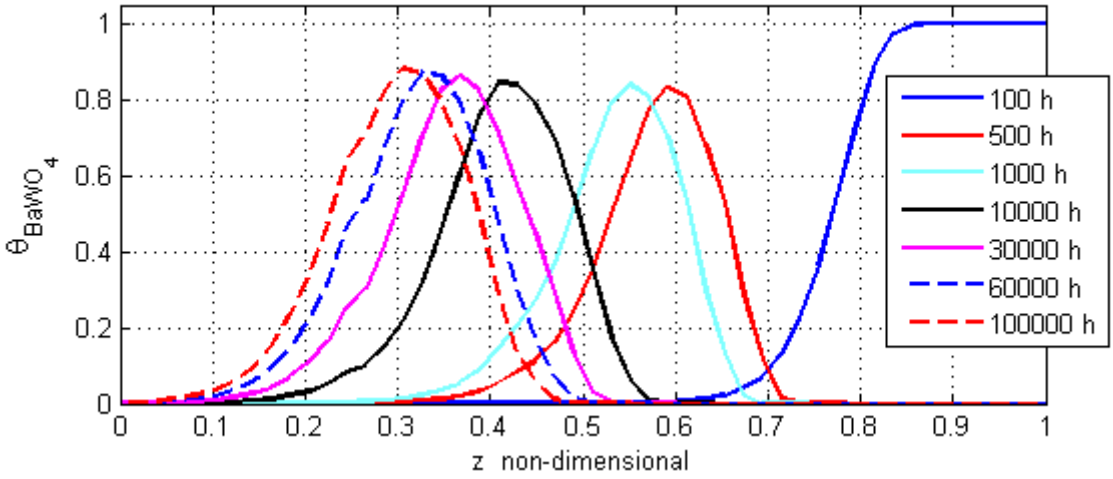

Figure 79 – $BaWO_4$ surface coverage – TH15

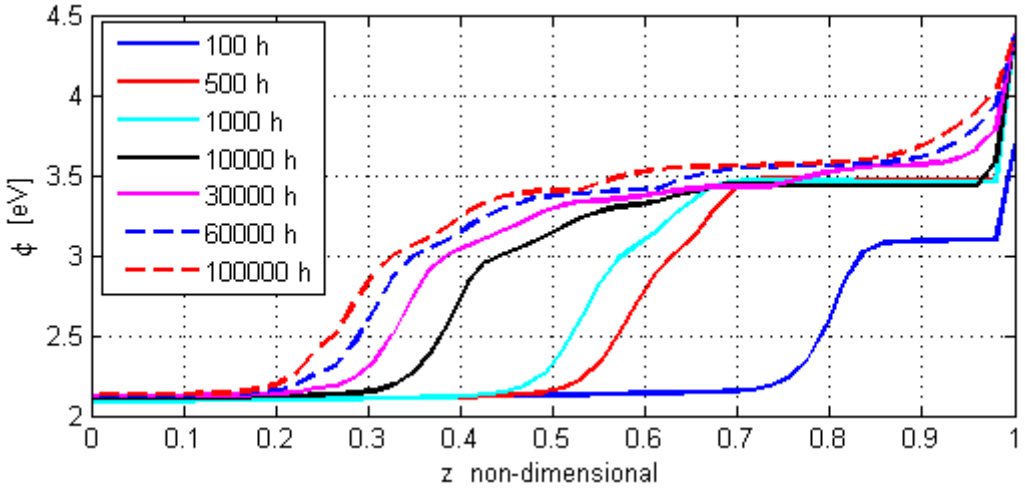

Figure 80 – surface work function – TH15

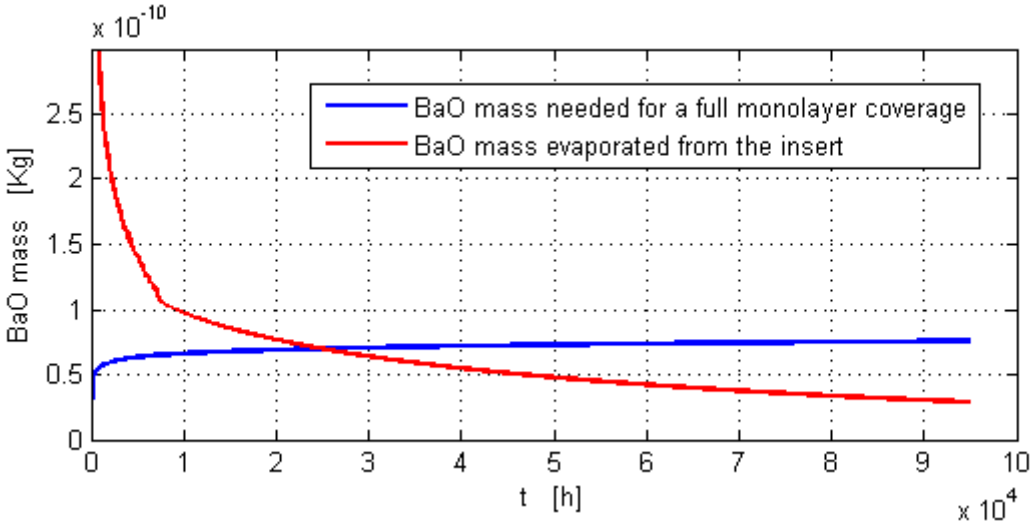

Figure 81 – BaO mass needed for a full coverage at start-up and evaporated mass during start-up T=1145 °C – TH15

For TH15 the low work function coverage and ϕ profiles are still similar to the ones relative to TH8 and TH0 although the relatively very high insert temperature causes a quicker aging of the insert chemistry making the evaporated barium oxide mass drop below the needed mass after 25,000 hours hence fixing to this value the life of the cathode. Such a low value could be expected since the operating conditions of the TH15 throttle level are close to the ones used in the lifetest reported in Ref [22] where the lifetime was 28,000 hours.

The similarities of the low work function coverage profile between this three throttle levels can be explained noting that even if at lower TH we have higher voltage drops and hence higher energy of the sputtering ions (Figure 56, Figure 57) the lower average insert temperature results in an higher activation energy (as could be seen from Eq. (89)) hence counterbalancing the increase in the sputtering energy; it must also be noted that a lower insert temperature means also a slower aging of the insert chemistry that on a very long time scale means higher local barium oxide concentrations and hence higher evaporation rates hence helping to balance the increase in the sputtering energy.

Regarding the hollow cathode lifetime a simple "rule of thumb" exists according to which the dispenser life doubled for every 30° to 40° reduction in the operating temperature of the insert. This rule is reported in Ref. [16], [18], [41] and has been derived from the analyses of a large volume of data regarding the life of cathodes dispensers for travelling wave tubes (TWT) devices.

This rule has never been tested with hollow cathodes for ion thrusters hence it will be tested with the data obtained numerically with the model.

The predicted lifetimes and the average temperatures relative to TH0, TH8 and TH15 are reported below

Table 13 – Lifetime and average insert temperatures for different THs

TH level	Average insert temperature [°C]	Predicted lifetime [h]	Δ_{Life}	ΔT
0	1045	200,000	1	0
8	1104	100,000	1/2	59
15	1169	25,000	1/8	124

To verify the statement reported above relatively to the lifetime trend with temperature we will now interpolate the data in Table 13 normalizing them relatively to TH0 and using an interpolating function of the kind

$$\Delta_{Life} = 2^{-\frac{\Delta T}{b}} \tag{121}$$

where Δ_{Life} is the lifetime amplification factor, ΔT is the temperature variation and b is the temperature increase needed to halve the cathode life.

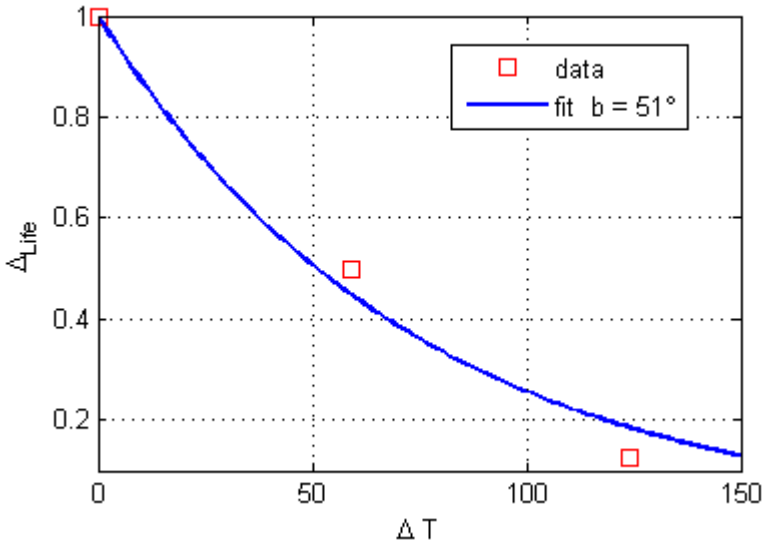

Figure 82 – Lifetime trend with temperature, computed data and interpolation

A mean least squares optimization return a value of $b = 51^o$ that, as it can be seen in Figure 82, produce a fit that well interpolates the data hence showing how the prediction of the model are in qualitative agreement with the expectation based on the analysis of a large amount of data relative to dispensers in TWTs, and showing how the life time is halved every 51 degrees of temperature increase.

As said before this rule of thumb is based on observation made on TWT devices and hence does not take into account the effects of ion bombardment, whereas it should reflect the effects of thermal desorption and deposition.

In this particular case the rule seems to be applicable (we can not make any definitive statement since only three points have been derived). This might be explained noting, as already said before, how, in this particular case, the surface coverage profiles are very similar for all the throttle levels given the counteracting effects of the insert temperature decrease and of the sheath voltage fall increase.

Since the surface coverage profiles are similar for all the THs the evaporation rate of barium oxide from the insert is the critical parameter for the lifetime definition. The behaviour of such evaporation is similar in hollow cathodes and in TWT devices hence allowing the application of the “rule of thumb” reported above.

This rule is instead most probably not applicable between different cathodes since the behaviour of the voltage drop and of the insert temperature profiles will be different (for example the lifetime of the T5 and T6 hollow cathodes cannot be determined extrapolating the data relative to NSTAR), and will not be applicable in cases where a variation of the discharge current produces variation of voltage and of the temperature that are too big or too small to reciprocally balance.

Now that the ELT cathode has been simulated at TH15, TH8 and TH0 we can move to its simulation using the throttle profile used in Ref [2] and reported in Table 10.

5.4.2.4 Discharge cathode from the Deep Space 1 spare ion engine 30000 hour life test

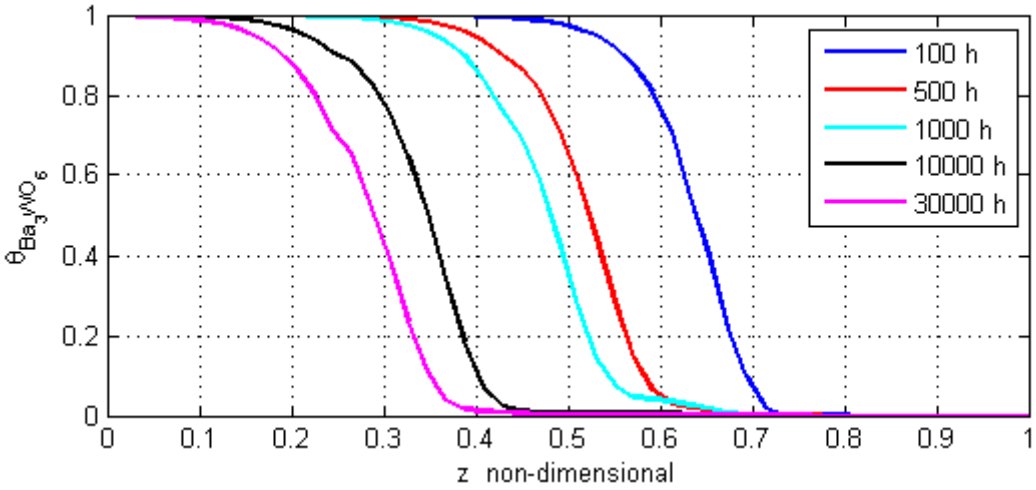

Figure 83 – Ba_3WO_6 surface coverage – NSTAR

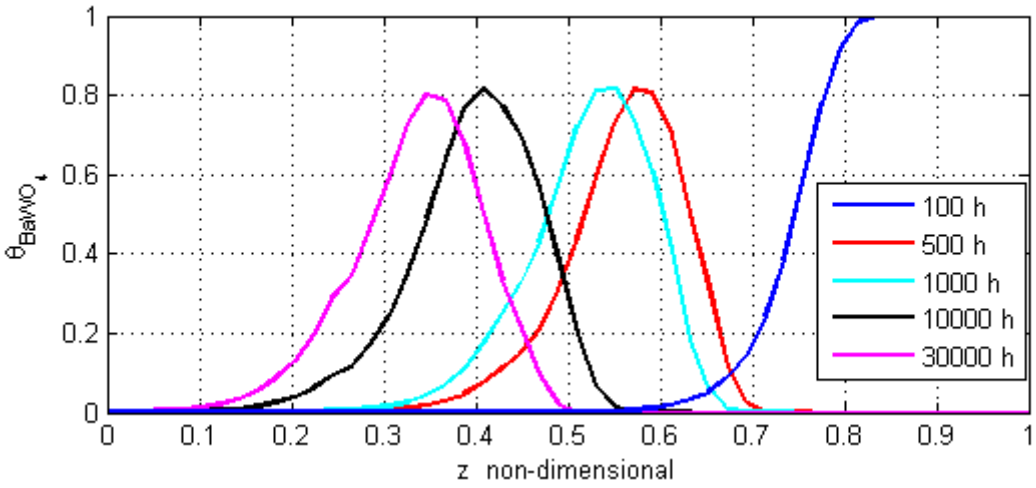

Figure 84 – $BaWO_4$ surface coverage – NSTAR

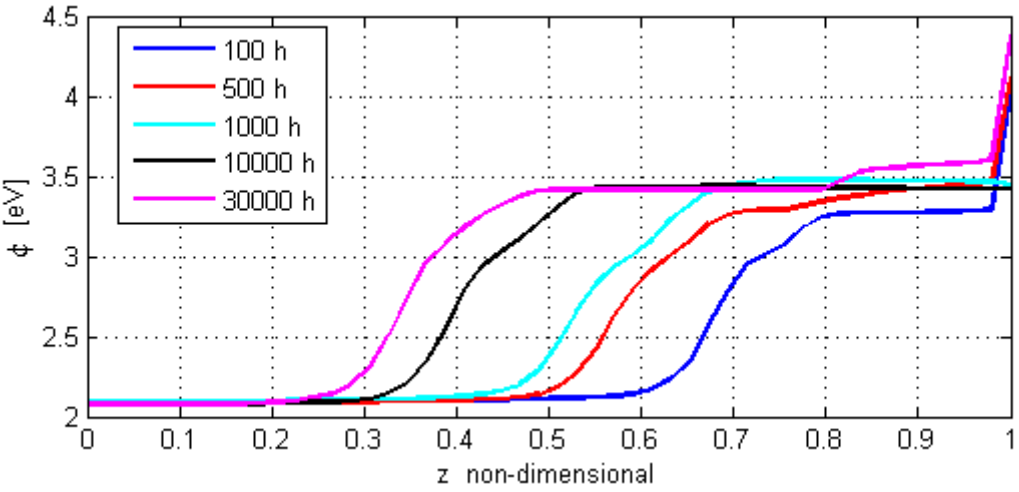

Figure 85 – Surface work function – NSTAR

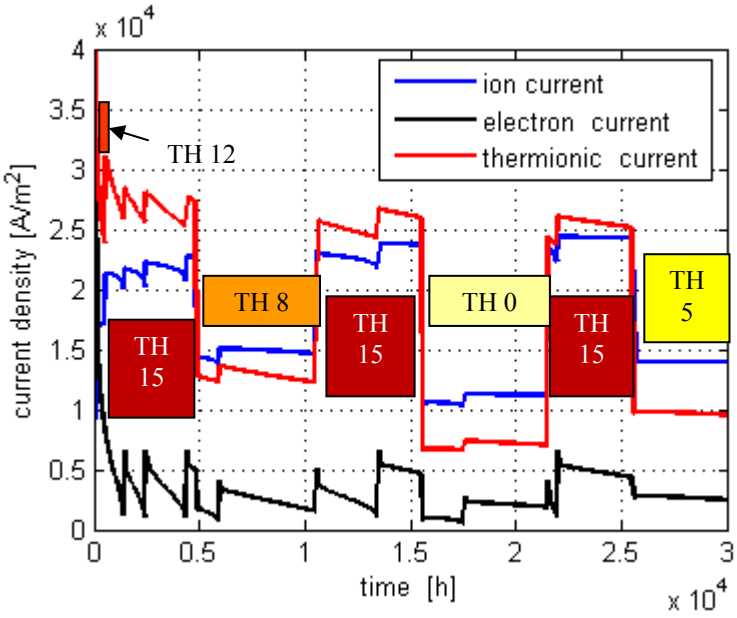

Figure 86 – Current densities to the cathode surface - NSTAR

Regarding the coverage and work function always the same comments are valid. In Figure 86 the current densities to the cathode surface are reported. In this figure we can note how when the cathode is run at TH15 the emitted current is higher than the ion one whereas for all the other throttle levels the contrary happens. This can be explained noting that TH15 is the TH level with the highest insert temperature hence with the highest thermionic emission.

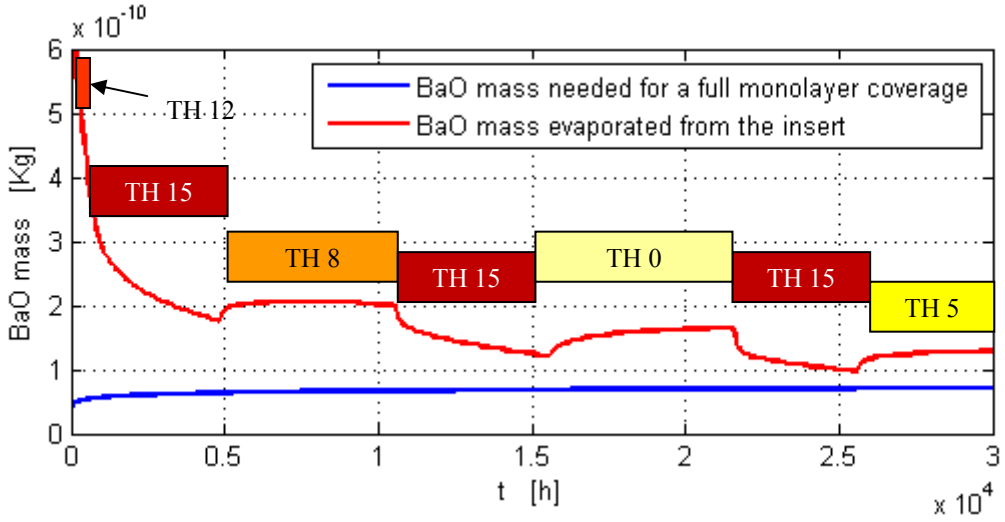

Figure 87 – BaO mass needed for a full coverage at start-up and evaporated mass during start-up T=1145 °C – NSTAR

Looking at Figure 87 we can note how after 30,000 hours the cathode has still not reached the end of life. This is in agreement with the real test of the cathode that has been voluntary stopped after 30,000 hours.

The estimation of the lifetime of the cathode depends on the throttle level the cathode will be run at from 30,000 hours onwards.

As it can be seen in Figure 87 during the time when the cathode is run at TH15 we have a net reduction of the evaporated mass whereas during the other TH levels we have even an increase in the evaporated mass.

This increase can be explained noting that the evaporation is proportional not only to the temperature but also to the local BaO concentration as demonstrated in §3.2.

When the cathode moves from TH15 to a lower throttle levels the insert temperature will decrease. A lower temperature means a lower evaporation rate hence a higher possibility that by diffusion the BaO depletion close to the surface can be replenished.

This at the beginning will result in a local increase in the BaO concentration that will lead to an higher evaporation rate explaining while at the beginning of TH8 (4,800h), TH5(15,500h) and TH0 (21,000h) the total deposited BaO mass increase with time.

After some time this higher evaporation rate will bring the system to an equilibrium between diffusion and evaporation (TH8 7,500 h) and then to a gradual reduction of the surface BaO density with a subsequent decrease in the evaporation rate (TH8 7,500-10,000 h).

It can be useful to estimate the lifetime of the cathode assuming that the operating conditions from 30,000 hours on will reflect those used until 30,000 hours. To do so the trends in Figure 87 have been extrapolated up to 100 thousands hours.

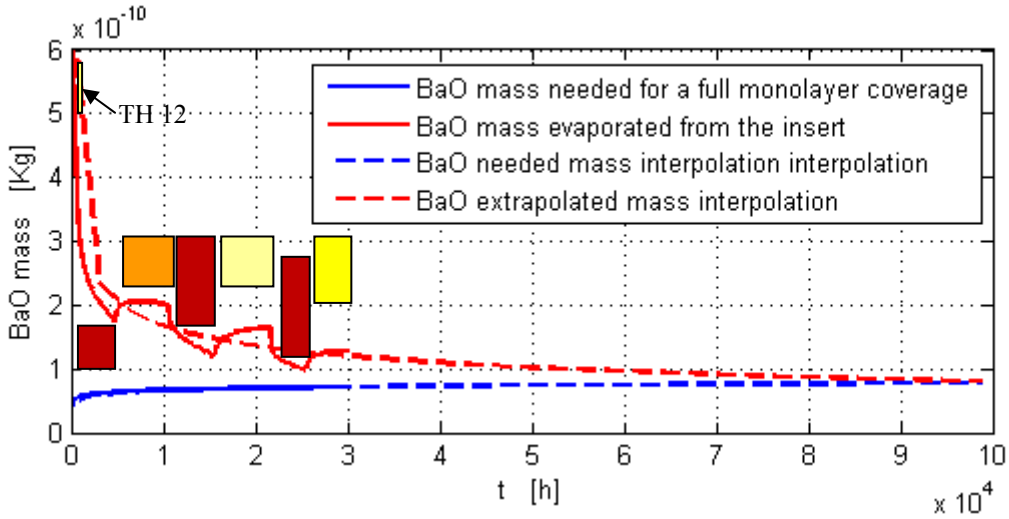

Figure 88 – Extrapolation of the deposited and needed BaO mass T=1145 – NSTAR

From this extrapolation a life time of 100 thousand hours can be predicted. The lifetime so predicted might seem too long considering that the lifetime at TH15 is only 25000 hours. This can be explained calculating the average discharge current of the cathode using the nominal current of each TH level weighted with the time that each TH level has been used for. The value so obtained is 7.98 A very close to the one of TH8 that is 7.6 A, this is in agreement with the fact that the lifetime predicted from Figure 88 is very close to the one relative to TH8.

The lifetime of 100,000 hours is then valid if the cathode is run at TH8 from 30,000 hours onward or if the throttle history reported in Table 10 is repeated for other 70,000 hours keeping the same ratio between the various throttle levels but using smaller time intervals so that the overall trend will get closer to the average one.

If the cathode is run at TH15 the lifetime is going to be around 35,000 hours whereas if the throttle level used is lower than TH8 the lifetime will be in excess of 100,000 hours.

5.5 Deposition model conclusion

In this chapter the results obtained with the model developed in §4 have been reported. This model is the first model that takes into account both ion bombardment and thermal low work function compounds desorption and that includes the effect that a surface

coverage reduction and the consequent work function increase has on the characteristics of the plasma inside the cathode cavity.

The process used to update the plasma characteristic has been validated using the data available in the literature finding a good agreement.

The cathode from Ref [22] and the one from the Deep Space 1 spare ion engine 30000 hours test [2] have been then simulated.

The simulation of the cathode in Ref [22] has shown how the low work function compounds coverage tends to decrease with time and how this decrease is followed by an increase in the plasma voltage. The effect of this increase has been analyzed and the reason why the predicted increase in the plasma voltage does not correspond to an increase of the voltage supplied by the power supply has been explained noting how the change in the current density distribution on the surface balance the voltage increase so that the current weighted mean voltage remains constant.

The evolution of the active area of the cathode has been studied. It has been shown that the downstream of the cathode is always a high current density area thanks to the high flux of ions reducing at this area of the surface whereas the peak due to thermionic emission tends to move upstream with time.

From the data obtained with the simulation of the cathode in [22] an end of life criterion has been derived and the model has been tuned to predict a lifetime of 28,000 hours fitting the experimental data for this cathode.

This end of life criterion has then been applied to the NASA ELT discharge cathode [2] relatively to the throttle levels TH0, TH8, TH15 and to the throttle profile used in the experimental analysis [2].

The results obtained show a lifetime of about 200,000 hours for TH0, 100,000 for TH8 and 25,000 for TH15. These data have been interpolated trying to verify the rule of thumb reported in [16], [18] finding a good agreement. The limit in the applicability of this rule has also being investigated and the cases where this can be used have been defined.

The simulation of the cathode with the throttle profile used during the experimental life test [2] shows a cathode life time in excess of 30,000 hours as observed in the experimental test reported in Ref [2].

The lifetime of the cathode is then relative to the throttle profile that will be used from 30,000 hours onwards; if TH8 (equivalent to the mean discharge current used up to 30,000 hours) is used the predicted lifetime is 100,000 hours whereas higher throttle

levels will provide shorter lifetimes (TH15 will provide a lifetime of about 35-40 thousand hours) and lower throttle levels longer lifetime (TH0 150-200 thousand hours).

Considering what have been said above we can conclude that the model developed in §4 gives results that are in agreement with the experimental evidence and with the theoretical expectations resulting to be, at present, the most comprehensive surface coverage model and the only one that, currently, includes a form of coupling between the surface changes and the plasma characteristics and that takes into account (even if indirectly through the results of the barium depletion chemical model) the complex chemistry of the impregnant.

6 Conclusions and future works

6.1 Conclusions

In this thesis a model for hollow cathode lifetime has been developed. This model has been divided in three parts: a barium oxide depletion model, a low work function surface coverage model and a plasma parameter update procedure; an end of life criterion has been added to these three parts.

The barium oxide depletion model has been derived from the knowledge of the BaO-CaO-Al_2O_3 ternary system diagram taking into account the BaO evaporation rate produced by every compound present on the pore surface.

It has been shown how the reduction of barium oxide evaporation to a single reaction (as done in some of the models present in the literature [10], [11], [13]-[15]) oversimplifies the problem overestimating the evaporation rate up to several orders of magnitude.

The motion of barium oxide inside the insert has been modelled using a single diffusion coefficient that has been derived from a sensitivity analysis made to match the model predictions to the experimental measurements reported in Ref [10].

As expected the values of the diffusion coefficient so obtained follow an Arrhenius trend with activation energy close to the one relative to BaO evaporation. These values are also found to be in qualitative agreement and of the same order of magnitude as those calculated with the theory developed by Jensen in Ref [11]. The discrepancy between the values obtained with the model and those obtained from the theory in [11] has been explained commenting the hypotheses made in the analytical derivation in Ref [11].

The data obtained from the depletion model have been compared with the experimental measurements performed on real cathode inserts by QinetiQ [41] and NASA JPL [2].

It has been shown how the model tends to produce results that get closer to the measurements the closer the imposed boundary conditions are to the real functioning of the cathode showing the goodness and the sensitivity of the model.

From the comparison with the experimental data both a qualitative (QinetiQ T5 and T6 cathode) and a quantitative agreement (NSTAR) has been found hence proving the goodness and the correctness of the model.

This depletion model is the first that takes into account both the complex chemistry of the $BaO\text{-}CaO\text{-}Al_2O_3$ system and the diffusion motion of barium oxide inside the insert; moreover this model is at present the only one able to fully simulate the 3D depletion of barium oxide from a cathode insert producing results that are in agreement with the measurements.

The surface coverage model has been derived from data found in the Russian literature [19]. From these data the main low work function compound has been identified.

The model reported in this thesis includes deposition, thermal desorption and ion sputtering desorption of the low work function compounds.

These processes have been analyzed and quantified and the most important desorption mechanism has been found to be ion sputtering hence is clear how the knowledge of the plasma characteristics is key in predicting the low work function surface coverage evolution.

The plasma will be affected by changes in the surface emission since a reduction in low work function coverage will result in a work function increase and in a subsequent reduction in thermionic emission reducing the electron input in the plasma column inside the cathode cavity.

To take into account this effect a semi empirical procedure to update the plasma parameters has been developed.

This procedure has been tested on the NASA NSTAR cathode producing results that are in good agreement with the measurements.

With the use of the coverage model together with the plasma parameter update procedure the evolution of the surface coverage and of the surface work function has been simulated.

The results so found are in qualitative agreement with the experimental data producing trends that match the theoretical expectation.

From the results obtained simulating the cathode tested in Ref [22] a simple way to calculate the trend of the breakdown voltage needed to initiate the cathode discharge with respect to time has been formulated. From this an end of life criterion has been developed. The criterion states that:

"Given the temperature and the duration of the start up procedure the end of life of a cathode is reached when the barium oxide mass evaporated from the insert during the start up phase is not enough to provide a full coverage over all the internal cathode surfaces"

Using this criterion the calculation of the breakdown voltage trend has been tuned to match the measured end of life of the cathode reported in [22]. It has been found that assuming the start up procedure to last for 10 minutes and the cathode insert to be at 1145 °C the lifetime predicted by the model matches the one measured experimentally.

The NSTAR cathode has then been simulated with the surface coverage model and its end of life has been determined at different throttle levels with the end of life criterion reported above.

For TH0 the computed lifetime is 200,000 hours whereas for TH8 and TH15 it is respectively 100,000 and 25,000 hours. These data regarding lifetime have been tested with the rule of thumb reported in Ref [16], [18], [41] according to which the lifetime of a cathode doubles every time the insert temperature is decrease by 40 °C. In this case the lifetime has been found to double every 51 degrees of temperature decrease. Since this rule has been derived from data relative to TWT devices its limits of applicability have been defined stating that it might be valid only to derive the lifetime of a cathode whose lifetime is already known at a different discharge current/insert temperature.

The NSTAR cathode has then been simulated for 30,000 hours using the throttle profile used during the long duration test reported in Ref [2].

The cathode has been found to be far from its end of life (as observed during the experimental campaign) and lifetime predictions have been formulated depending on the throttle level that will be used from 30,000 hours onwards.

Considering what has been said above the surface coverage model developed in this thesis results to be the most complete model of its kind being able to fully simulate the surface evolution and being the only model that, at present, is coupled with a model able to predict the changes in the hollow cathode plasma and with a barium oxide desorption model that takes into account both the $BaO\text{-}CaO\text{-}Al_2O_3$ system chemistry and barium oxide diffusion inside the insert.

The results obtained with the surface coverage model together with the chosen end of life criterion give lifetime predictions that are in agreement with previous observations and with the theoretical expectations confirming the goodness of the model.

In conclusion noting that the aim of this thesis was the development of a hollow cathode lifetime model we can state that this aim has been fully accomplished with the development of a model that given the insert temperature, the discharge current of the cathode and the plasma parameters of the cathode in nominal conditions is able to predict the barium oxide depletion in every point of the insert and the surface coverage

and work function in every location of the insert surface hence being able to predict the hollow cathode lifetime.

The data provided by the model, if not accurate, will definitely result to be conservative given the conservative character of every assumption made during the model development hence providing life time prediction that can be safely used to assess the suitability of a hollow cathode based electric propulsion subsystem for a long duration mission given its lifetime requirement.

6.2 Future works

The model reported in this thesis is complete and self consistent but to be used needs some input parameters that can be obtained only through experimental measurements.

These parameters are:

- the insert temperature distribution at the beginning of life needed to calculate BaO depletion from the insert.
- the plasma characteristics at the beginning of life (plasma particle density distribution, electron temperature distribution and voltage distribution) needed to calculate the desorption rates at the beginning of life and needed for the plasma parameters update procedure.

At present without these input parameters is impossible to use the model.

To avoid such limitation, in this section some possible improvements to the model will be proposed.

As pointed out several times in the thesis a plasma model is needed. With such a model the plasma characteristics could be calculated self-consistently at any time during the cathode lifetime simulation hence avoiding the need of a plasma parameter update procedure and the need of measuring the plasma parameters at the beginning of life.

Such a plasma model would be required to accept the geometry of the cathode, the insert temperature, the cathode mass flow rate and discharge current as input parameters and to produce as outputs the one-dimensional distribution along the cathode length of the plasma particle density, the voltage drop and of the ion and electron temperatures.

As pointed out in §2.2.2 at present in the literature only two the reliable and proven plasma models exist: the zero-dimensional model developed by Salhi and Turchi [7] and the full 3D model developed at JPL [5], [6], [35], [36].

The first model clearly does not fit our requirements whereas the second one is probably too complicated and, in addition to this, it is almost impossible to gain access to it due to ITAR regulations; hence a new plasma model must be developed.

Once such a model has been developed the knowledge of the insert temperature distribution is still needed.

To resolve this issue a thermal model of the cathode insert must be developed and coupled with the plasma model so that the insert temperature is calculated consistently with the plasma model solution.

If these two models (the plasma and the insert thermal model) will be added to the life-time model presented in this thesis, life time prediction could be carried out for any cathode whose geometry and current requirements are known hence constituting and extremely powerful design tool.

Appendix A

Numerical solution of the diffusion equation

Let's assume to have a diffusion equation in its typical form in a mono-dimensional domain

$$\frac{\partial u}{\partial t} = \frac{\partial^2 u}{\partial x^2} \tag{A122}$$

First of all the domain $D = [0,1] \times [0, \inf)$ will be discretized dividing [0,1] and [0,∞) with the points x_i and t_j

$$\begin{aligned} x_i &= i\Delta x \quad i = 0, 1, ...N \\ t_j &= j\Delta t \quad t = 0, 1, ...N \end{aligned} \tag{A123}$$

Where Δt and Δx are the temporal and spatial steps.

The partial derivatives will be approximated with forward finite differences in time and central finite differences in space

$$\begin{aligned} \frac{\partial^2 u_i^j}{\partial x^2} &= \frac{u_{i+1}^j - 2u_i^j + u_{i-1}^j}{\Delta x^2} \\ \frac{\partial u_i^j}{\partial t} &= \frac{u_i^{j+1} - u_i^j}{\Delta t} \end{aligned} \tag{A124}$$

Where u_i^j stands for the approximated value of the exact solution u calculated in x_i and t_j. Substituting Eq (A3) into Eq (A1) we obtain

$$\frac{u_{i+1}^j - 2u_i^j + u_{i-1}^j}{\Delta x^2} = \frac{u_i^{j+1} - u_i^j}{\Delta t} \tag{A125}$$

Introducing the parameter $\alpha = \dfrac{\Delta t}{\Delta x^2}$ and solving Eq (A1) for u_i^{j+1} we obtain

$$u_i^{j+1} = \alpha u_{i-1}^j + (1 - 2\alpha) u_i^j + \alpha u_{i+1}^j \tag{A126}$$

Defining the vectors U_j, V_j and the matrix A as follows

$$U_j = \left[u_1^j, u_2^j, ..., u_{N-1}^j\right]^T \qquad V_j = \left[u_0^j, 0, ..., 0, u_N^j\right]^T$$

$$A = \begin{bmatrix} 1-2\alpha & \alpha & & 0 \\ \alpha & \ddots & \ddots & \\ & \ddots & \ddots & \alpha \\ 0 & & \alpha & 1-2\alpha \end{bmatrix} \tag{A127}$$

We can switch to a more suitable matrix formulation of the numerical scheme

$$U_{j+1} = AU_j + \alpha V_j \tag{A128}$$

Assuming to have an initial perturbation E_0 on U_0, the perturbed U will be

$$\overset{...}{U}_0 = U_0 + E_0 \tag{A129}$$

This perturbation will propagate with the time integration

$$\overset{...}{U}_{j+1} = A\overset{...}{U}_0 + \alpha Vta_j \tag{A130}$$

The perturbation at the step $j+1$ is obtained subtracting Eq (A7) from Eq (A9)

$$E_{j+1} = AE_j = A^j saiE_0 \tag{A131}$$

Using the infinite or the one norm[†] we have

$$\|E_{j+1}\|_1 = \|E_{j+1}\|_\infty \leq \|A\|^j \|E_0\| \tag{A132}$$

A numerical scheme is *stable* if the norm of the error remains limited with $j \to \infty$ hence this scheme is stable if and only if $\|A\| \leq 1$.

$$\|A\|_1 = \|A\|_\infty = |\alpha| + |1 - 2\alpha| + |\alpha| \leq 1 \tag{A133}$$

Hence the system is stable if and only if $\alpha \leq 1/2s$.

The Lax Equivalence Theorem [54] states that a *consistent* finite difference approximation for a well-posed linear initial value problem is *convergent* if and only if it is *stable*.

The stability has been just demonstrated so now the consistency of the numerical scheme must be demonstrated.

A numerical scheme is defined consistent if reducing the steps to zero the numerical solution tends to the exact one. In formula

$$\lim_{\Delta x, \Delta t \to 0} L_R u - Lu = 0 \tag{A134}$$

Where L is the differential operator relative to the diffusion equation and L_R is the operator relative to the numerical scheme.

Considering how the derivatives have been approximated (Eq A3) and that u is the exact solution on the equation we have

---

[†] The one norm of a vector is defined as $\|v\|_1 = \sum_{k=1}^{N} |v_k|$.

The one norm of a matrix is defined as $\|A\|_1 = max\left(\|\text{column vector}\|_1\right)$

The infinite norm of a matrix is defined as $\|A\|_\infty = max\left(\|\text{row vector}\|_1\right)$

For the matrix A defined in Eq. (A6) the one and the infinite norm are equal because the matrix is symmetric

$$
\begin{gathered}
L_R = \frac{u_{i+1}^j - 2u_i^j + u_{i-1}^j}{\Delta x^2} - \frac{u_{i+1}^j - u_i^j}{\Delta t} = O(\Delta x^2 + \Delta t) \\
Lu = 0 \\
\lim_{\Delta x, \Delta t \to 0} L_R u - Lu = O(\Delta x^2 + \Delta t) \to 0
\end{gathered}
\tag{A135}
$$

The system is consistent and stable hence *the system converges if and only if* $\alpha \leq 1/2$.

Appendix B
Boundary conditions solution for the diffusion equation

B.1 1-D diffusion equation

Given a mono-dimensional diffusion equation

$$\frac{\partial \rho}{\partial t} = D_a \frac{\partial^2 \rho}{\partial x^2} \tag{B1}$$

if on the boundaries a mass flow rate condition is assigned this must equal the diffusion flux calculated on the boundary.

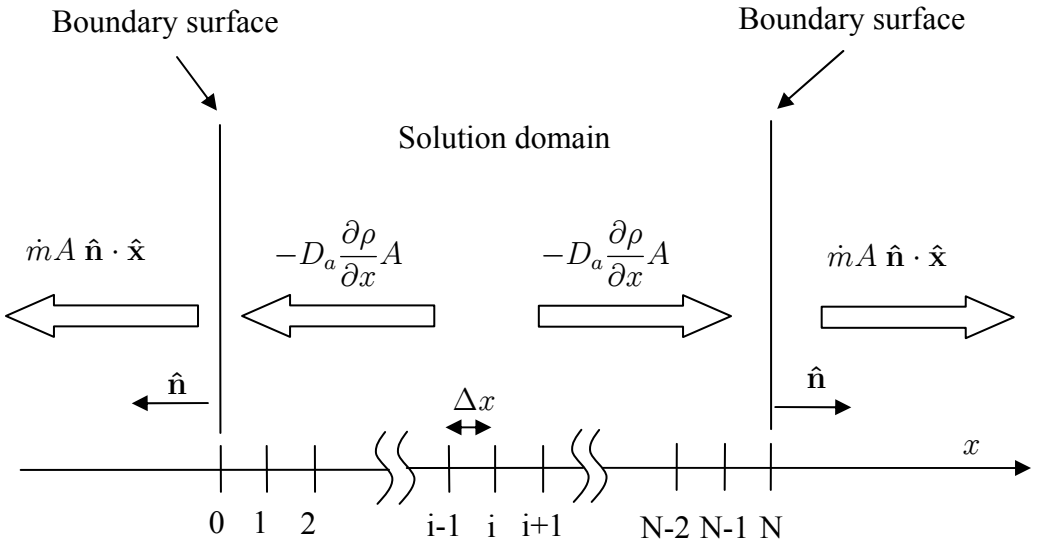

Figure B 1 – Boundary condition schematics

$$\begin{aligned} -D_a \frac{\partial \rho}{\partial x} A &= \dot{m} A \hat{\mathbf{n}} \cdot \hat{\mathbf{x}} \\ \frac{\partial \rho}{\partial x} &= -\frac{\dot{m}}{D_a} A \hat{\mathbf{n}} \cdot \hat{\mathbf{x}} \end{aligned} \tag{B2}$$

Where A is the area of the boundary surface and $\hat{\mathbf{n}}$ it's the outward normal unit vector. Moving to a non dimensional formulation to make the diffusion coefficient disappear and discretizing the spatial domain in N+1 point we have

$$\begin{aligned} \frac{\partial \widetilde{\rho}}{\partial \widetilde{t}} &= \frac{\partial^2 \widetilde{\rho}}{\partial \widetilde{x}^2} \\ \frac{\partial \widetilde{\rho}}{\partial \widetilde{x}} &= -\frac{\dot{m}}{D_a}\frac{d}{\widehat{\rho}}\,\hat{\mathbf{n}}\cdot\hat{\mathbf{x}} \end{aligned} \tag{B3}$$

Where *d* and $\widehat{\rho}$ are respectively the characteristic length and density.
For simplicity from now on we will put

$$b = -\frac{\dot{m}}{D_a}\frac{d}{\widehat{\rho}}\,\hat{\mathbf{n}}\cdot\hat{\mathbf{x}} \tag{B4}$$

and we will omit the ~ superscript assuming that all the variables are non-dimensional unless differently specified.
To solve the boundary condition the solution ρ will be expanded in a second order Taylor series where the diffusion equation and the boundary condition will be substituted.

B.1.1 Left hand boundary surface

For the left end boundary surface $i = 0$ so the Taylor series will be

$$\rho_1^t = \rho_0^t + \Delta x\frac{\partial \rho}{\partial x} + \frac{\Delta x^2}{2}\frac{\partial^2 \rho}{\partial x^2} + O(\Delta x^3) \tag{B5}$$

Substituting (B1), the boundary condition and Eq. (B4) we obtain

$$\rho_1^t = \rho_0^t + \Delta x b + \frac{\Delta x^2}{2}\frac{\partial \rho}{\partial t} + O(\Delta x^3) \tag{B6}$$

solving for ρ_0^{t+1}

$$\begin{aligned} \rho_1^t &= \rho_0^t + \Delta x b + \frac{\Delta x^2}{2}\frac{\rho_0^{t+1} - \rho_0^t}{\Delta t} \\ \rho_1^{t+1} &= \rho_0^t + 2\alpha(\rho_1^t - \rho_0^t) - 2\frac{\Delta t}{\Delta x}b \end{aligned} \tag{B7}$$

Substituting Eq (B4) and considering that on the left hand the normal $\hat{n}$ and $\hat{x}$ have opposite directions we obtain the final form of the boundary condition

$$\rho_0^{t+1} = \rho_0^t + 2\alpha(\rho_1^t - \rho_0^t) - \frac{\dot{m}(\rho_0^t)}{D_a}\frac{d}{\widehat{\rho}}\frac{2\Delta t}{\Delta x} \tag{B8}$$

Where $\dot{m}$ is the dimensional mass flow rate per unit area and D_a the dimensional diffusion coefficient.

B.1.2 Right hand boundary surface

For the right end boundary surface $i = N$ so the Taylor series is

$$\rho_{N-1}^t = \rho_N^t + \Delta x \frac{\partial \rho}{\partial x} + \frac{\Delta x^2}{2} \frac{\partial^2 \rho}{\partial x^2} + O(\Delta x^3) \tag{B9}$$

Following the same method used above and considering that on the right hand the normal $\hat{n}$ and $\hat{x}$ have the same direction we obtain the final form of the boundary condition

$$\rho_N^{t+1} = \rho_N^t + 2\alpha(\rho_{N-1}^t - \rho_N^t) - \frac{\dot{m}(\rho_N^t)}{D_a} \frac{d}{\widehat{\rho}} \frac{2\Delta t}{\Delta x} \tag{B10}$$

Where $\dot{m}$ is the dimensional mass flow rate per unit area and D_a the dimensional diffusion coefficient.

B.2 3-D diffusion equation

Given a three-dimensional diffusion equation with cylindrical symmetry

$$\frac{\partial \rho}{\partial t} - D_a \left(\frac{1}{r} \frac{\partial \rho}{\partial r} + \frac{\partial^2 \rho}{\partial r^2} + \frac{\partial^2 \rho}{\partial z^2} \right) - \frac{\partial \rho}{\partial z} \frac{\partial D_a}{\partial z} = 0 \tag{B11}$$

Assuming that the diffusion coefficient is a function of both r and z moving to a non dimensional formulation choosing the characteristic value of D_a as

$$\widehat{D}_a = max(D_a(r, z)) \tag{B12}$$

The system becomes

$$\frac{\partial \widetilde{\rho}}{\partial \widetilde{t}} - \widetilde{D}_a \left(\frac{1}{r} \frac{\partial \widetilde{\rho}}{\partial \widetilde{r}} + \frac{\partial^2 \widetilde{\rho}}{\partial \widetilde{r}^2} + \frac{\partial^2 \widetilde{\rho}}{\partial \widetilde{z}^2} \right) - \frac{\partial \widetilde{\rho}}{\partial \widetilde{z}} \frac{\partial \widetilde{D}_a}{\partial \widetilde{z}} = 0 \tag{B13}$$

where

$$\widetilde{D}_a = \frac{D_a}{\widehat{D}_a} \tag{B14}$$

And given a domain like the one in Figure 21 the boundary conditions on the inner and outer diameter surface can be expressed as

$$\frac{\partial \widetilde{\rho}}{\partial \widetilde{r}} = -\frac{\dot{m}}{D_a}\frac{d}{\widehat{\rho}}\left(\hat{\mathbf{n}}\cdot\hat{\mathbf{r}}\right) \tag{B15}$$

While for the upstream and orifice plate surface we have

$$\frac{\partial \widetilde{\rho}}{\partial \widetilde{z}} = -\frac{\dot{m}}{D_a}\frac{d}{\widehat{\rho}}\left(\hat{\mathbf{n}}\cdot\hat{\mathbf{z}}\right) \tag{B16}$$

B.2.1 Inner diameter surface

Neglecting now the ~ superscript since all the quantity are now non-dimensional, expanding the solution to a second order Taylor series and substituting Eq (B13) we have

$$\begin{aligned}\rho_{i,1}^{t} = \rho_{i,0}^{t} + \Delta x\frac{\partial \rho}{\partial r} + \frac{\Delta x^2}{2}\left[\frac{1}{D_a}\left(\frac{\partial \rho}{\partial t} - \frac{\partial \rho}{\partial z}\frac{\partial D_a}{\partial z}\right) - \right. \\ \left. - \left(\frac{1}{r_{int}}\frac{\partial \rho}{\partial r} + \frac{\partial^2 \rho}{\partial z^2}\right)\right] + O(\Delta x^3)\end{aligned} \tag{B17}$$

Substituting the derivatives with the finite differences Eq (A124)

$$\begin{aligned}\rho_{i,1}^{t} = \rho_{i,0}^{t} + \Delta x\frac{\partial \rho}{\partial r} + \frac{\Delta x^2}{2}\left[\frac{1}{D_a}\left(\frac{\rho_{i,0}^{t+1} - \rho_{i,0}^{t}}{\Delta t} - \right.\right. \\ \left.\left. - \frac{\rho_{i+1,0}^{t} - \rho_{i-1,0}^{t}}{2\Delta x}\frac{D_{a_{i+1,0}} - D_{a_{i-1,0}}}{2\Delta x}\right) - \left(\frac{1}{r_{int}}\frac{\partial \rho}{\partial r} + \frac{\rho_{i+1,0}^{t} - 2\rho_{i1,0}^{t} + \rho_{i-1,0}^{t}}{\Delta x^2}\right)\right]\end{aligned} \tag{B18}$$

Substituting Eq (B15) and solving for $\rho_{i,0}^{t+1}$ considering that on this surface $\hat{\mathbf{n}}$ and $\hat{\mathbf{r}}$ have opposite directions

$$\begin{aligned}\rho_{i,0}^{t+1} = & \rho_{i,0}^{t} + D_{a\,i,0}\left[2\alpha\left(\rho_{i,1}^{t} - \rho_{i,0}^{t} - \Delta x\frac{\dot{m}}{D_{a_{dim}i,0}}\frac{d}{\hat{\rho}}\right) + \right. \\ & + \alpha\left(\rho_{i+1,0}^{t} - 2\rho_{i,0}^{t} + \rho_{j-1,0}^{t}\right) + + \left.\frac{\Delta t}{r_{int}}\frac{\dot{m}}{D_{a_{dim}i,0}}\frac{d}{\hat{\rho}}\right] + \\ & + \alpha\frac{\rho_{i+1,0}^{t} - \rho_{i-1,0}^{t}}{2}\frac{D_{a\,i+1,0} - D_{a\,i-1,0}}{2}\end{aligned} \tag{B19}$$

B.2.2 Outer diameter surface

Expanding the solution to a second order Taylor series and substituting Eq (B13) we have

$$\rho_{i,N-1}^{t} = \rho_{i,N}^{t} - \Delta x \frac{\partial \rho}{\partial r} + \frac{\Delta x^2}{2}\left[\frac{1}{D_a}\left(\frac{\partial \rho}{\partial t} - \frac{\partial \rho}{\partial z}\frac{\partial D_a}{\partial z}\right) - \right. \\ \left. - \left(\frac{1}{r_{int}}\frac{\partial \rho}{\partial r} + \frac{\partial^2 \rho}{\partial z^2}\right)\right] + O(\Delta x^3) \tag{B20}$$

Following the same method used above and considering that on this surface $\hat{\mathbf{n}}$ and $\hat{\mathbf{r}}$ have the same direction

$$\rho_{i,N}^{t+1} = \rho_{i,N}^{t} + D_{a\,i,N}\left[2\alpha\left(\rho_{i,N-1}^{t} - \rho_{i,N}^{t} - \Delta x \frac{\dot{m}}{D_{a_{dim}i,N}}\frac{d}{\hat{\rho}}\right) + \right. \\ + \alpha\left(\rho_{i+1,N}^{t} - 2\rho_{i,N}^{t} + \rho_{j-1,N}^{t}\right) - - \left.\frac{\Delta t}{r_{int}}\frac{\dot{m}}{D_{a_{dim}i,N}}\frac{d}{\hat{\rho}}\right] + \\ + \alpha\frac{\rho_{i+1,N}^{t} - \rho_{i-1,N}^{t}}{2}\frac{D_{a\,i+1,N} - D_{a\,i-1,N}}{2} \tag{B21}$$

B.2.3 Upstream Surface

Expanding the solution to a second order Taylor series and substituting Eq (B13) we have

$$\rho_{1,j}^{t} = \rho_{0,j}^{t} + \Delta x \frac{\partial \rho}{\partial z} + \frac{\Delta x^2}{2}\left[\frac{1}{D_a}\left(\frac{\partial \rho}{\partial t} - \frac{\partial \rho}{\partial z}\frac{\partial D_a}{\partial z}\right) - \right. \\ \left. - \left(\frac{1}{r_{int}}\frac{\partial \rho}{\partial r} + \frac{\partial^2 \rho}{\partial r^2}\right)\right] + O(\Delta x^3) \tag{B22}$$

Substituting Eq (A124)

$$\rho_{0,j}^{t+1} = \rho_{0,j}^{t} + D_{a0,j}\left[2\alpha\left(\rho_{1,j}^{t} - \rho_{0,j}^{t} - \Delta x \frac{\dot{m}}{D_{a_{dim}0,j}}\frac{d}{\hat{\rho}}\right) + \right. \\ + \alpha\left(\rho_{0,j+1}^{t} - 2\rho_{0,j}^{t} + \rho_{0,j-1}^{t}\right) + + \left.\frac{\Delta t}{2r_j\Delta x}\left(\rho_{0,j+1}^{t} - \rho_{0,j-1}^{t}\right)\right] + \\ + \Delta t\frac{D_{a1,j} - D_{a0,j}}{\Delta x}\frac{\dot{m}}{D_{a_{dim}0,j}}\frac{d}{\hat{\rho}} \tag{B23}$$

substituting Eq (B16) and solving for $\rho_{i,0}^{t+1}$ considering that on this surface $\hat{\mathbf{n}}$ and $\hat{\mathbf{r}}$ have opposite directions

$$\rho_{0,j}^{t+1} = \rho_{0,j}^{t} + D_{a0,j}\left[2\alpha\left(\rho_{1,j}^{t} - \rho_{0,j}^{t} - \Delta x \frac{\dot{m}}{D_{a_{dim}0,j}}\frac{d}{\hat{\rho}}\right) + \right. \\ + \alpha\left(\rho_{0,j+1}^{t} - 2\rho_{0,j}^{t} + \rho_{0,j-1}^{t}\right) + + \left.\frac{\Delta t}{2r_j\Delta x}\left(\rho_{0,j+1}^{t} - \rho_{0,j-1}^{t}\right)\right] + \\ + \Delta t\frac{D_{a1,j} - D_{a0,j}}{\Delta x}\frac{\dot{m}}{D_{a_{dim}0,j}}\frac{d}{\hat{\rho}} \tag{B24}$$

B.2.4 Orifice plate surface

Expanding the solution to a second order Taylor series and substituting Eq (B13) we have

$$\rho_{M-1,j}^{t} = \rho_{M,j}^{t} - \Delta x \frac{\partial \rho}{\partial z} + \frac{\Delta x^2}{2}\left[\frac{1}{D_a}\left(\frac{\partial \rho}{\partial t} - \frac{\partial \rho}{\partial z}\frac{\partial D_a}{\partial z}\right) - \right. \\ \left. - \left(\frac{1}{r_{int}}\frac{\partial \rho}{\partial r} + \frac{\partial^2 \rho}{\partial r^2}\right)\right] + O(\Delta x^3) \tag{B25}$$

Following the same method used above and considering that on this surface $\hat{n}$ and $\hat{z}$ have the same direction

$$\rho_{M,j}^{t+1} = \rho_{M,j}^{t} + D_{aM,j}\left[2\alpha\left(\rho_{M-1,j}^{t} - \rho_{M,j}^{t} - \Delta x \frac{\dot{m}}{D_{a_{dim}M,j}}\frac{d}{\hat{\rho}}\right) + \right. \\ + \alpha\left(\rho_{M,j+1}^{t} - 2\rho_{M,j}^{t} + \rho_{M,j-1}^{t}\right) + \\ \left. + \frac{\Delta t}{2r_j \Delta x}\left(\rho_{M,j+1}^{t} - \rho_{M,j-1}^{t}\right)\right] - \Delta t \frac{D_{aM,j} - D_{aM-1,j}}{\Delta x}\frac{\dot{m}}{D_{a_{dim}M,j}}\frac{d}{\hat{\rho}} \tag{B26}$$

B.2.5 Corner 1

Expanding the solution to a second order Taylor series and substituting Eq (B13) we have

$$\rho_{1,1}^{t} = \rho_{0,0}^{t} + \Delta x\left(\frac{\partial \rho}{\partial z} + \frac{\partial \rho}{\partial r}\right) + \frac{\Delta x^2}{2}\left[\frac{1}{D_a}\left(\frac{\partial \rho}{\partial t} - \frac{\partial \rho}{\partial z}\frac{\partial D_a}{\partial z}\right) - \right. \\ \left. - \left(\frac{1}{r_{int}}\frac{\partial \rho}{\partial r}\right)\right] + O(\Delta x^3) \tag{B27}$$

Using always the same method and noting that both $\hat{\mathbf{z}}$ and $\hat{\mathbf{r}}$ direction are opposite to $\hat{\mathbf{n}}$

$$\rho_{0,0}^{t+1} = \rho_{0,0}^{t} + D_{a\,0,0}\left[2\alpha\left(\rho_{1,1}^{t} - \rho_{0,0}^{t} - \Delta x \frac{\dot{m}}{D_{a_{dim}0,0}}\frac{d}{\hat{\rho}}\right) + \right. \\ \left. + \frac{\Delta t}{r_{int}}\frac{\dot{m}}{D_{a_{dim}0,0}}\frac{d}{\hat{\rho}}\right] + \Delta t \frac{D_{a\,1,0} - D_{a\,0,0}}{2}\frac{\dot{m}}{D_{a_{dim}0,0}}\frac{d}{\hat{\rho}} \tag{B28}$$

B.2.6 Corner 2

Expanding the solution to a second order Taylor series and substituting Eq (B13) we have

$$\rho^{t}_{M-1,1} = \rho^{t}_{M,0} + \Delta x \left(\frac{\partial \rho}{\partial r} - \frac{\partial \rho}{\partial z}\right) + \frac{\Delta x^2}{2}\left[\frac{1}{D_a}\left(\frac{\partial \rho}{\partial t} - \frac{\partial \rho}{\partial z}\frac{\partial D_a}{\partial z}\right) - \right. \\ \left. - \left(\frac{1}{r_{int}}\frac{\partial \rho}{\partial r}\right)\right] + O(\Delta x^3) \tag{B29}$$

Using always the same method and noting that $\hat{\mathbf{r}}$ direction is opposite to $\hat{\mathbf{n}}$ whereas $\hat{\mathbf{z}}$ and $\hat{\mathbf{n}}$ have the same direction

$$\rho^{t+1}_{M,0} = \rho^{t}_{M,0} + D_{a\,M,0}\left[2\alpha\left(\rho^{t}_{M-1,1} - \rho^{t}_{M,0} - \Delta x \frac{\dot{m}}{D_{a_{dim}M,0}}\frac{d}{\hat{\rho}}\right) + \right. \\ \left. + \frac{\Delta t}{r_{int}}\frac{\dot{m}}{D_{a_{dim}M,0}}\frac{d}{\hat{\rho}}\right] - \Delta t \frac{D_{a\,M,0} - D_{a\,M-1,0}}{2}\frac{\dot{m}}{D_{a_{dim}M,0}}\frac{d}{\hat{\rho}} \tag{B30}$$

B.2.7 Corner 3

Expanding the solution to a second order Taylor series and substituting Eq (B13) we have

$$\rho^{t}_{M-1,N-1} = \rho^{t}_{M,N} - \Delta x \left(\frac{\partial \rho}{\partial r} - \frac{\partial \rho}{\partial z}\right) + \frac{\Delta x^2}{2}\left[\frac{1}{D_a}\left(\frac{\partial \rho}{\partial t} - \frac{\partial \rho}{\partial z}\frac{\partial D_a}{\partial z}\right) - \right. \\ \left. - \left(\frac{1}{r_{int}}\frac{\partial \rho}{\partial r}\right)\right] + O(\Delta x^3) \tag{B31}$$

Using always the same method and noting that both $\hat{\mathbf{z}}$ and $\hat{\mathbf{r}}$ have the same direction as $\hat{\mathbf{n}}$

$$\rho^{t+1}_{M,N} = \rho^{t}_{M,N} + D_{a\,M,N}\left[2\alpha\left(\rho^{t}_{M-1,N-1} - \rho^{t}_{M,0} - \Delta x \frac{\dot{m}}{D_{a_{dim}M,N}}\frac{d}{\hat{\rho}}\right) + \right. \\ \left. + \frac{\Delta t}{r_{int}}\frac{\dot{m}}{D_{a_{dim}M,N}}\frac{d}{\hat{\rho}}\right] - \Delta t \frac{D_{a\,M,N} - D_{a\,M-1,N}}{2}\frac{\dot{m}}{D_{a_{dim}M,N}}\frac{d}{\hat{\rho}} \tag{B32}$$

B.2.8 Corner 4

Expanding the solution to a second order Taylor series and substituting Eq (B13) we have

$$\rho^{t}_{1,N-1} = \rho^{t}_{0,N} + \Delta x \left(\frac{\partial \rho}{\partial z} - \frac{\partial \rho}{\partial r}\right) + \frac{\Delta x^2}{2}\left[\frac{1}{D_a}\left(\frac{\partial \rho}{\partial t} - \frac{\partial \rho}{\partial z}\frac{\partial D_a}{\partial z}\right) - \right. \\ \left. - \left(\frac{1}{r_{int}}\frac{\partial \rho}{\partial r}\right)\right] + O(\Delta x^3) \tag{B33}$$

Using always the same method and noting that $\hat{\mathbf{z}}$ direction is opposite to $\hat{\mathbf{n}}$ whereas $\hat{\mathbf{r}}$ and $\hat{\mathbf{n}}$ have the same direction

$$\begin{aligned}\rho_{0,N}^{t+1} =& \rho_{0,N}^{t} + D_{a\,0,N}\left[2\alpha\left(\rho_{1,N-1}^{t} - \rho_{0,N}^{t} - \Delta x\frac{\dot{m}}{D_{a_{dim}0,N}}\frac{d}{\hat{\rho}}\right) - \right.\\ &\left. - \frac{\Delta t}{r_{int}}\frac{\dot{m}}{D_{a_{dim}0,N}}\frac{d}{\hat{\rho}}\right] + \Delta t\frac{D_{a\,1,N} - D_{a\,0,N}}{2}\frac{\dot{m}}{D_{a_{dim}0,N}}\frac{d}{\hat{\rho}}\end{aligned} \tag{B34}$$

Appendix C

Differential equation analytical solution

To solve a system of linear differential equation with variable coefficients of the kind

$$\begin{bmatrix} dy_1/dt \\ dy_2/dt \end{bmatrix} = \begin{bmatrix} F_{11}(t) & F_{12}(t) \\ F_{21}(t) & F_{22}(t) \end{bmatrix} \begin{bmatrix} y_1 \\ y_2 \end{bmatrix} + \begin{bmatrix} U_1(t) \\ U_2(t) \end{bmatrix} \tag{C1}$$

where F and U are continuous functions of t in an interval where the solution is required we must define some matrix operations:

- The integration or derivation of a matrix is a matrix whose elements are the integral/derivatives of the coefficients of the original matrix

$$\frac{dA(t)}{dt} = \frac{d}{dt}\begin{bmatrix} A_{11}(t) & A_{12}(t) \\ A_{21}(t) & A_{22}(t) \end{bmatrix} = \begin{bmatrix} dA_{11}(t)/dt & dA_{12}(t)/dt \\ dA_{21}(t)/dt & dA_{22}(t)/dt \end{bmatrix} \tag{C2}$$

$$\int A(t)dt = \int \begin{bmatrix} A_{11}(t) & A_{12}(t) \\ A_{21}(t) & A_{22}(t) \end{bmatrix} dt = \begin{bmatrix} \int A_{11}(t)dt & \int A_{12}(t)dt \\ \int A_{21}(t)dt & \int A_{22}(t)dt \end{bmatrix} \tag{C3}$$

- the elevation of a matrix to the power *n* is the result of the line-by-row product of the matrix by itself repeated *n* times

$$\begin{aligned} A^n &= \prod_{i=1}^{n} A \\ A^3 = A \cdot A \cdot A &\neq \begin{bmatrix} A_{11}(t)^3 & A_{12}(t)^3 \\ A_{21}(t)^3 & A_{22}(t)^3 \end{bmatrix} \end{aligned} \tag{C4}$$

- the exponential of a matrix is calculated using the Taylor infinite expansion of the exponential function and hence is in general different from a matrix formed by the exponential of the single elements

$$\begin{aligned} exp(A) = e_M{}^A &= \prod_{i=1}^{\infty} \frac{1}{i!} A^i \\ e_M{}^A &\neq \begin{bmatrix} e^{A_{11}(t)} & e^{A_{12}(t)} \\ e^{A_{21}(t)} & e^{A_{22}(t)} \end{bmatrix} \end{aligned} \tag{C5}$$

- from this definition of the exponential of a matrix and noting that $\infty - 1 = \infty$ the derivative of the exponential of a matrix can be expressed as

$$\frac{de_M{}^{A(t)}}{dt} = \prod_{i=1}^{\infty} \frac{1}{i-1!} A(t)^{i-1} \frac{dA(t)}{dt} = \prod_{i=0}^{\infty-1} \frac{1}{i!} A(t)^i \frac{dA(t)}{dt} = e_M{}^{A(t)} \frac{dA(t)}{dt} \tag{C6}$$

Eq (C1) can be rewritten in a matrix form as

$$\frac{dY}{dt} = F(t)Y + U(t) \tag{C7}$$

Since $F(t)$ is a continuous function $e_M^{-\int F(t)dt}$ will be continuous as well hence Eq (C7) is equivalent to

$$e_M^{-\int F(t)dt}\left[\frac{dY}{dt} - F(t)Y\right] = e_M^{-\int F(t)dt}\,U(t) \tag{C8}$$

Noting that the LHS is the derivative of the product $YF(t)$ we have

$$\frac{d}{dt}\left[e_M^{-\int F(t)dt}\,Y\right] = e_M^{-\int F(t)dt}\,U(t) \tag{C9}$$

integrating the LHS and the RHS of the above equation we get

$$e_M^{-\int F(t)dt}\,Y = C + \int\left(e_M^{-\int F(t)dt}\,U(t)\right)dt \tag{C10}$$

hence the general solution is

$$Y = e_M^{\int F(t)dt}\,C + e_M^{\int F(t)dt}\cdot\int\left(e_M^{-\int F(t)dt}\,U(t)\right)dt \tag{C11}$$

Where C is a constant vector. Assuming to have a Cauchy problem of the form

$$Y(t_0) = Y_0 \tag{C12}$$

the particular solution becomes

$$Y = e_M^{\int_{t_0}^{t} F(x)dx}\,Y_0 + e_M^{\int_{t_0}^{t} F(x)dx}\cdot\int_{t_0}^{t}\left(e_M^{-\int_{t_0}^{x} F(\tau)d\tau}\,U(x)\right)dx \tag{C13}$$

Appendix D

How to use the model

Here a simple guide explaining how to use the model presented in this thesis will be reported to help any reader that would be interested in using the model to obtain hollow cathode life time predictions.

First of all to obtain life time predictions some input data are needed:

- the cathode insert and geometry
- the starting composition of the impregnant (usually 4 BaO – 1 CaO – 1 Al_2O_3)
- the mass flow rate and discharge current at which the cathode is running
- the insert temperature distribution along the cathode length at the beginning of life
- the plasma density, electron temperature and voltage drop distribution along the cathode length at the beginning of life.

1) BaO depletion calculation

input: insert geometry, insert temperature, starting impregnant composition.

output: BaO content in any point inside the insert and at any time during the cathode life, BaO evaporation rate at every point on the insert surfaces and at any time during the cathode life.

Using the model reported in §3.2 (BaO evaporation calculation) and in §3.5 (3D BaO depletion) with the numerical scheme in Appendix A and the trend of the diffusion coefficient reported in Eq. (114) starting from the insert geometry and temperature, and from the initial impregnant composition, the BaO content inside the insert and the BaO evaporation rate can be calculated at any time during the cathode life.

2) Surface coverage evolution prediction

input: insert geometry, insert temperature, BaO content and BaO evaporation rates, plasma characteristics at the beginning of life, cathode discharge current.

output: low work function surface coverage evolution with time, work function evolution with time

Using the model reported in §4.5.1 (surface coverage evolution) with the deposition and desorption rates reported in §4.2 – §4.4 the evolution of the surface coverage can be calculated. At the same time the evolution of the work function must be calculated using the equations in §4.5.2.
Since the desorption rates depend on the plasma characteristics, during the surface coverage evolution the plasma parameters must be updated at fixed time steps (with a span between them of the order of 10 hours) using the plasma update procedure reported in §4.5.3.

3) Life time prediction

input: insert geometry, BaO evaporation rates, surface coverage evolution, star up phase duration, start up temperature.
output: hollow cathode life time

Using the equations reported in §5.4.1.1 the total mass of BaO that evaporates during the start up phase and the total mass of BaO required to obtain a full surface coverage can be calculated.
Noting when the value of the total evaporated mass falls below the needed BaO mass the life time of the cathode can be obtained according to the criterion reported in §5.4.1.1

As already pointed out in the thesis the hollow cathode life time is very sensitive to the start up procedure duration and to the start up temperature.
In case these values differ sensibly from the one used in this thesis it would be advisable to tune the model repeating what has been done in §5.4.1.1. This will imply carrying on an experimental life test (it can be done forcing the cathode to work at a very high discharge current so that the life time and hence the duration of the test are short) and varying the value of start up temperature used in the model until the predicted life time matches the experimental one.
The model is also very sensible to the insert temperature and to the plasma parameters.
Although the life time model presented in this thesis has been derived to obtain conservative estimates of the lifetime it is strongly recommended to measure the values of insert temperature and plasma parameter at the beginning of life of the cathode

instead of using guessed values (unless a reliable plasma model can be used to obtained such values).

If a plasma model is not available and the insert temperature and plasma parameter must be guessed it will be advisable to use conservative values, hence high insert temperatures, plasma particle densities and voltage falls to produce conservative estimates on the lifetime.

The last remark about using the model concerns the accuracy of the life time predictions.

During the development of the model we have been forced to do a number of assumptions due to the lack of data mainly relatively to the chemical processes taking place in the cathode and to the fact that some of the hollow cathode processes are still not completely understood.

Because of this all the assumptions made have been done to obtain conservative estimates of the lifetime. If very accurate life time estimates are required a small number of quick life tests (of the order of 1 to 10 thousand hours) could be carried out (using very high discharge currents to limit the duration of the tests) to tune the model for the particular cathode and hence being able to obtain accurate life time prediction for very long life tests (100 thousands of hours).

Appendix E

Nomenclature

A_{th}	thermionic emission constant, 1.26 10^6 A/(m^2 °K)
A	area
A, B, C	in the ternary diagram respectively Al2O3, BaO, CaO
d	one-dimensional insert length
D_a	diffusion coefficient
E	electric field
E_{act}	activation energy
E_{ion}	ionization energy
E_{trans}	transferred energy
E_0	initial energy
h	Plank constant
I_e	electronic current
I_{eq}	mass flow rate equivalent current
I_D	discharge current
I_i	ionic current
I_{th}	thermionic current
IDS	insert inner diameter surface
J	current density
J_i	ion current density
J_e	electron current density
J_{or}	orifice current density
J_{th}	thermionic current density
k_b	Boltzamann constant
kb	backward reaction constant
kf	forward reaction constant
K_p	equilibrium constant
L_c	cathode length
L_{Da}	characteristic diffusion length
m_{BaO}	barium oxide molecular mass in kilograms
m_e	electron mass

m_i	ion mass
M_{BaO}	barium oxide molecular mass in a.m.u.
$m_{BaO\ evap}$	barium oxide mass evaporated during the start up phase
$m_{BaO\ needed}$	barium oxide mass needed to reach a full surface coverage
$\dot{m}$	mass flow rate per unit area
n	plasma particle density (where quasi neutrality is assumed)
n_e	electron plasma particle density
n_i	ion plasma particle density
n_0	neutral particle density
$\dot{n}$	ionization rate
N^+	deposition rate
N^{-th}	thermal desorption rate
N^{-bomb}	ion sputtering desorption rate
ODS	insert outer diameter surface
OP	orifice plate
p	pressure
p_{BaO}	barium oxide pressure
q	electron charge
r	radial coordinate along the insert depth
R	universal gas constant / radius
r_{int}	internal insert radius
R_{Ba}	barium atomic radius
S_{insert}	insert surface area
S_{op}	orifice surface area
t	time
t_{start}	start up phase duration
T	temperature
T_e	electron temperature
T_i	ion temperature
T_{start}	start up insert temperature
T_w	insert temperature
US	upstream insert surface
v_e	electron velocity
v_i	ion velocity

v_{th}	thermal velocity
v_0	neutral velocity
V	potential
x	coordinate along the cathode depth
Y_{sputt}	sputtering yield
z	coordinate along the cathode depth
α	ionization fraction/ convergence parameter/bombing coefficient
β	voltage amplification factor
δ	barium oxide depletion depth
ΔG	free Gibbs energy variation
ΔH	enthalpy variation
ΔS	entropy variation
ΔV	sheath voltage drop
Δt	numerical time step
Δx	numerical space step
ϵ_0	vacuum dielectric constant
ϕ	work function
ϕ_{eff}	effective work function
ϕ_0	work function at 0 °K
η	plasma resistivity
κ	thermal conductivity
κ_e	thermal conductivity
κ_i	thermal conductivity
κ_n	thermal conductivity
λ_D	Debye length
ν	collision frequency
ν_{ei}	collision frequency
ν_{en}	ion-electron collision frequency
ν_{in}	ion-neutral collision frequency
ν_{iz}	ionization collision frequency
θ	surface coverage
ρ	density
σ	collision cross section

τ	characteristic time
ξ_{BaO}	barium oxide stoichiometric coefficient
$x_{,y}$	partial derivative of the variable “x” with respect to the variable “y”
$\dot{x}$	time derivative of the variable “x”
x_i^t	numerical variable “x” calculated at the time “t” and in the location “i”

Bibliography

[1] M. Coletti, A. Grubisic, N. Wallace, "*European Student Moon Orbiter Solar Electric Propulsion Subsystem Architecture. An All – Electric Spacecraft*", IEPC-2007-111, 30th Electric International Propulsion Conference, Florence, Italy, September 2007.

[2] Sengupta, "Destructive Physical Analysis of Hollow Cathodes from the Deep Space 1 Flight Spare Ion Engine 30,000 Hr Life Test", IEPC-2005-026, 29th International Electric Propulsion Conference, Princeton, 31 October – 4 November , 2005

[3] K. Jameson, D.M. Goebel, RM. Watkins, *"Hollow Cathode and Thruster Discharge Chamber Plasma Measurements"*, IEPC-2005-269, 29th International Electric Propulsion Conference, Princeton, 31 October – 4 November , 2005

[4] D.M. Goebel, K. Jameson, I. Katz, I.G. Mikellides, *"Energetic Ion Production and Keeper Erosion in Hollow Cathode Discharges"*, IEPC-2005-266, 29th International Electric Propulsion Conference, Princeton, 31 October – 4 November , 2005

[5] I.G. Mikellides, I. Katz, D.M. Goebel, "*Numerical Simulation of the Hollow Cathode Discharge Plasma Dynamics*", IEPC-2005-200, 2005

[6] I.G. Mikellides , I. Katz, D.M. Goebel, J.E. Polk, "*Hollow Cathode Theory and Experiment. A Two-Dimensional Model of the Emitter Region*", J. of App. Physics, v98, 2005

[7] A. Salhi, P. J. Turchi, "*Theoretical Modelling of Orificed Hollow Cathode Discharges*", Journal of Propulsion and Power, September 1994.

[8] E.L. Murphy and R.H. Good, "*Thermionic Emission, Field Emission, and the Transition Region*", Physical Review 102, 1956

[9] S. Pottinger, "*Investigation of Steady State Characteristics of Hollow Cathode Internal Plasmas using Optical Emission Spectroscopy*", PhD Thesis, University of Southampton, 2005

[10] J.M. Roquais, F. Poret, R. le Doze et al., "*Barium Depletion Study on Impregnated Cathodes and Lifetime Prediction*", Applied Surface Science 215, pp 5-17, 2003.

[11] K. L. Jensen, Y. Y. Lau and B. Levush, "*Migration and Escape of Barium Atoms in Thermionic Cathode*", IEEE Transaction on Plasma Science, Vol. 28, No. 3, 2000

[12] S.D. Kovalesky, " *Life Model of Hollow Cathodes Using a Barium Calcium Aluminate Impregnated Tungsten Emitter*", IEPC-01-276, Pasadena, 2001

[13] R. T. Longo, E. A. Adler, and L. R. Falce, "*Dispenser Cathode Life Prediction Model*", International Electron Devices Meeting 1984

[14] R.T. Longo, "*Physics of Thermionic Dispenser Cathode Aging*", Journal of Applied Physics, Vol 94, No 10, 2003

[15] W G. Tighe, K.R Chien, *"Hollow Cathode Ignition Studies and Model Development*", IEPC-2005-314, 29th International Electric Propulsion Conference, Princeton, November 2005.

[16] I. Katz, et al. "*Model of Hollow Cathode Operation and Life Limiting Mechanisms*". IEPC-2003-0243, 2003.

[17] J. Polk, "*The Effect of Oxygen on Hollow Cathode Operation*", 42nd Jint Propulsion Conference, Sacramento, 2006

[18] Goebel, D.M. et al. "*Extending Hollow Cathode Life for Electric Propulsion in Long Term Missions*". AIAA-2004-5911, Space 2004 Conf. and Exhibit, 2004.

[19] B.V. Bondarenko, E.P. Ostapchenko, B.M. Tsarev, "*Thermionic Properties of Alkali Metal Tungstates*", Radiotekh. Elektron, Vol 5, pp 1246-1253, 1960

[20] P. Appendino, "*Ricerche sul Sistema Ternario Calce-Ossido di Bario-Allumina*", Ceramurgia, pp. 103-106, 1972.

[21] T.N. Resulhina, V.A. Levitskii, M.Ya. Frenkel, Izvestiya Akademii Nauk SSSR, Neorgan. Mater. 2, pp. 325-331, 1966.

[22] T. R. Sarver-Verhey, "Destructive Evaluation of a Xenon Hollow Cathode After a 28,000 Hour Life Test", NASA/CR—1998-208678, 1998

[23] T. R. Sarver-Verhey, "*Scenario for Hollow Cathode End-of-Life*", NASA/CR—2000-209420, 2000

[24] S.D. Kovaleski, M.J. Patterson, G.C. Soulas, T.R. Sarver-Verhey, "A Review of Testing of Hollow Cathodes for The Interantional Space Station Plasma Contractor", IEPC-01-271, 27th International Electric Propulsion Conference, Pasadena, CA, 15-19 October, 2001

[25] J. Polk, A. Grubisic, N. Taheri, D. Goebel, R. Downey, S. Hornbeck, "*Emitter Temperature Distributions in the NSTAR Discharge Hollow Cathode*", AIAA-2005-4398

[26] D.M. Goebel, K. Jameson, I. Katz, I.G. Mikellides, "*Energetic Ion Production and Keeper Erosion in Hollow Cathode Discharges*", IEPC-2005-266, 2005

[27] G.M Wolten, "*An Appraisal of the Ternary System BaO-CaO-Al2O3*", SD-TR-80-67, Space Division, Air Force Command, Los Angeles, 1980

[28] R.A. Lipeles, H.K.A. Kan, "*Stability of Barium Calcium Aluminate*", App. of Surf. Sc.,pp16-189, 1983

[29] L.L.Y. Chang, M.G. Scroger, B. Phillips, "*Alkaline-Earth Tungstates: Equilibrium and Stability in the M – W – O Systems*", Journal of the American Ceramic Society, Vol 49, n 7, pp 385-390, 1966

[30] B. Phillips, L.L.Y. Chang, "*High Temperature Stability of Tungsten Oxide Structures*", Transaction of The Metallurgic Society of AIME, Vol 230, pp 1203-1206, 1964

[31] E.R. Kreidler, "*Phase Equilibria in the System CaO – BaO – WO_3*", Journal of the American Ceramic Society, Vol 55, n 10, pp 514-519, 1972

[32] D.E. Sigfried, P.J. Wilbur "*A Model for Mercury Orificed Hollow Cathodes: Theory and Experiment*" AIAA Journal, Vol. 22, No. 10, October 1984

[33] I. Katz,J. R. Anderson,J. E. Polk,J. R. Brophy, "*One-Dimensional Hollow Cathode Model*", Journal of Propulsion and Power,Vol. 19, No. 4, July–August 2003

[34] P. Rossetti, F. Paganucci, M. Andrenucci, "*A Hollow Cathode Model for Application to the Electric Propulsion*", AIAA 2002-4239, 38th Joint Propulsion Conference & Exhibit, Indianapolis, July 2002.

[35] I Katz, J. E. Polk, I. G. Mikellides et al. , "*Combined Plasma and Thermal Hollow Cathode Insert Model*", IEPC-2005-228, 2005.

[36] I.G. Mikellides , I. Katz, D.M. Goebel, J.E. Polk, "*Theoretical Model of a Hollow Cathode Plasma for the Assessment of Insert and Keeper Lifetimes*", 41st AIAA Joint Propulsion Conference, Arizona, 2005

[37] P.D. Prewett, J.E. Allen, "*Double Sheath Associated with a Hot Cathode*", Proceeding of Royal Society of London, Ser A (341), April 1976

[38] A. Salhi, H.M. Mayers, P.J. Turchi, "*Experminetal investiagtion of a hollow cathode discharge*", IEPC Paper No 93-025, September 1993

[39] M. Coletti, S.B. Gabriel, "*A Chemical Model for Barium Oxide Depletion from Hollow Cathode's Insert*", AIAA-2007-5193, 43rd AIAA/ASME/SAE/ASEE Joint Propulsion Conference & Exhibit, Cincinnati, Ohio, USA, July 2007.

[40] M. Coletti, S.B. Gabriel, "*A Model for Barium Oxide Depletion from Hollow Cathodes' Inserts*", IEEE Transaction on Plasma Science, accepted for publication expected December 2008.

[41] I.M. Ahmed Rudwan, N. Wallace, M. Coletti, S.B. Gabriel, "*Emitter Depletion measurement and modelling in the T5&T6 Kaufman-type Ion Thrusters*", IEPC-2007-256, 30th Electric International Propulsion Conference, Florence, Italy, September 2007.

[42] M. Coletti, S.B. Gabriel, "*A Model for Low Work Function Compound Deposition on Hollow Cathode Insert Surface*", 46th AIAA Aerospace Sciences Meeting and Exhibit, Reno, Nevada, USA, January 2008

[43] M. Coletti, S.B. Gabriel, "*Coupling between plasma characteristics and insert low work function surface coverage in hollow cathodes*", 44th AIAA/ASME/SAE/ASEE Joint Propulsion Conference & Exhibit, Hartford, CT, 20 - 23 Jul 2008

[44] Langmuir, "*The Nature Of Adsorbed Films of Caesium on Tungsten*", Physical review, vol 43, 1933

[45] H. Kingdon, I. Langmuir, "*The Removal of Thorium from the Surface of a Thoriated Tungsten Filament by Positive Ion Bombardment*", Physical review, 1923

[46] Langmuir, "*The Electron Emission from Thoriated Tungsten Filaments*", Physical review, vol 22, 1923

[47] J.B. Taylor, I. Langmuir, "*The Evaporation of Atoms, Ions and Electrons from Caesium Films on Tungsten*", Physical Review, vol 44, n 6, 1933

[48] Langmuir, K.H. Kingdon, "*Thermionic Effects Caused by Vapours of Alkali Metals*", Proceeding of the Royal Society of London, vol 107, no 741, pp61-79, 1925

[49] R.C. Huges, P.P. Coppola, H.T. Evans, "*Chemical Reactions in Barium Oxide on Tungsten Emitters*", Journal of Applied Physics, Vol. 23 N 6, June 1952.

[50] P. Palluel, A.M. Shroff, "*Experimental Study on Impregnated Cathode Behaviour, Emission and Life*", J. Appl. Phys. 51, pag. 2894, 1980

[51] P. Silvestroni, "*Fondamenti di Chimica*", Veschi Editore, Roma, 1974

[52] Wikipedia, http://en.wikipedia.org/wiki/Activation_energy from "*Compendium of Chemical Terminology*", IUPAC

[53] S. Dushmann, "*Electron Emission from Metals as a Function of Temperature*", Physical Review 21, 1923

[54] L.Gori, "*Calcolo Numerico*", Ed. Kappa, Roma, 1999

[55] A. Ghizzetti, F. Rosati, "*Analisi Matematica*", Ed Masson, Roma, 1996

[56] P. Gessini, S. B. Gabriel and D. G. Fearn, "*A Study of the Thrust Generated by a T6 Hollow Cathode*", AIAA Paper 2006-5265, 42nd AIAA/ASME/SAE/ASEE Joint Propulsion Conference & Exhibit, Sacramento, CA, July 2006

[57] P. Gessini, S. B. Gabriel and D. G. Fearn, "*The T6 Hollow Cathode as a Microthruster*", AIAA Paper 2005-4078, 41st AIAA/ASME/SAE/ASEE Joint Propulsion Conference & Exhibit, Tucson, AZ, July 2005.

[58] P. Gessini, S. B. Gabriel and D. G. Fearn, "*Thrust Characterization of a T6 Hollow Cathode*", IEPC Paper 05-257, 29th International Electric Propulsion Conference, Princeton, NJ, October-November 2005

[59] P. Gessini, M. Coletti, N. Bevan, R. Intini Marques, G. Michalareas and S. B. Gabriel, "*Solar Electric Propulsion for Lunar Transfer*", Solicited Paper, 1st Hellenic-European Student Space Science and Technology Symposium, Patras, Greece, 2006.

[60] P. Gessini, M. Coletti, A. Grubisic S. Gabriel, N. Wallace, D. Fearn, "*Hollow Cathode Thruster for All-Electric Spacecraft*", to be published at next JPC in Cincinnati.

[61] M. Coletti, I. A. Rudwan, N. Wallace, S.B. Gabriel, University of Southampton and QinetiQ report to ESA, contract 16614/02/NL/PA, CCN 8, 2007

[62] O.K. Kultashev, A.P. Makarov, "*Effect of Oxygen Adsorption on the Electronic and Adsorption Properties of Barium Atoms on the (100), (110) and (111) Faces of Tungsten*", Izv. Akad. Nauk SSSR, 38(2):317–321, 1974.

[63] R. Foreman, "*Comment on the mechanism of operation of the impregnated tungsten cathode*", Journal of Applied Physics, vol 50, n° 3, March 1979

[64] E.S. Rittner, "*On the Mechanism of Operation of the Type B Impregnated Cathode*", Journal of Applied Physics, vol 48, n° 10, October 1977

[65] E.S. Rittner, R.H. Ahlert, W.C. Rutledge, "*Studies on the Mechanism of Operation of the L Cathode. I*", Journal of Applied Physics, vol 28, n° 2, February 1957

[66] W.C. Rutledge, E.S. Rittner, "*Studies on the Mechanism of Operation of the L Cathode. II*", Journal of Applied Physics, vol 28, n° 2, October 1956

[67] K. Hilpert, "*Mass Spectrometric Study of the Evaporation of* $BaAl_2O_4$", High Temperature Science 7, 1975

[68] E.S. Rittner, W.C. Rutledge, R.H. Ahlert, "*On the Mechanism of Operation of the Barium Aluminate Impregnated Cathode*", Journal of Applied Physics, vol 28, n° 12, Dicember 1957

[69] V.M. Rashkovan, I.A. Ponomaryova, "Optical Probe and Measurements of the Hollow Cathode Plasma", Journal of Physics D: Applied Physics vol 38, 2005

[70] G.J. Williams, T.B. Simth, K.H. Glick, Y. Hidaka, A.D. Gallimore, "FMT-2 Discharge Cathode Erosion Ratye Measurements via Laser Induced Fluorescence", AIAA Paper 2000-3663

[71] M.W. Crofton, "Mesurement of Barium Production in a Hollow Cathode", AIAA-2005-3665, 41st Joint Propulsion Conference, 2005

[72] A. Sengupta, J.R. Brophy, K. D. Goodfellow, “Status of the Extended Life Test of the Space 1 Flight Spare Ion Engine After 20,252 Hors of Operation”, AIAA-2003-4558, 39th Joint Propulsion Conference, 2003